THESIS FOR THE DEGREE OF DOCTOR OF PHILOSOPHY

# Interaction of water with supplementary cementitious materials

Hydration mechanism, microstructure and moisture transport

Liming Huang

Division of Building Technology

Department of Architecture and Civil Engineering

CHALMERS UNIVERSITY OF TECHNOLOGY

Gothenburg, Sweden 2023

**Interaction of water with supplementary cementitious materials**

Hydration mechanism, microstructure and moisture transport

Liming Huang
ISBN 978-91-7905-871-5



Doktorsavhandlingar vid Chalmers tekniska högskola
Ny serie nr 5337
ISSN 0346-718X

Department of Architecture and Civil Engineering
Division of Building Technology
Chalmers University of Technology
SE-412 96 Gothenburg
Sweden
Telephone + 46 (0)70-879 1506
Author e-mail: limingh@chalmers.se

Cover:

Graphical illustration of the scientific topics in this dissertation

Chalmers Reproservice
Gothenburg, Sweden 2023

**Interaction of water with supplementary cementitious materials**

Hydration mechanism, microstructure and moisture transport

LIMING HUANG
Department of Architecture and Civil Engineering
Division of Building Technology, Building Materials
Chalmers University of Technology

# Abstract

Supplementary cementitious materials (SCMs) offer a sustainable solution to reduce carbon emissions from the production of cement and concrete. This dissertation explores the impact of SCMs and the related additives on the hydration process of cementitious materials, which affects their microstructure and transport properties. Water is involved in the whole life of the cementitious materials thereby determining the hydration, microstructure, and durability. Advanced techniques were employed in this study to investigate the impact of additives on the hydration of $C_3S$, alterations in water dynamics and microstructure induced by SCMs, and their correlation to transport properties. A device was designed to continuously monitor the effect of SCMs on early hydration, and it was subsequently updated to monitor the hardening process of concrete containing SCMs.

Results show that the dissolution theory fails to explain anomalous hydration of tricalcium silicate at high water to solid ratio. A new hypothesis in this study proposes that calcium silicate hydrate (C-S-H) primarily nucleates within the near-surface region, and this hypothesis bridges the gap between dissolution and protective layer theories. The precipitation involves primary particle nucleation and growth by particle attachment. Acceleration in C-S-H growth, instead of etch pit dissolution, may explain the rapid increase in reaction rate after the induction period. The hypothesis provides a thorough explanation for the impact of potassium salts and pH on the dissolution of $C_3S$ and the precipitation of C-S-H. The newly designed device exhibits excellent performance in monitoring the interaction of water with cement and SCMs. The evolution of electrical conductivity in hydrating pastes closely relates to chemical reaction process. SCMs reduce the initial conductivity of pastes mainly by decreasing alkali concentration. The growth rate of the formation factor replicates the reactivity of different binders. Blending SCMs refines the pore structure, decreases pore connectivity and results in a higher formation factor. A percolation model can be used to demonstrate the relationship between volume of evaporable water and formation factor.

SCMs affect not only the pore structure of hardened cement-based paste (hcp), but also the phase assemblage and water dynamics. The effect of SCMs on mesoscale pore structure can be

well indicated by water vapour desorption isotherms, but effects of ion on water vapour equilibrium pressure must be considered when calculating the pore size distribution. A novel approach works well in evaluating the hydration degree of SCMs by use of water vapour sorption and thermodynamic modelling. Thermoporometry and broadband dielectric spectroscopy effectively characterise moisture distribution and water dynamics in hcp, respectively. SCMs have limited effects on the dynamics of structural water, primarily influencing water dynamics in small gel pores and interfacial polarization. The first drying process decreases the volume of unfrozen water (< ~2.4 nm) under any level of relative humidity. Gel pores coarsen significantly during the drying between 75 % and 50 %.

Change of microstructure alters the transport of moisture and chloride in hcp. The decrease in both moisture transport coefficient and chloride migration coefficient induced by SCMs is notably more significant at a higher water-to-binder ratio upon extended curing period. The modified moisture transport in blended systems is mainly due to pore structure refinement, specifically the reduction in pore connectivity. Both the formation factor and porosity of small pores determine the moisture transport in hcp, with the formation factor being more significant at high RH and the porosity of small pores being more significant at low RH. The effect of SCMs on chloride diffusion is mainly attributed to their influence on pore connectivity. A simplified model based on the formation factor can be used to estimate the chloride migration coefficient for the blended pastes and mortars.

The upgraded device provides a reliable non-destructive monitoring of concrete performance by measuring electrical conductivity and internal temperature accurately. Formation factor, maturity and ultrasonic pulse velocity are reliable indices for concrete strength; however, formation factor exhibits the optimal performance. This study provides insights into the mechanism of water interacting with cementitious materials and a new non-destructive method to promote the high-quality use of SCMs in sustainable concretes.

**Keywords:**

Supplementary cementitious materials; hydration; durability; electrical conductivity; formation factor; microstructure; moisture transport

**Växelverkan mellan vatten och supplementary cementitious materials**

Hydratiseringsmekanism, mikrostruktur och fuktransport

LIMING HUANG
Institutionen för Arkitektur och samhällsbyggnadsteknik
Avdelningen för Byggnadsteknologi, byggmaterial
Chalmers tekniska högskola

# Sammanfattning

Alternativa bindemedel (supplementary cementitious materials, SCMs) erbjuder en hållbar lösning för att minska koldioxidutsläppen från produktionen av cement och betong, som är en stor bidragande faktor till globala växthusgasutsläpp. Denna avhandling utforskar effekten av SCMs och relaterade tillsatser på hydratiseringsprocessen av cementbaserade material, vilka kan påverka dess mikrostruktur och transportegenskaper. Vatten är involverat i hela livet av cementbaserade material och avgör därmed hydratiseringen, mikrostrukturen och beständigheten. Avancerade tekniker användes i denna studie för att undersöka effekten av tillsatser på hydratiseringen av $C_3S$, mikrostrukturell förfining genom SCMs och dess relation till transportprocesser, samt bedöma förändringar i vattendynamiken. En enhet designades för att övervaka effekten av SCMs på tidig hydratisering och den uppdaterades senare för att övervaka härdningsprocessen av betong som innehåller SCMs.

Resultaten visar att upplösningsteorin misslyckas med att förklara anomal hydratisering vid höga vatten pulvertal. En ny hypotes i denna studie föreslår att C-S-H främst nukleeras inom när-ytan regionen, denna hypotes bygger en bro mellan upplösnings- och skyddandelagerteorier. När utfällning sker, uppstår en primärpartikel nukleering och tillväxt genom partikel sammanfogning. Accelerationen i C-S-H-tillväxt, istället för gropetsningsupplösning, kan förklara den snabba reaktionshastighetsökningen efter induktionsperioden. Hypotesen förklarar väl upplösning av $C_3S$ och C-S-H-utfällning påverkad av kaliumsalter och pH-nivåer. Den utvecklade enheten fungerar bra vid övervakning av vatteninteraktioner med SCM. Utvecklingen av elektrisk ledningsförmåga i hydratiserande pastor relaterar nära till kemiska reaktionsprocesser och kan klassificeras i fyra faser. SCM minskar den initiala ledningsförmågan för pasta främst genom att minska alkalikoncentrationen. Tillväxthastigheten för formationsfaktorn indikerar reaktiviteten hos olika bindemedel. Inblandning av SCM förfinar porstrukturen genom att minska anslutningen mellan porer och resulterar i en högre formationsfaktor. Övervakning av ledningsförmåg demonstrerar visar på relationen mellan förångbar vattenvolym och formationsfaktorn, vilket underlättar in-situ övervakning av fuktinnehåll.

SCM påverkar inte bara porstrukturen i härdade cementbaserade pastor (hcp), utan också dess fassammansättning och vattendynamik. Den mesoskala porstrukturen i pastor med SCM kan indikeras väl av vattenångadsorptionisotermer, men jonernas effekter på vattenångjämvikts tryck måste beaktas vid beräkning av porstorleksfördelning. En ny metod fungerar bra för att utvärdera SCMs hydratiseringsgrad genom användning av vattenångsorption och termodynamisk modellering. SCMs ökar både små och stora gel porvolymer, mest märkbart vid ett vatten till bindemedel-förhållande på 0,35. Termoporometri och bredbandig dielektrisk spektroskopi karaktäriserar effektivt fuktfördelning och dynamik i hcps, respektive. SCM har begränsad effekt på dynamiken i strukturellt vatten, som främst påverkar vattendynamiken i små gel porer och interfacial polarisation. Den första torkningsprocessen minskar volymen av ofruset vatten (< 2,4 nm) under olika nivåer av relativa fuktigheter. Gel porer förstoras avsevärt under torkningen mellan 75 % och 50 %.

Porstrukturen hos hpc påverkas kraftigt av SCMs, vilket kan förändra transportegenskaperna för fukt och klorider. Minskningen av både fuktransportkoefficient och kloridmigrationskoefficient som orsakas av SCM är märkbart mer signifikant i hcp med högre vatten/ bindemedelstal efter en längre härdningsperiod. Förbättrad motståndskraft mot fukt i blandade system beror främst på en förfining av porstrukturen, särskilt minskningen av poranslutning. Både formationsfaktorn och porositeten hos små porer bestämmer fuktransportegenskaperna hos hcp, med formationsfaktorn som är viktigast vid hög relativa fuktigheter och porositeten hos små porer som är viktigast vid låg relativ luftfuktighet. Effekten av SCMs på kloridmotståndet beror på vatten/bindemedelsförhållandet, och en av de främsta orsakerna till minskningen av kloridinträngning är också minskningen av poranslutning som orsakas av SCM. En förenklad modell baserad på formationsfaktorn för hcp kan användas för att uppskatta kloridmigrationskoefficienten.

Den uppdaterade enheten ger tillförlitlig icke-destruktiv övervakning av betonghärdning genom att mäta elektrisk ledningsförmåga och intern temperatur noggrant. Formationsfaktorn och ultraljudspulshastigheten är tillförlitliga indikatorer för betongstyrka. Korrelationer mellan tryckhållfasthet och dessa index har etablerats, med bildningsfaktorn som uppvisar mycket högre noggrannhet. Denna studie ger insikter i mekanismen för vatteninteraktion med cementbaserade material och en ny icke-destruktiv metod för att främja tillämpningen av SCMs i hållbara betongar.

**Nyckelord:**

Alternativa bindemedel; hållbarhet; hydratisering; beständighet; elektrisk ledningsförmåga; formationsfaktor; mikrostruktur; fuktransport

# Acknowledgement

I would like to express my sincere appreciation to my supervisors, Luping Tang and Zhenghong Yang, for their invaluable guidance and support throughout my research journey. The insightful discussions with them have played a critical role in the development of novel ideas and overcoming research challenges. I am also grateful to my assistant supervisors, Ingemar Löfgren, Nilla Olsson, Jan Swenson, and Itai Panas, for their helpful input in experimental design and results interpretation during reference group meetings.

I would like to extend my gratitude to Lars Wadsö and Ingemar Segerholm for their collaboration in the laboratory work and their constructive feedback on the experiments. Special thanks are also due to my colleagues in the building materials group, Arezou Baba Ahmadi, Helén Jansson, Shunfeng Wang, Yongqiang Li, Samuel Armistead, and Amrita Hazarika, for their inspiring discussions and fruitful collaborations. I am also grateful to my colleagues in the Division of Building Technology and WET for their support in laboratory work and the pleasant discussions during fika time, which have provided me with much-needed energy and motivation during the challenging period of the COVID-19 pandemic. I would like to thank the colleagues in the Physics and Chemistry department for their collaboration in the experimental testing. Lastly, I would like to express my appreciation to my family for their unwavering support throughout my academic and personal endeavors.

I am grateful for the financial support provided by the Swedish Research Council for Environment, Agricultural Sciences and Spatial Planning (FORMAS) [Grant No. 2018-01430] and the National Key Research and Development Program of China [No. 2018YFD1101002]. I also appreciate the partial financial support from Thomas Concrete Group, SBUF (the construction industry's organization for research and development), and Cementa AB.

*Liming Huang*

Gothenburg, March 2023.

## List of Publications

This dissertation is mainly based on the work presented in the following publications:

I. L. Huang, L. Tang, H. Gu, Z. Li, Z. Yang, New insights into the reaction of tricalcium silicate ($C_3S$) with solutions to the end of the induction period, Cem. Concr. Res. 152 (2022) 106688. https://doi.org/10.1016/j.cemconres.2021.106688.

II. L. Huang, L. Tang, I. Löfgren, N. Olsson, Z. Yang, Real-time monitoring the electrical properties of pastes to map the hydration induced microstructure change in cement-based materials, Cem. Concr. Compos. 132 (2022) 104639. https://doi.org/10.1016/j.cemconcomp.2022.104639

III. L. Huang, L. Tang, L. Wadsö, I. Löfgren, N. Olsson, Z. Yang, Using water vapour and $N_2$ isotherms to unveil effects of SCMs on nanopores and evaluate hydration degree, Cem. Concr. Res. 164 (2023) 107042. https://doi.org/10.1016/j.cemconres.2022.107042.

IV. L. Huang, H. Jansson, J. Swenson, L. Tang, Z. Yang, Distribution and dynamics of water in the blended pastes unraveled by thermoporometry and dielectric properties, (2023). Submitted manuscript.

V. L. Huang, L. Tang, I. Löfgren, N. Olsson, Z. Yang, Y. Li, Moisture and ion transport properties in blended pastes and their relation to the refined pore structure, Cem. Concr. Res. 161 (2022) 106949. https://doi.org/10.1016/j.cemconres.2022.106949.

VI. L. Tang, D. Boubitsas, L. Huang, Long-term performance of reinforced concrete under a de-icing road environment, Cem. Concr. Res. 164 (2023) 107039. https://doi.org/10.1016/j.cemconres.2022.107039.

VII. L. Huang, L. Tang, I. Löfgren, N. Olsson, A. Ahmadi, O. Esping, Y. Li, Z. Yang, Non-destructive test system to monitor hydration and strength development of low $CO_2$ concrete, (2023). Submitted manuscript.

## Additional Publications

Other publications that are related to the content of the thesis are listed below.

VIII. L. Huang, Z. Yang, Early hydration of tricalcium silicate with potassium hydroxide and sulfate from pore solution and solid view, Constr. Build. Mater. 230 (2020) 116988. https://doi.org/10.1016/j.conbuildmat.2019.116988.

IX. L. Huang, L. Tang, I. Löfgren, N. Olsson. Water distribution in green cementitious materials under different relative humidity, *proceedings of ERICA-CASH II Final Conference*, January, 25–27, 2021, Heidelberg, Germany.

X. L. Huang, Water and alkali salts in the hydrating and hardened green cement-based materials: Hydration process, moisture content and transport, Licentiate thesis, Chalmers Tekniska Högskola (Sweden), 2022.

XI. L. Huang, L. Tang, Z. Yang, The hydration and drying of concrete monitored by the array sensors, *proceedings of 24th NCR symposium*, August 17–19, 2022, Stockholm, Sweden.

# Contents

**Abbreviations**

| | |
|---|---|
| *w/b* | Water to binder ratio |
| $C_3A$ | Tricalcium aluminate |
| $C_3S$ | Tricalcium silicate, alite |
| C-S-H | Calcium silicate hydrate |
| GEMS | Thermodynamic modelling software GEM-Selektor v3.7 |
| hcp | Hardened cement-based paste |
| LT-DSC | Low temperature differential scanning calorimetry |
| PSD | Pore size distribution |
| RCM | Rapid chloride migration method |
| RH | Relative humidity |
| SCMs | Supplementary cementitious materials |
| SEM | Scanning electron microscopy |
| UPV | Ultrasonic pulse velocity |
| VFT | Vogel-Fulcher-Tammann equation |
| BET | Brunauer-Emmett-Teller |

***Major notations***

| | |
|---|---|
| $\sigma_{ps}$ | Electrical conductivity of pore solution |
| $\sigma_p$ | Electrical conductivity of paste |
| $\sigma_c$ | Electrical conductivity of concrete |
| $F$ | Formation factor |
| $\beta$ | Pore connectivity index |
| $D_v$ | Vapour diffusion coefficient at steady state |
| $D_w$ | Total moisture transport coefficient |
| $D_{v,s}$ | Vapour diffusion coefficient by semi-infinite drying |
| $D_{RCM}$ | Chloride migration coefficient by RCM test |
| $RH_s$ | Equilibrium relative humidity at the solution surface |
| $RH_o$ | Observed relative humidity in cylinder pores |
| $\alpha$-$F$ | Average growth rate of formation factor |
| $\alpha$-$UPV$ | Average growth rate of ultrasonic pulse velocity |
| $f_c$ | Compressive strength |
| $\phi$ | Water porosity |
| $\phi_c$ | Critical volume for percolation of water in hcp |
| $\Phi_0$ | Porosity at which the strength vanishes |
| $E_a$ | Activation energy |

# 1 Introduction

*In this chapter, a concise background of the research area will be presented in section 1.1. The aim of this dissertation will be outlined in section 1.2. The following section, 1.3, will introduce the framework of this dissertation that internally links the different research topics. Finally, the limitations of experimental investigation and framework will be discussed in section 1.4.*

## 1.1 Background

Risks of climate change have emerged gradually and some of them make direct influence on our daily life, such as causing the rise of the sea level and the increase in frequency of severe weather. Some others effects do not directly impact our current life but they are vital for future of homo sapiens [1]. To ensure a habitable climate for present and future generations, it is imperative to achieve the goal of net-zero by significantly reducing greenhouse gas emissions. Concrete is the most widely-used construction materials in the world due to its critical role in housing, transport infrastructure, hydroelectric dams and wind farms. Although the embodied $CO_2$ emission and energy for the production of one kilo of concrete is lower than most other construction materials, emission from cement clinker production becomes a challenging problem due to the massive demand of concrete [2]. The global production of cement in 2021 is around 4.3 Gt, among which China is accounting for about 55 %, followed by India (8 %), the European Union (4 %) and the United States (2 %) [3]. The total production is expected to grow up to 4.68 Gt in 2050 [4]. Traditional production process of ordinary Portland cement consumes fuel (e.g. coal) in the energy supply and releases massive $CO_2$ from the decomposition of calcium carbonate (accounting for approximately 60 % of the emissions). It is the third largest energy-consuming industry, which accounts for 6–7 % of anthropogenic $CO_2$ emissions and 4–5 % of greenhouse gases [5,6].

The effective solutions for reducing emission in the cement industry mainly include using green energy source, carbon capture and storage technologies, and reducing the Portland clinker

content in the cement. On the way to net-zero at 2050, it requires to make cement with clinker portion lower than 0.69 at 2025, and that lower than 0.56 also with 95 % of $CO_2$ from cement production stored [7]. Substituting clinker with supplementary cementitious materials (SCMs) is the most efficiency way to lower the clinker content in cement [8]. Furthermore, a prolonging of the service life by improving the durability of constructions is a good way to reduce emissions. In the net-zero emission scenario, the longer building lifetimes will result in a 13 % reduction in cement demand by 2050, compared to a baseline scenario with limited material efficiency [3].

SCMs significantly influence the hydration of ordinary Portland cement and the microstructure of hardened cement-based paste (hcp), which consequently affect the properties of fresh mix (setting time and rheology), the hardened properties, and thus the durability of concrete. Hydration of cement blended with SCMs is an interaction between water and these binders. This process involves the dissolution of minerals and the followed precipitation of hydration products from pore solution [9,10]. Water plays a crucial role in the reaction of cementitious materials. It acts as a "carrier" to dissolve ions from mineral surfaces and as "component" to form the chemical structure of hydration products.

Reaction of minerals in clinker with water would be altered by the SCMs. Escalante-García and Sharp [11] found that the hydrations of tricalcium silicate ($C_3S$), tricalcium aluminate ($C_3A$), and ferrite phase were accelerated by the replacement of SCMs, while pulverized fly ash did not accelerate $C_3S$ hydration as much as other alternative materials. Hydration of dicalcium silicate ($C_2S$) was retarded by fly ash at higher temperatures, but it was accelerated by slag or volcanic ash. Many previous publications proposed that the driving force of early hydration is the undersaturation with respect to the dissolution of alite/tricalcium silicate ($C_3S$) [12–16]. The presence of limestone can accelerate this process by causing a higher undersaturation degree. Conversely, high concentrations of aluminum, which are dependent on the type and chemical composition of SCMs, have a retarding effect on the reaction. Interestingly, high calcium concentrations do not have any adverse effect on hydration kinetics [17,18].

The typical SCMs, such as slag and fly ash, generally have slower reaction rates than the main clinker phase, so it leads to a lower early strength as the SCMs replacement level is increased. Nevertheless, alkali metal sulfates can significantly enhance strength development at both early and later ages while improving workability [19]. After a sufficient curing time, it may induce a refinement in the pore structure, increase in bound water content and cumulative heat release, reduction in portlandite and calcium aluminate monosulfate (AFm) contents, and increase in ettringite content. The dosage of alkali metal sulfates can be adjusted to improve both early and long-term strength of the activated slags based binders [20].

Addition of alkali metal sulfates also impacts the hydration of $C_3S$ [21,22], resulting in changes to the setting and rheology of fresh pastes, as well as the microstructure of both plain and blended concrete [23,24]. During the hydration process without introducing extra alkali salts, the calcium silicate hydrate (C-S-H) phase grows with a morphology of long needle-like structure which eventually link together. In contrast, the presence of alkali metal sulfates or calcium sulfates results in C-S-H growing in a dispersed and needle-like morphology. Furthermore, the sole addition of alkali metal ions causes the formation of a short tree-shaped C-S-H adhering to the surface of the unhydrated particles [22,25]. These different build-up patterns result in a significant difference in the pore structure, ultimately affecting the strength, shrinkage, and durability of the hardened cement-based materials.

The durability of concrete is characterized by its capacity to withstand adverse environmental factors, such as chemical exposure, weathering, and abrasion, while maintaining its initial shape, quality, and intended function [26]. The initial signs of durability issues manifest as material deterioration, which may not pose an immediate safety concern. However, they can gradually lead to structural damage, potentially endangering the integrity of the structures. The presence of water significantly influences the deterioration process of cement-based materials due to its control over transport properties [27,28] and corrosion reactions [29]. Moreover, water confined in hcp plays a critical role in the freezing-thawing damage [30,31] and alkali-silica reaction [32], as these processes are highly sensitive to the amount of water present. Therefore, understanding the effect of SCMs on interaction of water with hcp is crucial for the development of durable concrete structures.

Effects of SCMs on the chloride transport properties have been investigated through experimental and modeling approaches [33–36]. However, only a limited number of publications shed light on the moisture transport properties of hcp containing SCMs. Baroghel-Bouny [37] reported that the addition of 8%–10% silica fume in concrete reduced the apparent moisture diffusion coefficient of hcp at a saturation degree higher than 50%. Saeidpour and Wadsö [38] conducted an investigation on the vapor diffusion coefficient of blended mortar during adsorption and desorption processes using a cup method. They observed that silica fume and slag could reduce vapor transport coefficient reduced by one order of magnitude, which was ascribed to the higher amount of gel pores and lower volume of capillary pores in the blended system. Olsson et al. [39] reported similar effects of silica fume and slag on vapor diffusion coefficient, and it was more pronounced at higher relative humidity levels. Linderoth [40] found that fly ash did not reduce the pore volume but still refined the pore structure. This caused a decrease in moisture diffusion coefficients by a factor of 2 to 5 after one-year curing. The addition of aggregates had very limited effect on the measured pore structure and sorption isotherms of mortar.

The moisture content is a significant factor that affects the chloride ingress in hcp. Chloride migration coefficient becomes higher at a higher moisture level [41]. This is crucial for the understanding and modelling of concrete structures exposed to different environments such as de-icing salt road and marine environments [42]. Leaching, as a kind of interaction with water, leads to change of the microstructure and a peak phenomenon in chloride profile of the exposed concrete. In addition, the splashing zone experiences high frequencies of wet-dry cycles, causing the anomalous chloride profiles in the near surface zone. These factors highlight the importance of considering the effect of moisture content on chloride ingress in hcp containing SCMs.

The deterioration processes are intrinsically determined by the interaction of water and ions in the microstructure of hcp [43,44]. Influence of SCMs on the microstructure and chemical structure of main hydration products, calcium-silicate-hydrate (C-S-H), has been a subject of significant research interest. Berodier and Scrivener [45] found that incorporating SCMs resulted in a lower volume of hydration products than in pastes made with ordinary Portland cement, which in turn increased the total porosity hcp. However, the pore structure was refined due to the filling effect of later age hydration products from SCMs. Several studies have reported that the addition of slag can reduce total porosity at an early stage and refine the pore structure [46]. In previous investigations, it was found that blending of silica fume, fly ash, slag, and metakaolin altered the elastic modulus of hydration products. The specific trend of change is closely related to the water to binder ratio (*w/b*) and the amount of SCMs [47,48]. It was also shown that the incorporation of SCMs has no effect on the performance of two different types of C-S-H, but it increases the percentage of high density C-S-H in hydration products [49]. A clear understanding of these changes in microstructure and properties is important for assessing the performance of concrete containing SCMs.

Water confined in the microstructure of hcp exhibits distinct structural and dynamical properties from bulk water [50–52]. Behavior of water in hcp at low temperature is a crucial factor in determining the frost damage of cement-based materials. The phase transition of freezable water to ice creates hydraulic pressure by expelling the unfrozen water, and it causes the cryo-suction process that forces the liquid to move towards the frozen sites [53]. These water migration processes are closely related to the distribution of freezable and unfrozen water in the porous matrix, as well as the dynamics of water confined in the nanosized pores. However, there is a lack of a comprehensive and general understanding of the confined water dynamics in hcp. Thus far, no investigation has been undertaken to explore the influence of SCMs on the water dynamics in hcp.

Use of SCMs for production of low $CO_2$ concrete affects the reaction kinetics, meaning deviation in early hardening properties such as setting time and the strength development. The

transition of a fluid to a hardened state during the hydration process governs the construction progress, the quality, and cost of the concrete structures. The hardening process determines the appropriate time for demoulding and further procedures. Furthermore, the evolution of the specific yield stress, as pointed out by Reiter et al. [54], is of great significance for digital fabrication (3D printing) due to the loading of concrete during fabrication. Traditional off-site quality control methods are time-consuming and require manual operation, making them inadequate for the quality control of fast or automated construction [55]. Additionally, hardening is known to be sensitive to temperature changes, so traditional methods must control the temperature and humidity of the environment, which can differ from the actual field site, particularly during the construction of large concrete structures [56]. Therefore, an efficient and high-quality non-destructive testing method would be very helpful in mitigating these problems in the use of SCMs in construction and digital fabrication.

## 1.2 Objectives

Replacement of cement clinker with SCMs is effective to reduce emissions in construction sectors. Slag and fly ash, sometimes with limestone, are the most widely and well-used alternative binders for making sustainable concretes. This thesis aims to investigate the interaction of water with the cement-based materials blended with large amount of these SCMs. The interaction at initial stage is called hydration in terminology of cement research. Reaction in this period will determine the workability of cement-based materials, which will also furtherly influence the performance of the materials at hardened state. Hydration of binders consumes the water and produces new phases to induce the transition of a flowable fresh state to a rigid hardened state thereby building links between particles. Space between the particles will be filled gradually as the hydration continues to reach a certain degree. Microstructure has been formed during the hydration and hardening process. It determines the deterioration process of the cement-based materials caused by the interaction with water and ions from the environment in service. To understand the effects of SCMs and their related ions on the above-mentioned properties, the subsequent problems have been tackled in the current work:

- How does water interact with the main mineral $C_3S$ with the presence of $C_3A$, $K_2SO4$ and KOH at the early stage thereby focusing on the nucleation of hydration products?

- How does the SCMs influence microstructure of pastes during the hydration up to the main peak, as determined by a novel in-situ monitoring method?

- What is the underlying mechanism between the interaction of water with the porous structure of the hardened pastes with SCMs and its reflection of the microstructure?

- How do SCMs modify the moisture and ion transport in hcp, and which parameter is the key determinant of the moisture and chloride transport properties?

- How does the upgraded non-destructive method work for onsite monitoring of hydration and strength development.

## 1.3 Thesis framework

This dissertation is dedicated to investigating the interaction of water with cementitious materials containing large volume of SCMs, spanning from the early stages to the long-term service. It mainly includes the content of 7 related papers as shown in Figure 1.1. Chapter 1 is about the background, objectives, framework, and limitations of this dissertation. Chapter 2 describes the information of materials, experimental procedures and test methods applied during the study. Chapter 3 to 6 demonstrates the main experimental results and discussions.

Chapter 3 starts with questioning the correlation between the dissolution rate and hydration rate of main minerals in the bulk pore solution. A novel hypothesis is proposed to understand the hydration mechanism with respect to the precipitation of C-S-H through a non-classical nucleation process. The research subject has expanded from pure minerals to SCMs substituting Portland cements. Effect of SCMs and *w/b* on the hydration induced microstructure change has been investigated in detail. This chapter comprises the content of paper I and II.

Chapter 4 consists of content from papers III and IV. Paper III presents a comparative study of pore structure in hcps with SCMs by water desorption isotherm. Dynamic water vapor desorption data were used to calculate the pore size distribution based on the principles of interaction between water and porous structure of hcp. Paper IV explores the correlation between water behavior and microstructure of hcp by thermoporometry method. The dynamics of water confined in nanopores were also characterized by broadband dielectric spectroscopy. The interaction of water with hcp was studies under various low temperatures conditions.

Chapter 5 comprises content of paper V and VI to discuss the effect of SCMs on the moisture and chloride transport in hcps. The moisture transport and chloride migration in the blended materials were correlated to the pore structure. Refinement effect of SCMs on the microstructure will be clearly indicated by a comprehensive analysis of various parameters indexing the pore structure.

Chapter 6 presents the main results of paper VII, in which an upgraded design of device was used to monitor the hydration and hardening of concrete containing SCMs. The monitored properties will be correlated with traditional indices measured by standard methods. The

function of upgraded device will be evaluated by comparison with the widely used method, ultrasonic pulse velocity test.

Chapter 7 concludes the major findings in this study and proposes prospects for future research to address the unresolved problems.

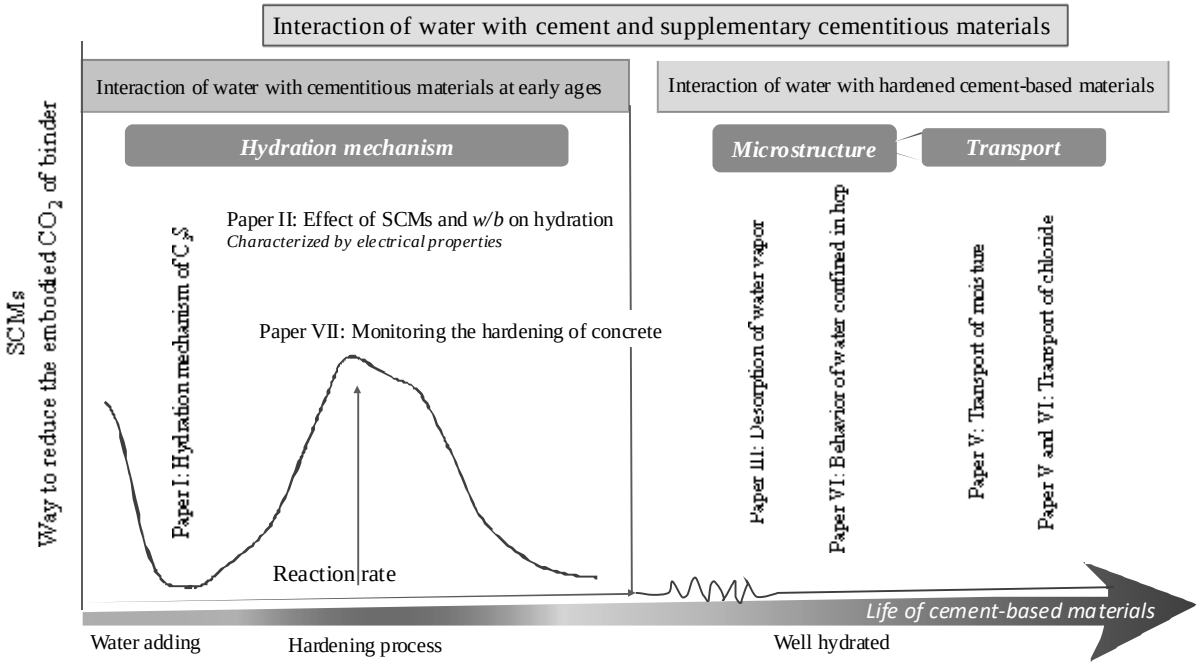


Figure 1.1. The research framework of this dissertation.

## 1.4 Limitations

The oxide compositions of binders were determined using X-ray fluorescence, and therefore they do not represent the actual concentration of dissolvable alkalis in materials. Because the conductivity of the pore solution is influenced by the types and concentrations of ions in pore solutions, solubility of the chemical composition is important for accurately predicting the electrical conductivity of the pore solution. To address this problem, a modification of the equation for calculating alkali concentration was introduced, but some discrepancies still exist between the calculated and actual concentrations due to the inaccurate evaluation of calcium and sulfate ions in the pore solution. Furthermore, this study was only focused on three kinds of SCMs, but there are many newly emerging alternative materials, such as calcined clay. Validation of the method with other SCMs is needed for promoting its application.

The method for determining water content in hcp neglects the effect of carbonation, which may overestimate the evaporable water content, although the effect is very minor in the early stages of hydration. Because the moisture transport coefficient was measured with small samples, the size effect needs to be considered if the model is to be applied for predicting moisture transport

in practical concrete structure.

Some assumptions in this dissertation may need further verification. It was assumed that the solvent exchange treatment by isopropanol had similar effects on morphology of hydration products for all samples, and the freeze-dry had the negligible effects on the sizes and number of etch pit on particles surface. This makes impact on the discussion based on the size of nucleated particles. The freezing and thawing experience will alter the microstructure and the moisture distribution in hcps. Although the experimental results showed that the fast low-temperature DSC test had minor nonreversible effects, the reversible effect needs to be assessed for a good understanding of real moisture state in hcps. For the estimation of hydration degree with desorption data, it was assumed that the water amount in the interlayer of C-S-H is similar in SCMs blended hcp. The presence of slag and fly ash reduces the Ca/Si ratio in C-S-H, and in turn it lowers the water content in the interlayers. Neglecting this change leads to an underestimation of the hydration degree due to the lower calculated C-S-H content based on water vapor sorption.

The primary focus of investigation was on the moisture transport properties of paste. However, the presence of aggregates in concrete results in different moisture transport behavior as compared to hcp. Hence, it is necessary to conduct further research to extend the applicability of the theory from hcp to concrete by considering the interfacial transition zone and volume of aggregates. Monitoring of concrete was conducted on a lab scale without considering the presence of reinforcement in practical. The steel bar is high conductive component and may alter the calibration factors, possibly limiting the use of parameters in this study to a real construction.

# 2 Materials and methods

*This chapter presents an overview of the raw materials, the procedures employed for mixing and casting, and the measurement settings of various machines. Furthermore, an upgrade of test system for monitoring conductivity will be elaborated. In addition, methods are introduced to determine the moisture content in hcp.*

## 2.1 Raw materials

### 2.1.1 Minerals and salts

Pure minerals, including triclinic tricalcium silicate ($C_3S$) and cubic tricalcium aluminate ($C_3A$), were procured from DMT Materials Technology Co., Ltd. The specific surface area of $C_3A$ powder was measured to be 1.26 $m^2/g$ by BET method with $N_2$ sorption. $C_3S$ powder has a purity of 98.57 % (Rietveld refinement results from [57]), with a specific surface area of 1.92 $m^2/g$. The in formation of particle size distribution of $C_3S$ powder is available in [58]. Analytical reagents like sulfuric acid, LiCl, NaCl, KCl, KOH, $K_2SO_4$ and $Mg(NO_3)_2$ were employed for the experimental investigation as additives or relative humidity (RH) controller. Superplasticizer (PCE) used in the concrete samples was Master Glenium 5118 (with 17.5 % dry substance) purchased from Master Builder Solutions.

### 2.1.2 Cement and supplementary cementitious materials

The cement in all experiments is the Portland cement (CEM I 52.5 R) from Cementa with a Blaine surface of 525 $m^2/kg$. To substitute the Portland cement, three types of SCMs were used: ground granulated blast-furnace slag with a Blaine surface of 420 $m^2/kg$ from Thomas Cement, fly ash from Cementa, and limestone powder from Nordkalk. The type of limestone is Limus 15 with a $D_{50}$ of 18 µm. Table 2.1 shows the chemical composition of each binder referred to [59]. The limestone consists of approximately 89 % calcite and 9 % $SiO_2$. The detailed information about particle size distribution of the binders is presented in [58].

Table 2.1. Chemical composition of different binders (*LOI*: loss of ignition; $\delta_i$: mole of chemical composition per gram binder).

| Chemical Composition | CEM I 52.5 R | | Slag | | Fly ash | | Limestone |
|---|---|---|---|---|---|---|---|
| | wt % | $\delta_i$(mol/g) | wt % | $\delta_i$(mol/g) | wt % | $\delta_i$(mol/g) | wt % |
| CaO | 62.2 | $1.11\times10^{-02}$ | 39.11 | $6.98\times10^{-03}$ | 5.1 | $9.11\times10^{-04}$ | 49.5 |
| $SiO_2$ | 19.6 | $3.06\times10^{-03}$ | 36.63 | $5.72\times10^{-03}$ | 54.6 | $8.53\times10^{-03}$ | 9.0 |
| $Al_2O_3$ | 4.5 | $4.41\times10^{-04}$ | 13.56 | $1.33\times10^{-03}$ | 22.4 | $2.20\times10^{-03}$ | 0.6 |
| $Fe_2O_3$ | 3 | $1.88\times10^{-04}$ | 0.49 | $3.06\times10^{-05}$ | 8.7 | $5.44\times10^{-04}$ | 0.3 |
| $SO_3$ | 3.5 | $4.38\times10^{-04}$ | 0.27 | $3.38\times10^{-05}$ | 0.8 | $1.00\times10^{-04}$ | 0.03 |
| MgO | 3.5 | $8.75\times10^{-04}$ | 8.52 | $2.13\times10^{-03}$ | 1.8 | $4.50\times10^{-04}$ | - |
| $K_2O$ | 1.01 | $1.07\times10^{-04}$ | 0.57 | $6.06\times10^{-05}$ | 2.1 | $2.23\times10^{-04}$ | 0.3 |
| $Na_2O$ | 0.27 | $4.35\times10^{-05}$ | 0.42 | $6.77\times10^{-05}$ | 1 | $1.61\times10^{-04}$ | 0.1 |
| Cl | 0.07 | $1.97\times10^{-05}$ | 0.009 | $2.54\times10^{-06}$ | - | - | - |
| Sulfide | - | - | 0.73* | - | - | - | |
| *LOI* | 2.5 | | -1.07 | | 3.5 | | 40.1 |

**Note*: The sulfide in slag will be oxidized during the LOI test, so this induces an increase of weight. Although the hydration also makes oxidization of sulfide [60], we assume that its oxidization is rare due to the low hydration degree at the early age.

### 2.1.3 Aggregates

Aggregates used in the casting of fly ash blended concrete (C145) and slag blended concrete with *w/b* of 0.55 (C255) were siliceous type, and they were obtained from the building materials market in Gothenburg. The loose bulk density of the aggregates, which consists of sand and stones with a size distribution ratio of 85.2 %:14.8 % (1–4 mm: 4–10 mm), is $1.74 \times 10^3$ kg/m$^3$, while the close packing density is $1.96 \times 10^3$ kg/m$^3$. Different aggregates were used for casting the slag blended concrete with *w/b* of 0.45 (C245) and ternary concrete (C338). Sand with a density of $2.66 \times 10^3$ kg/m$^3$ was sourced from Eurosand, and stones with a density of $2.85 \times 10^3$ kg/m$^3$ were obtained from Skanska.

## 2.2 Preparation of samples

### 2.2.1 Hydration of minerals

The hydration of $C_3S$ and $C_3S$:$C_3A$ (wt, 90 %:10 %) mixture system was investigated using different solutions including deionized water, KOH solution, and $K_2SO_4$ solution. The solid to solution ratio was 0.5, and the samples were stirred for 1 min in a glovebox filled with $N_2$ gas and then cured under such an environment to avoid carbonation before hydration stopping. The hydration was stopped by two different methods, solvent exchange with isopropanol and freeze drying by immersing the samples into liquid nitrogen. The detailed description of sample treatment procedure can be found in paper I and VIII.

To investigate the hydration of $C_3S$ under high solution to solid ratio conditions, 0.1 g of $C_3S$ was mixed with 10 g (ratio of 100:1) and 20 g (ratio of 200:1) solutions in an ampere bottle. The mixture was then quickly placed into the channels of a calorimeter. To collect sufficient

solid residue for other tests, parallel experiments were conducted using materials five times the amount used in the calorimetry test. Solid residues were obtained by suction filtration, and they washed three times with an adequate volume of isopropanol to stop hydration. The washed residues were then vacuum dried at 40 °C for 48 h and sealed in a tube for analysis.

### 2.2.2 Preparation of cement-based materials

The mixture proportion of 11 paste samples is presented in Table 2.2. To create binary systems, Portland cement was substituted with 35 % fly ash or slag by weight. In the ternary system, Portland cement was replaced with 35 % slag and 16 % limestone. The pastes were mixed with three different *w/b* of 0.35, 0.45, and 0.55, except for the fly ash pastes with two *w/b* (0.35 and 0.45), as the future availability of fly ash is limited.

Table 2.2. The mixture proportion of pastes.

| Samples | Binders | | | | *w/b* |
|---|---|---|---|---|---|
| | Cement | Fly ash | Slag | Limestone | |
| P035 | 100 % | - | - | - | 0.35 |
| P045 | | | | | 0.45 |
| P055 | | | | | 0.55 |
| P135 | 65 % | 35 % | - | - | 0.35 |
| P145 | | | | | 0.45 |
| P235 | 65 % | - | 35 % | - | 0.35 |
| P245 | | | | | 0.45 |
| P255 | | | | | 0.55 |
| P335 | 49 % | - | 35 % | 16 % | 0.35 |
| P345 | | | | | 0.45 |
| P355 | | | | | 0.55 |

Pastes were mixed by a planetary mixer with 100 stainless steel balls (16 mm in diameter) in the bowl to ensure homogeneity. The mixer's agitator speed was set at 75 revolutions per minute with 7 rotations per revolution to prevent ball bouncing. Detailed description of mixing procedures was illustrated in the licentiate thesis [58]. After well-mixed, pastes were casted in different containers for further experiments.

Some specimens were cast in zip bags with dimensions of 150 mm × 200 mm. To facilitate the subsequent crushing, the freshly mixed pastes were rolled to a uniform thickness of approximately 1 mm prior to bag sealing. After a week of sealed curing, all samples were removed from the bags and crushed to particles with sizes around 1 mm. These particles were then cured in water within a sealed container of 1 L volume, with a control of the water mass (about 15 % of the particle mass) to ensure sufficient moisture but minimize leaching.

After being water-cured for two months, a portion of the particles was transferred to conditioning boxes maintained at four different levels of relative humidity (97.6 %, 75.5 %, 54.4 %, and 33 %), which were controlled by saturated salt solutions at 20 °C. Measurements

were conducted on samples that had been conditioned for 1.5 years. The total amount of evaporable water content in these samples was determined by subjecting the particles to vacuum drying at 25 °C for a week. Additionally, after 6-month curing a subset of each sample was conditioned at 11 % relative humidity, controlled by a saturated LiCl solution, for one year. The curing temperatures were held constant at 20 ± 1 °C throughout the experiment.

Some fresh paste was cast in polypropylene tubes and sealed with lips. To prevent inconsistencies caused by bleeding, the tubes were placed on a rotator at a speed of 12 rpm for 24 h. The samples were then stored in a curing room with a constant temperature of 20 °C for a period of 390 days (d). Afterwards, the tubes were wet cut properly from the top with a constant water flow using an electric diamond saw. Details about the cutting protocol are described in [28] for the measurement of moisture transport properties.

Table 2.3 shows the mixture proportion of concretes containing SCMs. Concretes were mixed using a self-falling mixer with a capacity of 50 liters. The water and binder were initially mixed for 2 min, and then the aggregates were gradually added to the mixer and mixed for an additional 5 min. The fresh concretes were cast into a container as depicted in Figure 1 (left side), and a board with an array of sensors was fixed in the container before casting. Once the container was filled to a specified height (10 mm above the first row of sensors), it was carefully vibrated if needed, and then sealed at the top to ensure minimal moisture loss. The samples were then placed in the laboratory room at either Chalmers (22 ± 1 °C) or Thomas concrete lab (19 ± 1 °C), and data collection from conductivity test began approximately 10–20 min after mixing with water.

Table 2.3. The mixture proportion of concretes (kg/m$^3$).

| Mix ID | Cement | Slag | Fly ash | Limestone | Water | PCE | Sand (<4 mm) | Coarse aggregate (4–10 mm) |
|---|---|---|---|---|---|---|---|---|
| C145 | 286 | | 154 | | 201 | 3.2 | 1411 | 246 |
| C245 | 280 | 151 | | | 194 | 3.0 | 954 | 795 |
| C255 | 247 | 133 | | | 209 | 2.7 | 1449 | 256 |
| C338 | 242 | 173 | | 79 | 187 | 4.0 | 953 | 780 |

## 2.3 Measurement procedures

### 2.3.1 Monitoring of electrical conductivity

Electrical conductivity of paste was tested by four electrodes positioned in the Wenner configuration [61]. The old setup of the device and measuring procedure have been illustrated in detail in paper II and licentiate thesis [58,59].

The monitoring system was upgraded in paper VII to measure the hydration of concrete at

various depths by accounting for temperature and dimension effect. Figure 2.1 presents the updated version based on the previous system, which includes an additional sensor to measure the temperature at each row. These sensors were calibrated to provide an accuracy of ± 0.2 °C. The measurement of each depth was performed sequentially, from the top to the bottom of the sample, and each instant measurement took approximately 0.1 seconds. Data were recorded every 5 min during the first 24 h and then every 10 min from 1 day to 7 d. Subsequent data was collected at selected ages, such as 14 and 28 d, to capture the later stages of hydration.

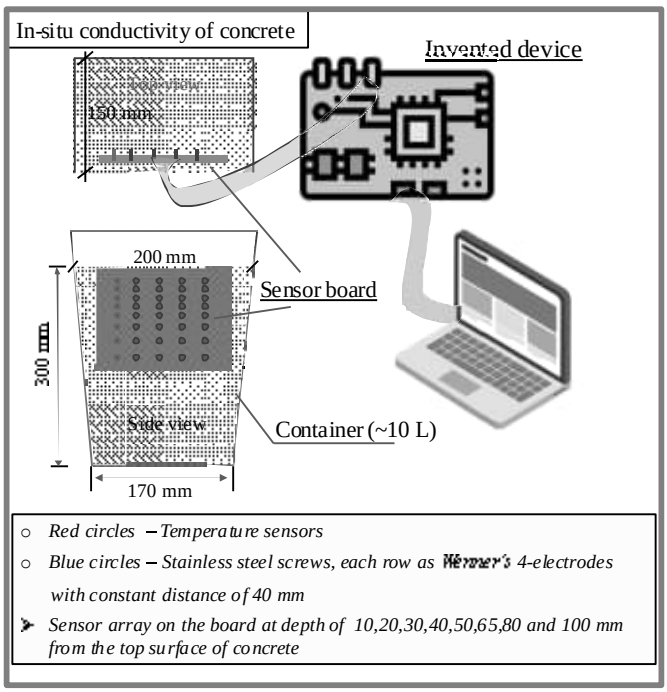


Figure 2.1. The setup for conductivity monitoring of concrete samples.

The impact of temperature on the electrical conductivity of concrete has been taken into consideration. The activation energy ($E_a$ = 13.375 kJ/mol) was determined using the Arrhenius equation, Eq. (2.1), based on the measured conductivity in mimic pore solutions conditioned between 3 and 70 °C. In the equation, "$A$" represents the pre-exponential constant, "$R$" is the gas constant (8.314 J/K mol), and "$T$" represents the absolute temperature of the specimen.

$$\sigma = A \cdot e^{\frac{E_a}{RT}} \tag{2.1}$$

Wenner's method is used to calculate the electrical conductivity of concrete with assumption of a semi-infinite boundary, which is not always met in practical applications, particularly for the upper rows of sensors. The dimension factors at different depths have been modelled with COMSOL Multiphysics software. To account for the effects of temperature and dimension on electrical conductivity, Eq. (2.2) was used to calculate the conductivity of hydrating concrete at various depths. The average conductivity for each sample was calculated with data from the

second to the eighth row.

$$\sigma_c = \frac{I}{2\pi \Delta V d} \gamma e^{\frac{Ea}{R}\left(\frac{1}{273.15+T} - \frac{1}{298.15}\right)} \tag{2.2}$$

where $\sigma_c$ is electrical conductivity of concretes normalized to 25 °C, $I$ is the applied constant current between the outer two electrodes, $\Delta V$ is potential difference between the two middle electrodes, $d$ is the distance between inner two electrodes and $\gamma$ is the dimension factor at different depths.

### 2.3.2 Moisture transport

Moisture transport properties in the hcp were measured by the invented tube method, which enables to test both vapor diffusion under steady-state conditions (constant flux through the samples) and total moisture transport under non-steady-state conditions by a semi-infinite drying. The detailed information of tube method is presented in paper V [28] with the equations to calculate the moisture transport parameters.

Measurements of vapor diffusion in pastes were carried out across four different RH intervals, namely RH97–75 (97.6–75.5 % RH), RH85–75 (85.1–75.5 % RH), RH97–50 (97.6–50 % RH), and RH75–50 (75.5–50 % RH). In addition, semi-infinite drying tests were performed in two distinct RH conditions, namely 75.5 % RH within a box and 50 % RH within a climate room. To prevent any potential leakage from the tube edges, a thin circle of moisture-tight glue (LOCTITE® 60 Seconds Universal glue) was applied around the edge. Each sample was weighed at various conditioning times, and 3 parallel measurements were done for each.

### 2.3.3 Ultrasonic pulse velocity

Figure 2.2 illustrates the setup for monitoring of ultrasonic pulse velocity (UPV), using the IP-8 Ultrasonic Measuring System from Ultratest GmbH. The system comprises two channels equipped with an acoustic emission system, a controller, and a computer. A transmitter and a receiver are placed within the silicon mould facing each other and inserted into the inner empty cylinder. The protrusion of approximately 3 mm inside the cylinder ensures a dense connection to the fresh concrete at a measurement distance of 50 mm. The ultrasonic pulse was set at a frequency of 25 kHz, and the velocity in the hydrating concrete normally ranges from 100 m/s to 5000 m/s at about 20 °C. To compact the concrete samples, a mild vibration was applied immediately after casting, and the mould was then connected to the controller for automatic control by the computer. Ultrasonic waves were recorded at a constant interval of either 2 or 5 min. Each sample underwent three parallel measurements, and the average value was taken as the result.

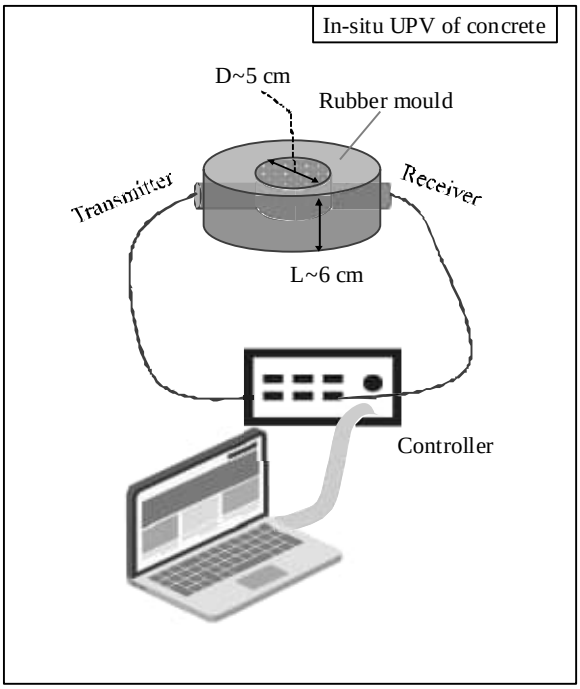


Figure 2.2. The setup for monitoring UPV in concrete samples.

### 2.3.4 Setting time

To measure the setting time of concrete, the penetration resistance test was carried out on the mortar part of the concrete mixture, in accordance with the traditional standard (ASTM C 403/C 403M – 05).

### 2.3.5 Compressive strength

Compressive strength measurements of the concrete samples were conducted in accordance with the EN 12390-3:2019 standard at several time points: 12 h, 24 h, 3 d, 7 d, 14 d, and 28 d. Notably, the dimensions of the C145 and C255 samples were 100×100×100 $mm^3$, while the C338 and C245 were cast as cubes of 150×150×150 $mm^3$. To ensure that a fair comparison could be made, the strength values of C145 and C255 were normalized using a dimension factor of 0.93 [62].

## 2.4 Methods

The licentiate thesis [58] has extensively covered several methods including X-ray diffraction, scanning electron microscopy (SEM), rapid chloride migration (RCM), and mercury intrusion porosimetry. Therefore, this dissertation will not describe the information of these techniques to avoid duplication.

### 2.4.1 Nitrogen sorption

A BET instrument (TriStar3000, Micromeritics) was used to measure the nitrogen sorption isotherm of samples. Before the sorption measurement, samples had been outgassed for 4 h with a continuous $N_2$ gas flow at 60 °C for a fast water removal. Adsorption isotherms were measured over the pressure range of 0.01–0.982 $P/P_0$ with an equilibrium interval of 10 s for each step at 77 K. Each sample has been repeated at least once, and the final value is an average of parallel tests.

### 2.4.2 Thermogravimetric analysis

The weight loss due to the decomposition of portlandite was measured by a thermogravimetric and differential thermal analysis instrument (SDT Q600, TA Instruments) with a Stanton Redcroft STA 780 simultaneous thermal analyser. Powder samples (dried at 11 % RH for 1 year) were heated at a rate of 10 °C/min under a continuous nitrogen flow (100 $cm^3$/min) from 20 °C to 1000 °C.

### 2.4.3 Isothermal calorimeter

Hydration heat release of samples was measured using an isothermal calorimeter called I-Cal 2000 HPC, manufactured by Calmetrix. The instrument is specifically designed for measuring the isothermal heat flow of cement-based materials, which has two configurations with two or eight sample cells. These cells are well-insulated from each other by a wide air gap, ensuring a high level of precision and stability by eliminating any cross-influence. The temperature was maintained at a stable 20 °C with an accuracy of ± 0.001 °C. Two parallel measurements were conducted simultaneously to obtain an average value.

### 2.4.4 Moisture content

Moisture content in the hcp at early ages (10 h to 12 d) was determined with an easily implementing procedure described in [59] based on the solvent exchange by isopropanol and vacuum drying at 60 °C.

Moisture content in pastes after curing for 390 d was measured to calculate the moisture transport coefficient. Pastes were additionally crushed into particles with a size less than 2 mm and conditioned under various RH levels (97.6 %, 75.5 %, and 50 %) in a box where calcium hydroxide was placed to absorb $CO_2$. After one year, the particles were weighed and subjected to a vacuum drying process at 60 °C for 3 d to determine the evaporable water content.

### 2.4.5 Low temperature differential scanning calorimetry

The Q2000 TA equipment was used to conduct the test of heat flow in powder samples. Samples, weighing approximately 20 mg, were placed in hermetically sealed pans with lips. Samples were firstly cooled from 20 °C to -60 °C with a rate of 2 °C/min, and then equilibrated for 5 min before reheated to 20 °C with the same rate. Samples conditioned at 97 % RH were measured with a second cycle using the same protocol. To better compare the signals of the different binder systems, a normalization was done to obtain a similar starting point of all curves for better comparison. A mimic pore solution was made by adding 150 mmol/L KCl and 50 mmol/L NaCl into the extracted pore solution of CEM I paste with a *w/b* of 1, and it was then measured with the same temperature procedure for evaluating the heat of fusion of the pore water in hcp.

### 2.4.6 Broadband dielectric spectroscopy

The powder samples, obtained from well-conditioned particles, were subjected to dielectric permittivity testing. The broadband dielectric spectrometer (Novocontrol Alpha-N) was used to measure the complex dielectric permittivity in the frequency range of $10^{-2}$–$10^{6}$ Hz. Tests were performed isothermally in the temperature range of 130–300 K with a temperature increment of 5 K, and with temperature deviation controlled to be lower than ± 0.1 K. The powder samples (about 0.5 g) were tightly held with a thickness of 0.2 mm in between parallel gold-plated electrodes, with a diameter of 10 mm (see Figure 2.3).

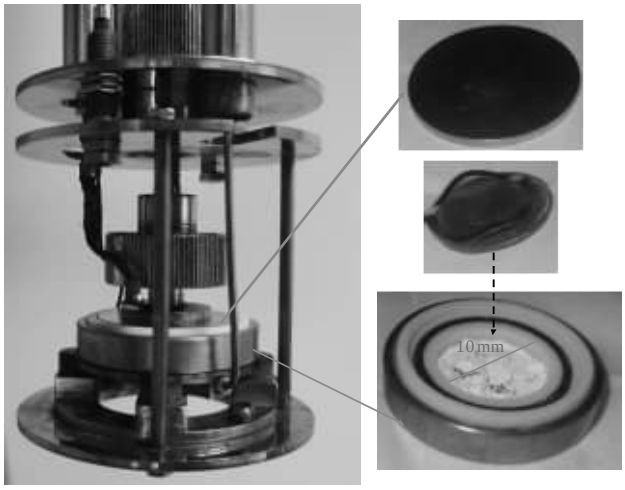


Figure 2.3. Holder for the broadband dielectric spectroscopy test of powder samples.

### 2.4.7 Dynamic water vapour isotherm

Water vapour desorption isotherms were measured on 6-month water cured samples. The measurement was carried out using a gravimetric water vapour sorption instrument, DVS (Advantage, Surface Measurements Systems, UK). The instrument continuously recorded the

mass of small samples during exposure to varying RH conditions. Samples weighing 40–60 mg were subjected to an RH sequence (95 %-90 %-80 %-70 %-50 %-40 %-35 %-30 %-20 %-10 %-0 %) at a constant temperature of 20 °C. To attain the criterion of mass loss rate lower than 0.0001 %/min, each RH step required a duration of 30–60 h. At least two samples were measured for each mix, and the final values are the average of parallel measurements.

### 2.4.8 Thermodynamic simulation

Thermodynamic modelling was carried out using GEM-Selektor v3.7, a freely available software for Gibbs energy minimization. The simulation was based on the cement database Cemdata18 [63] and the PSI-GEMS thermodynamic database [64]. It was applied to simulate the aqueous and gaseous species present in the pore solution of $C_3S$ over a range of pH values.

The influence of SCMs on the phase assemblage was simulated by assuming that the clinker had a hydration degree of 92.2 % after being cured in water for 6 months at 20 °C (based on the portlandite content determined by Thermogravimetric analysis). This value closely aligns with that reported in [65], which used a similar clinker composition and curing conditions.

# 3 Interaction of water with cementitious materials at early age

*This chapter will focus on the interaction of water with cementitious materials right after water addition to the main peak in hydration heat release. Theories for the early hydration of main minerals in cement are yet to have a good explanation for the result found in the experiments. Therefore, this chapter tries to propose a reasonable hypothesis for $C_3S$ hydration using experimental results and thermodynamic simulation. In practical application, SCMs substituting partial cement is the most common scenario. The interaction of water with the blended binders will be demonstrated by an in-situ test method to monitor the electrical properties of hydrating paste. Electrical conductivity of pore solution will be calculated based on the concentration of alkali metal, hydroxide, sulfate, and calcium ions. The content of this chapter is sourced from paper I, paper II, and graphs in papers VIII and X.*

## 3.1 Hydration of $C_3S$ with solutions

This section explores the hydration of $C_3S$ in various solutions. The preliminary result suggests that the dissolution theory regarding the thermodynamic property of the bulk pore solution is difficult to explain the hydration of $C_3S$ with a high *w/b*. Therefore, the attention will be paid to the interfacial nucleation of C-S-H during hydration with normal *w/b*. A novel hypothesis has been proposed to provide a comprehensive understanding of the hydration process from the initial water contact to the end of induction period. The hydration evolution was monitored using an isothermal calorimetry test, while the composition and morphology of hydration products were determined by X-ray diffraction and SEM, respectively. GEMS simulation results provide significant information on the distribution of ion species in the pore solution.

### 3.1.1 Induction period

A significant number of prior investigations have categorized the hydration of $C_3S$ into five distinct stages, as documented in [66]. Scrivener et al. [10] have simplified the classification

into three periods: I - up to the end of the induction period; II - the main hydration peak; and III - after the main peak. The debate continues as to whether the reaction during period I is controlled by the formation of a protective surface layer [67] or solely by the rate of dissolution [12]. The two prevailing theories that attempt to explain the sudden decline in heat release during the induction period are the protective membrane and the dissolution controlled by undersaturation of pore solution. These theories are comprehensively delineated and differentiated in [10]. Nonetheless, the protective membrane hypothesis has faced criticism mainly due to the lack of evidence through microscopic observations.

Figure 3.1 demonstrates that a high water to solid ratio merely results in an increased hydration rate at the main peak, without a significant impact on the duration of the induction period. However, more interesting results are observed in the cumulative heat release. It is observed that the cumulative heat release at the main peak is comparable among samples with a solution to $C_3S$ ratio of 100, 200, and 200 (pH=4), which is approximately half of the heat release at 24 h. This observation indicates that the dissolution degree of the solid is similar at the end of the induction period, even with a very high water to solid ratio. As a result, the calcium concentration in the bulk pore solution is far from saturation with respect to the dissolution of $C_3S$. This conclusion is based on the theoretical calcium concentration from a complete dissolution of $C_3S$.

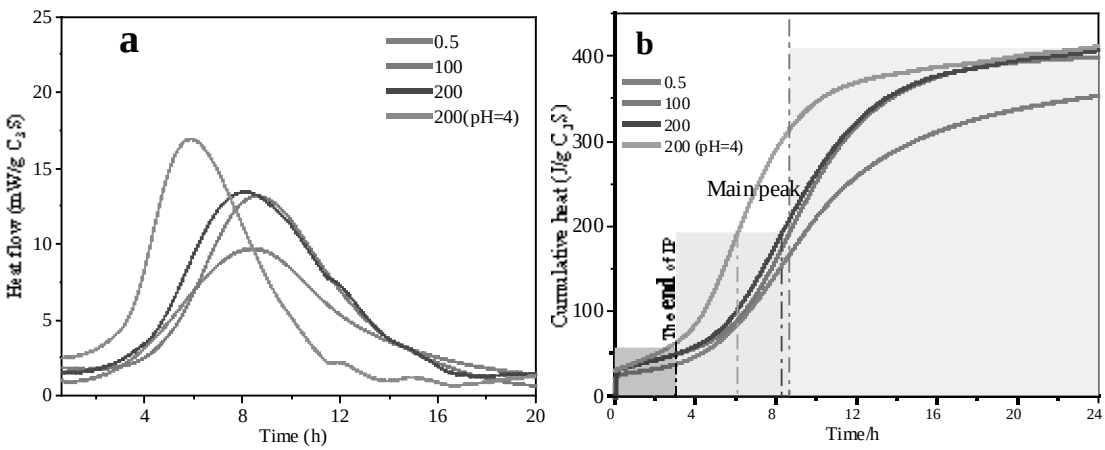


Figure 3.1. Graph "a" presents the hydration heat flow of $C_3S$ with different deionized water to solid ratio (0.5, 100, 200) and sulfuric acid solution (pH=4) to solid ratio of 200. Graph "b" are the cumulative heat these samples, corresponding to *Figure 2* in paper I [68].

$C_3S$ with an empirical formula of $Ca_3SiO_5$ has a molar mass of 228.3 g/mol. To achieve a saturated state (>22.5 mmol/L [69,70]) with respect to portlandite at 25 °C, a water to solid ratio of 100 requires the consumption of more than 1/6 of $C_3S$ (22.5/131.4 from Table 3.1). When the water to solid ratio is increased to 200, more than 1/3 of solid $C_3S$ must be consumed to attain the saturated condition. A complete dissolution of $C_3S$ with a water to solid of 600 only results in calcium concentration of 21.9 mmol/L in pore solution, which is slightly lower than

the saturated concentration of portlandite. Despite this, the precipitation of portlandite is still detected in the product at 4 h [68], which challenges the theory that the dissolution rate is controlled solely by the thermodynamic state of the bulk pore solution, as discussed in [16].

Table 3.1. The theoretical $Ca^{2+}$ concentration from a complete dissolution of $C_3S$ with a high water to solid ratio.

| Water to solid ratio (by weight) | Volume of solvent (ml) | Mole of Ca in solid (mmol) | Complete dissolving Ca concentration (mmol/L) |
|---|---|---|---|
| 100 | 100 | | 131.4 |
| 200 | 200 | 13.14 | 95.7 |
| 600 | 600 | | 21.9 |

Hydration heat flow of $C_3S$ with and without $C_3A$ is shown in Figure 3.2. The presence of $C_3A$ evidently prolongs the starting point of the induction period. The majority of previous studies have proposed that the effect of aluminate on the hydration during the induction period is caused by inhibiting the dissolution of $C_3S$ [71,72]. However, it should be noted that the "induction period" in these studies refers to the time from water addition to the end of the low-rate period. In contrast, this study tries to distinguish the inhibiting effect of aluminates on dissolution and nucleation processes. By replacing the concept of thermodynamic state between the solid and bulk pore solution with the state within the interfacial regions near the surface, we propose that the sharp decrease in heat release is a result of the increase in saturation degree within the near surface with respect to $C_3S$ dissolution.

The occurrence of a delayed starting point, as shown in Figure 3.2b, can be attributed to the inhibiting effect on dissolution by Al species absorbed on the surface of $C_3S$. During this period, the pH value of the pore solution is typically below 12.6. As hydration progresses, the pH increases and the effect of Al on dissolution is eliminated [73,74]. It means that the Al in solution has little influence on the dissolution of $C_3S$ during induction period. This finding is consistent with the result that the lowest point of heat release rate in $C_3S$ with $C_3A$ is even higher than that of pure $C_3S$ during induction period (Figure 3.2a). The ending time of low-rate period is delayed by the presence of aluminate due to the inhibition of both dissolution and precipitation, which is similar to the effect found in [75].

The addition of KOH and $K_2SO_4$ has been found to mitigate the effect of $C_3A$ on the induction period and even shorten its duration. In particular, the heat flow of samples in KOH solution is much higher than the others in this period, indicating a higher dissolution rate of $C_3S$ in KOH solution than in other solutions when the nucleation of the hydration products takes over the hydration process. The presence of $K^+$ ions and high pH in the solution accelerates nucleation, resulting in a reduction in the duration of induction period. $K_2SO_4$ eliminates the effect of Al by reducing the concentration of Al through ettringite precipitation. Although $C_3A$ has little effect on the starting point induction period in $K_2SO_4$ solution, it does reduce its duration, and

as such, further attention should be paid to the nucleation and growth of the hydration products.

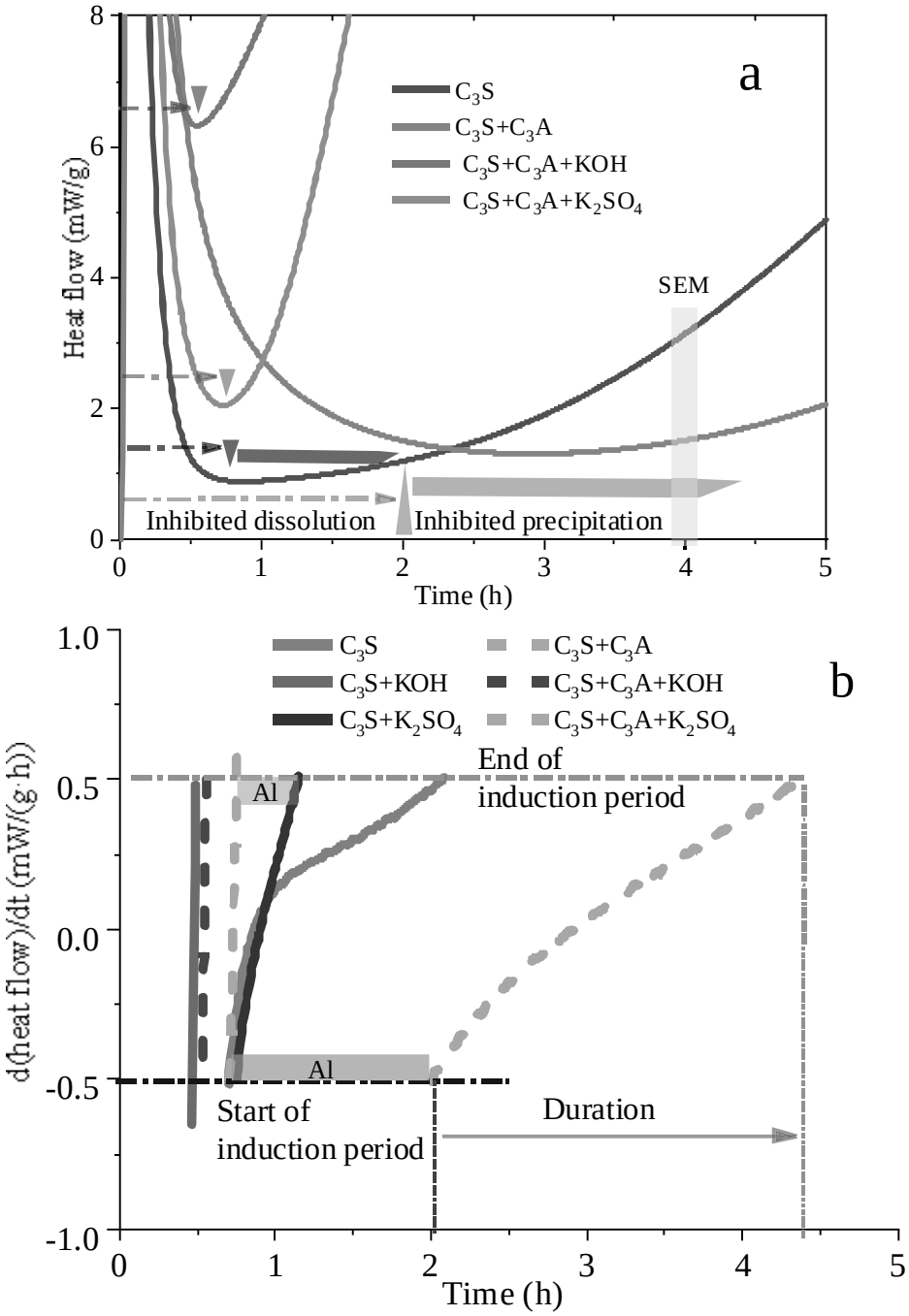


Figure 3.2. Hydration heat flow of $C_3S$ with the presence of $C_3A$ and additives in the first 5 h (a). Induction period of $C_3S$ hydrating in solutions with and without $C_3A$ (b). Samples were mixed with a water to solid ratio of 0.5 and cured at 25 ℃, corresponding to *Figure 7* in paper I.

### 3.1.2 Main peak

Figure 3.3 presents heat release at the main peak from hydration of $C_3S$ in different solutions. After the low-rate period the interaction between water and $C_3S$ will proceed to an acceleration period during which time the growth of hydration products occurs, the heat release of $C_3S$ hydrating in $K_2SO_4$ solution at 20 ℃ overtakes the other two mixes and maintains the

maximum until deceleration period at about 10 h. KOH induces the time of main peak appears much earlier than the others at 25 °C, but the maximum hydration rate is still observed in $K_2SO_4$ solution. This indicates that $K_2SO_4$ has the most enhancement of the growth of hydration products at acceleration period.

In previous studies, two hypotheses, namely the diffusion layer hypothesis and the impingement hypothesis, have been proposed to explain the heat evolution at the main peak. However, these hypotheses were unable to provide a satisfactory explanation for some experimental evidence [10]. In recent years, another two hypotheses, namely the confined growth and dissolution limitation hypotheses, have been introduced and critically evaluated. Moreover, the hypothesis about the C-S-H growth seems to be quantitatively supported through a needle model [76]. However, the underlying mechanism behind the formation of C-S-H needles is still lacking a fundamental explanation.

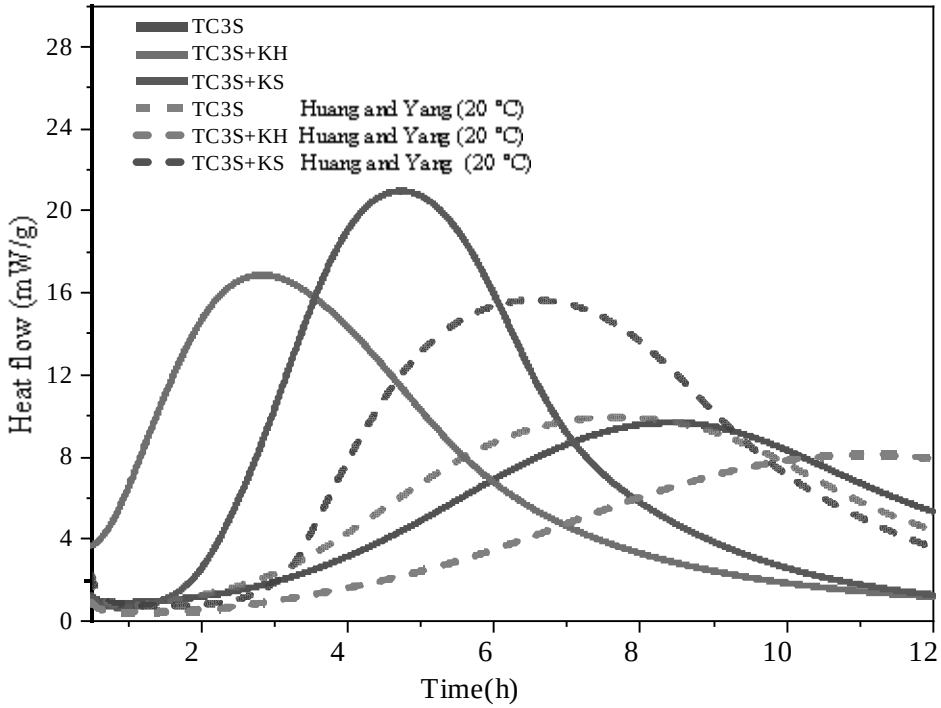


Figure 3.3. Hydration heat flow of $C_3S$ with deionized water, KOH and $K_2SO_4$ from 0.5 to 12 h. The solid line is hydration data with a water to solid ratio of 0.5 at 25 °C from [68], and the dash line is hydration data with a water to solid ratio of 2 at 20 °C.

Results in this study (see Figure 3.4) provide the evidence for the nucleation of a primary mono floc (0), formation of a dimer floc (1), a single strip from the nearly oriented attachment (2) and the clusters from a strip attachment (3) or primary particles attaching to strips. This implies that the precipitation of C-S-H is very similar to the crystallization process of some other polymers or minerals [77,78], which starts from the nucleation of primary mono flocs that are poorly crystalline nanoparticles or colloidal. The mono floc may correspond to the intermediate C-S-H phase during the precipitation process as highlighted in the previous investigations

[79,80]. As it is thermodynamically metastable, it tends to aggregate into strips through oriented attachment within a local region. As the precipitation of mono floc and strips increases, the mono floc will attach to the strip and strips will agglomerate to form more stable clusters or blocks. The primary mono floc seems to be a globular grain with size smaller than ~60 nm. The presence of $C_3A$, KOH and $K_2SO_4$ will alter the size of mono floc as well as the orientation of particle attachment, resulting in a variation in length of strips (needles) and morphology of products.

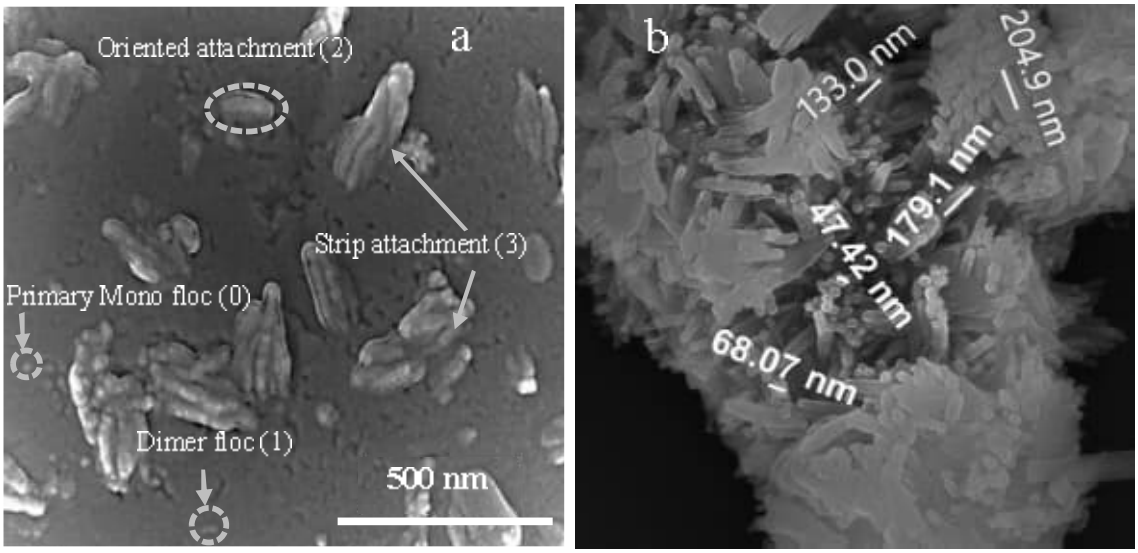


Figure 3.4. SEM images of $C_3S$ hydrated in deionized water at 25 °C. The hydration was stopped at 4 h after water addition by freeze-drying. An image with higher magnification was provided to give a clear picture of the particles on the surface (a) [68]. Nucleation of primary mono-flocs and dimer flocs was detected above or near the etch pit. C-S-H grows by nearly oriented attachment and block attachment. Hydration products of $C_3S$ with $K_2SO_4$ solution at 20 °C stopped at 4.5 h by solvent exchange (b) [22].

### 3.1.3 Hydration mechanism up to the main peak

The reaction of $C_3S$ in water can mainly classified into five stages. Stage I is a fast dissolution in the first few minutes right after contacting with water. Stage II is the state for approaching dissolution equilibrium with respect to $C_3S$ within the local zone near the surface. In stage III a new surface equilibrium with respect to nucleation of hydration products would be established. Afterwards it goes into stage IV with the surface nucleation, and Stage V will follow when the precipitation of hydration products takes over by attachment to growth.

Stage I and II corresponds to the first dissolution peak in the hydration heat flow, which is controlled by the dissolution rate of minerals (0' process illustrated in Figure 3.5). After these two stages, the rate of reaction is limited by the nucleation and growth rate of the main products C-S-H. Nucleation of C-S-H is a colloidal assembly process similarly found in the crystallization of many other minerals [77,78]. The kinetics of this process is a key to understand the hydration mechanism in the main peak of hydration. The pH value is a critical

parameter to control the nucleation (0 process) and dimer assembly (1 process), since it determines the calcium and silicate ion species in pore solution (see the results from GEMS modellings in [68]). Al ions have an inhibiting effect on the dissolution to affect the process 0` and change the kinetic of nucleation of C-S-H. Presence of other inorganic ions such as $K^+$, $SO_4^{2-}$ will alter the attaching process (2 to 3) as well.

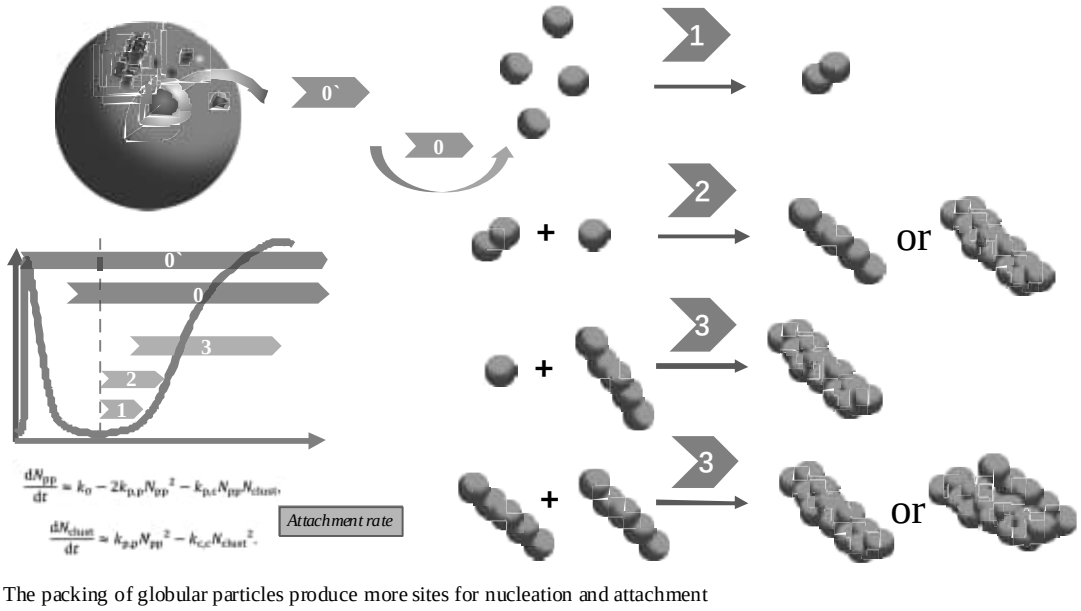


Figure 3.5. Illustration of hydration process up to the main peak time from the nucleation perspective.

The presence of some organic substances has been observed to increase the solubility of C-S-H [81], as indicated by an increase in calcium concentration. This effect brings the solubility of C-S-H closer to, and sometimes even higher than, the equilibrium line of $C_3S$ hydration. The interaction between organic admixtures and Si ions results in the release of more ions into the bulk solution from the near surface region, leading to a higher silicate ion concentration in the solution than in the pure system. This modification of the double layer reduces the concentration of Si and Ca in the near surface region, which in turn requires a higher supersaturation state for the precipitation of primary C-S-H on the surface with these admixtures. Furthermore, some organics such as PCE can stabilize the primary floc [82], hindering the attachment between primary particles.

## 3.2 Hydration of cement blended with SCMs

A device for instantaneous monitoring of electrical conductivity was designed, with a focus on understanding the relationship between the conduction and structure of paste. This section presents the correlation between the electrical properties, hydration process and structure evolution in the hydrating Portland cement and the blended pastes. The evaporable water content in paste was measured by a newly designed procedure, so that it enables the calculation

of the electrical conductivity of the pore solution based on the chemical composition of the binders and the volume of evaporable water. The formation factor was calculated to distinguish the effect of pore solution and structure on conduction. The change of liquid connection has been evaluated during the hydration. The average growth rate of the formation factor is defined to indicate the setting and hydration reactivity of cementitious materials.

### 3.2.1 Hydration induced conduction change

The process of cement hydration can be divided into two simplified stages: the dissolution of solid minerals in water, which increases the ion concentration in the liquid pore solution; the precipitation of hydration products to create solid network. Figure 3.6 depicts change of conduction in paste during the hydration, which is mainly caused by the changes in volume of solid particles and liquid pore solution. The electrical conductivity of solid particles is approximately $1 \times 10^{-8}$ mS/cm. This value is much lower than the typical ionic conductivity of pore solution, $\sigma_s = 10–200$ mS/cm [83]. Thus, the dry solid component can be considered as an insulative element ($\sigma s \rightarrow 0$).

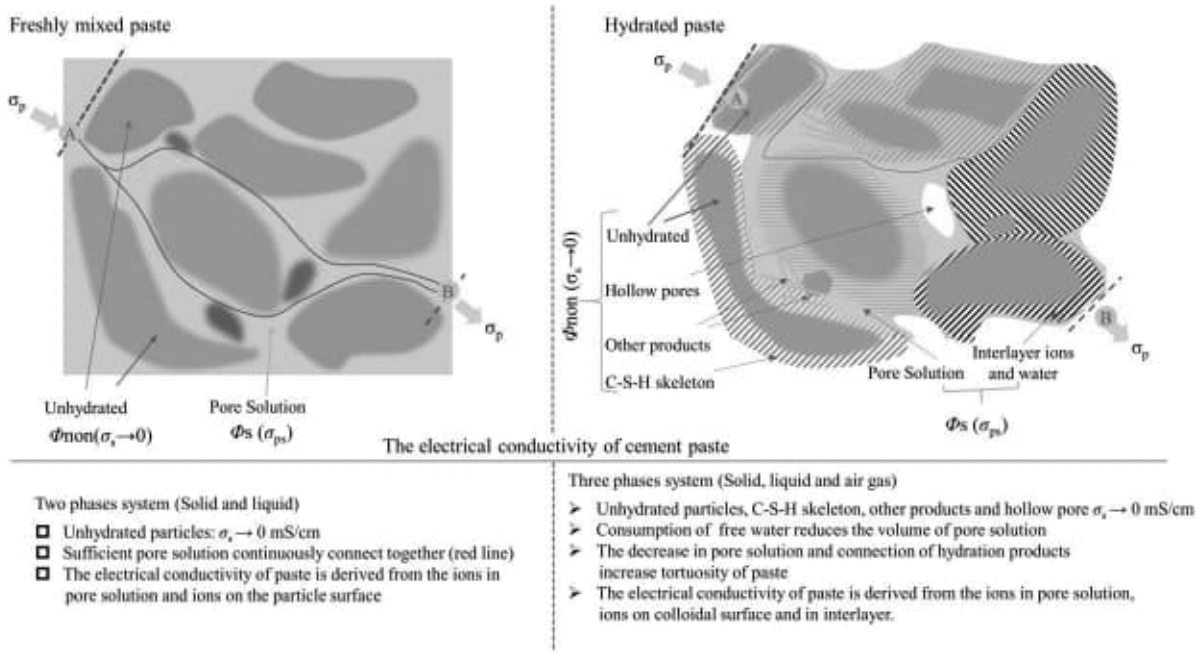


Figure 3.6. A graphical representation of the temporal evolution of electrical conductivity during the hydration process.

### 3.2.2 Conductivity of pore solution over time

The pore solution is the primary conductive component in the paste, and the ionic conductivity of the solution depends on the type and concentration of ions. The concentration of highly soluble alkalis can be determined by using the evaporable water content and chemical composition of binders (see Table 2.1). The electrolyte conductivity of the pore solution can be represented as the sum of the molar conductivity of each ion species [84]. The detailed

procedure and equations for calculation of ionic conductivity of pore solution have been elaborated in paper II [59], assuming that alkali metal oxide has a fast dissolution to a certain percentage in the first few minutes.

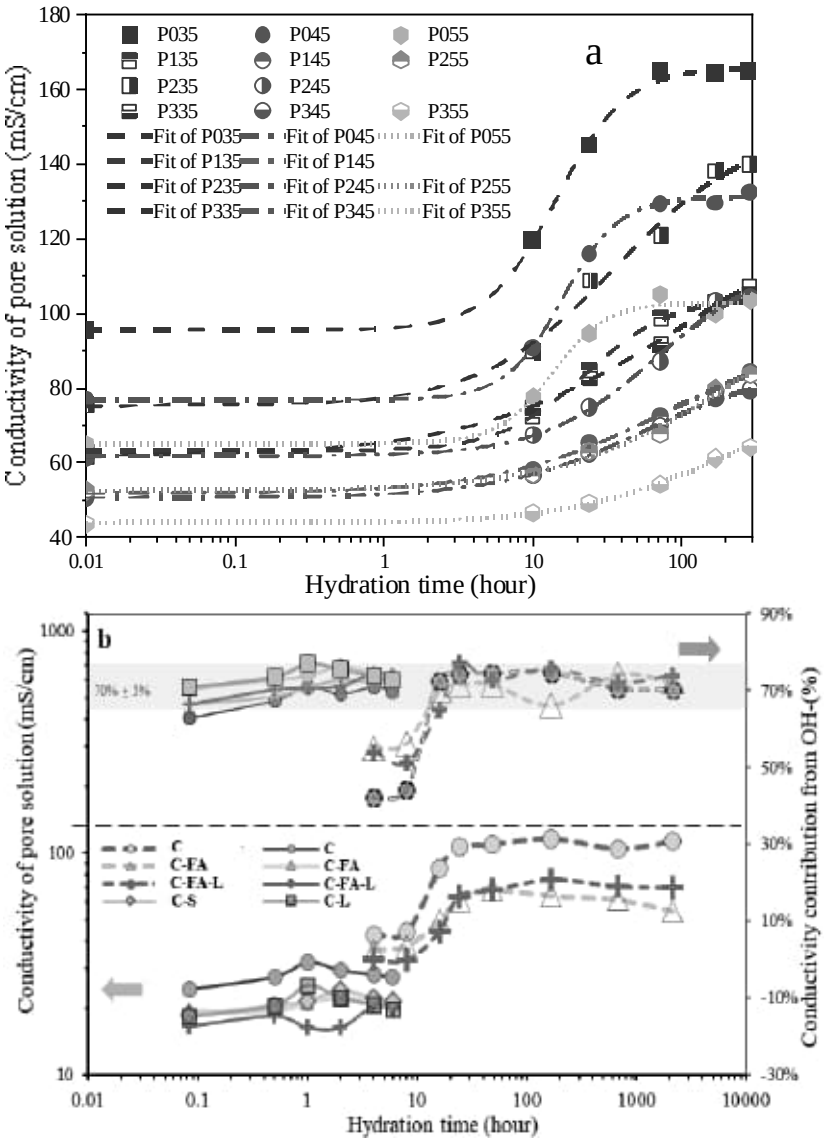


Figure 3.7. Calculated conductivity of pore solution. (a)- the values in this study. (b)- the conductivity value calculated based on the concentration of squeezed pore solution from literatures: solid line from [17] with *w/b*=0.75, and dash line from [85] with *w/b*=0.5. Notes, C: Portland cement; FA: fly ash; S: slag; L: limestone, corresponding to *Figure 7* in paper II.

Figure 3.7a illustrates the calculated conductivity of pore solution in paste samples along with the regression lines. It shows that an increase in *w/b* results in a decrease in electrical conductivity of the pore solution as a higher *w/b* lowers the concentration of alkali ions by introducing more evaporable water into the paste. Blending SCMs reduces the electrical conductivity of pore solution, which is consistent with data from published papers based on the squeezed pore solution data (see Figure 3.7b). It was also discovered in the previous investigation [68] that blending SCMs reduces the electrical conductivity of pore solution.

Even though the fly ash used in [67] has high alkali content (3.9 % $K_2O$ and 0.9 % $Na_2O$), the concentrations of $K^+$, $Na^+$, and hydroxide in the fly ash blended pastes are similar with those in pastes with identical quartz replacement, supporting the assumption that alkalis in fly ash have a very low solubility.

The measured conductivity of paste is lower than the calculated conductivity of pore solution because the presence of cement particles breaks the connection between pore solution. The chemical composition of Portland cement used in this study is highly similar to that of cement used in [85], so the calculated conductivity of P055 (light blue hexagon in Figure 3.7a) based on chemical composition is close to that of ordinary Portland cement with *w/b* of 0.5 based on the data of squeezed pore solution (dashed line sphere in Figure 3.7b). Hydroxide ion is the major conductive ions in the pore solution of cement-based materials which accounts for around 70 % of the electrical conductivity (see Figure 3.7b). The electrical conductivity of pore solution remains almost constant until it has a sharp increase after about 6 h. The evolution of conductivity of pore solution is well regressed by the Hill function [59]. The fitted lines exhibit the same trend as the evolution of the value calculated from the squeezed pore solution. This verifies that method in this study can effectively quantify the specific conductivity of pore solution without the need to extract the solution from the paste or use any expensive equipment, as summarised in [86], to measure the ion concentration of squeezed pore solution.

### 3.2.3 Evolution of microstructure

To differentiate the impact of pore solution and microstructure, the formation factor (*F*) was introduced. It was originally proposed by Archie [87] to describe the relationship between the electrical conductivity of sandstone and its permeability or porosity. *F* is now commonly used in cement-based materials to indicate the diffusivity of ions in hcp, which shares a porous nature with sandstone, according to the definitions in [88,89].

$$F = \sigma_{ps}(t)/\sigma_p(t) \tag{3.1}$$

where $\sigma_p(t)$ represents the conductivity of the bulk paste, while $\sigma_{ps}(t)$ indicates the conductivity of pore solution at a given hydration time, *t*. In this study, $\sigma_p(t)$ is equivalent to the conductivity of naturally saturated hcp. $\sigma_p(t)$ was measured by the designed device, and data of $\sigma_{ps}(t)$ was generated from the regression line in Figure 3.7.

*F* of the porous matrix is determined by porosity and pore connectivity, which can be described by the equation [88,90]:

$$F = \frac{1}{\phi\beta} \tag{3.2}$$

where $\phi$ is the porosity of paste and $\beta$ is the pore connectivity index. In this study, the water

accessible porosity was used to calculate the pore connectivity index.

Figure 3.8 shows the evolution of formation factor in pastes with various binders up to 180 d. Initially, *F* remains constant for a period of 2 to 9 h, which varies depending on the *w/b* and types of SCMs. The initial *F* is higher than 1, and it decreases with increasing *w/b*. It is followed by a sharp increase after the constant period, whose phenomenon is similar to the percolation of solid at the setting time found in ultrasound tests [91]. The effect of *w/b* on *F* is magnified during the fast growth period, The ratio of F in hcp, with a *w/b* ratio of 0.35, to that in hcp with a *w/b* ratio of 0.45 was found to be 1.90, 2.57, 3.90, and 2.05 for CEM I, fly ash, slag, and ternary systems, respectively. The differences in *F* of binary and ternary slag pastes become negligible after 28 d. The fly ash blended pastes exhibit the highest increase in *F* up to 180 d. Figure 3.8 b shows that as the hydration process continues, the $\beta$ value decreases significantly from the point of water addition until 24 h. Despite the slag blended systems having a higher volume of evaporable water than CEM I pastes with identical *w/b*, the $\beta$ value of slag blended pastes is lower than CEM I, as demonstrated by the data for P235 and P335 in Figure 5 of paper II [59]. This difference results in a higher *F* value for the slag blended paste. Therefore, the dissimilarities in *F* values among various binder systems primarily stem from variations in $\beta$.

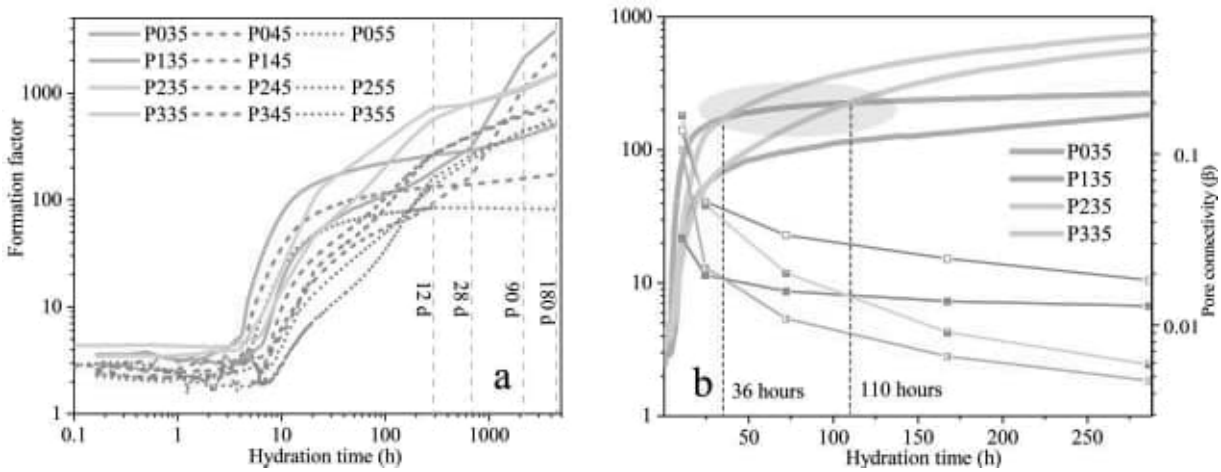


Figure 3.8. Evolution of formation factor for all pastes (a) and pore solution connectivity of binders with *w/b* of 0.35 over time, adopting from *Figure 8* in paper II.

For analyzing the change rate of microstructure, the average growth rate of *F* ($\alpha$-*F*) is defined as Eq. (3.3): where $F(t)$ is the *F* of paste at hydration time *t*.

$$\alpha\text{-}F = \frac{F(t)}{t} \tag{3.3}$$

As shown in Figure 3.9, the progression of $\alpha$-*F* for CEM I paste can also be classified into three phases. The $\alpha$-*F* in Period I has a sharp decrease followed by a constant period. It involves mineral dissolution, ettringite precipitation, and C-S-H nucleation. The $\alpha$-*F* in Period II exhibits a sharp increase because a rapid growth of ettringite, C-S-H, and portlandite joints particles to block the connectivity of pore solution. In Period III $\alpha$-*F* displays a decreasing trend due to the

slowing down of hydration and water consumption. For blended paste, period IV corresponds to a new peak during deceleration, indicating a refining of the pore size due to the later age hydration of SCMs. These periods correlate to the changes of connectivity and size of pores in the pastes during hydration.

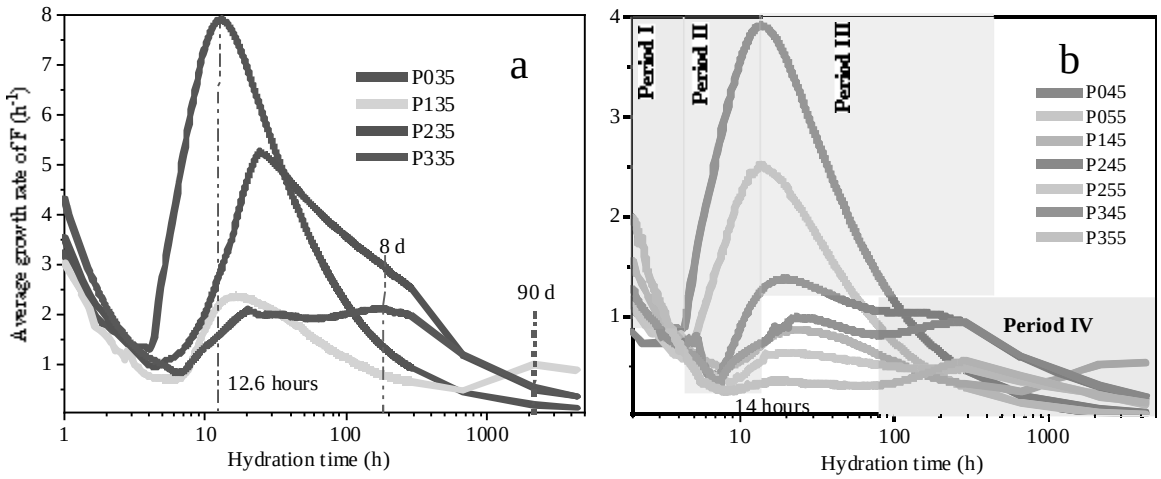


Figure 3.9. Evolution of *a-F* over hydration time, adopting from *Figure 9* in paper II.

### 3.2.4 Moisture content and formation factor

The electrical conductivity of cement-based materials depends on the composition of the paste, which consists of insulative dry solid and conductive liquid solutions (Figure 3.6). After an extension of the percolation theory to the continuum cases [92,93], a general formula similar to Archie's law describes the conductivity of cement-based materials.

$$\sigma_p = a * \sigma_{ps} * (\phi - \phi_c)^m \tag{3.4}$$

After the substitution of conductivity with $F$, we get:

$$F = 1/a * (\phi - \phi_c)^{-m} \tag{3.5}$$

In this study, the conductive component is assumed to comprise ions in pore water and layer water, with $\phi$ representing the volume of evaporable water. $\phi_c$ is the critical volume required for percolation of the conductive component, while $m$ and $a$ represent the shape factor and the constant, respectively. Figure 3.10 and $R^2$ in *Table 6* of paper II [59] indicate that the regression curve matches the experimental data well.

The shape factor and percolation threshold are affected by the type of binders. Systems with complex shapes, such as sand and chalk, have a higher shape factor (1.6) compared to single-shaped particle systems. Calcium montmorillonite has the highest shape factor of 3.28 [94]. The difference in the threshold for percolation may improve the understanding and modelling

of mass transport in concrete containing SCMs by some lattice models.

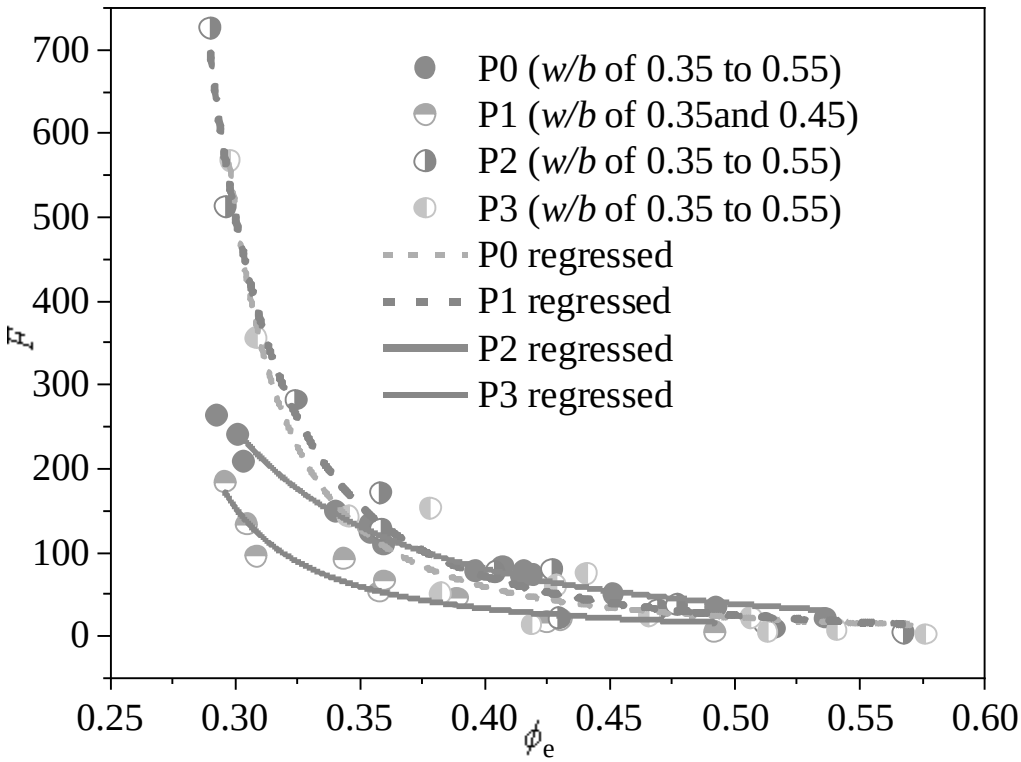


Figure 3.10. Relationships between the volume of evaporable water ($\phi_e$) and formation factor ($F$). P0, P1, P2 and P3 correspond to CEM I, the fly ash, slag, and ternary blended pastes, respectively: adopting from *Figure 13* in paper II.

## 3.3 Chapter summary

The mechanism of cementitious materials reacting with water at the early age is a complicated scientific problem. Reaction of the main mineral, $C_3S$, has not been thoroughly understood to date. Experimental studies have shown that the dissolution theory can hardly explain the anomalous interaction at high water to solid ratio. Therefore, a theory based on the crystallization and precipitation process of the main hydration products has been proposed. The hypothesis suggests that C-S-H primarily nucleates within the near-surface region, bridging the gap between dissolution and protective layer theories. The precipitation of C-S-H is a nonclassical nucleation process involving primary particle nucleation and growth by particle attachment. The acceleration of C-S-H growth rather than etch pit dissolution may explain the rapid reaction rate increase after the induction period. The dissolution of $C_3S$ and precipitation of C-S-H are affected by potassium salts and pH levels.

The interaction of water with supplementary cementitious materials is a more complex process than that with $C_3S$. Therefore, a more comprehensive detection method based on conductivity was used to monitor the interaction process at early age. Electrical conductivity evolution in

hydrating pastes relates closely to chemical reaction processes and can be classified into four stages during early hydration. Differences in the connectivity of pore solution primarily account for the variations in the *F* of pastes with different binders. The *w/b* ratio impacts the electrical conductivity and *F* of pastes by altering the alkali concentration in pore solution and increasing pore connectivity. The growth rate of the formation factor can indicate the reactivity of different binders. Blending SCMs refines the pore structure, decreasing pore connectivity. Monitoring conductivity can demonstrate the relation between evaporable water volume and formation factor, facilitating in-situ monitoring of moisture, alkali ion concentration, and pore connectivity.

# 4 Interaction of water with hardened cement-based materials

*The hardened cement-based paste is a complex porous matrix with a wide range of pore sizes from 0.5 nm to tens of micrometers. Due to the hydrophilic nature of cementitious materials, the surface of the pore wall interacts strongly with water. Understanding the interaction between the pore structure and water is essential to develop effective strategies for improving the durability of cement-based materials. The effect of SCMs on water-related relaxation processes in hcp with different RH levels has been quantitatively illustrated for the first time in cement-based materials research. This chapter comprises the content of paper III and IV.*

## 4.1 Desorption isotherms

Water vapour isotherm is very useful for understanding the moisture-related behavior of cement-based materials and its relationship with pore structure. It has been utilized for modelling moisture transport, understanding drying shrinkage mechanisms [95,96], and exploring microstructural changes during the drying process [97]. This section presents the effect of SCMs on nanopores in hardened pastes, which was investigated by dynamic water vapour desorption. C-S-H content was determined from sorption data, and portlandite content was determined by thermogravimetric analysis. The hydration degree of SCMs was evaluated by the means of GEMS simulation.

### 4.1.1 Effect of SCMs and *w/b* on isotherms

Figure 4.1 shows that the type of SCMs and *w/b* make impact on the desorption isotherms. While paste mixing with *w/b* of 0.35, the replacement with SCMs increases the moisture content ($W_e$) in the hcps under the whole range RH intervals from 11 % to ~95 %. Moreover, the effect of SCMs on desorption isotherms is dependent on the *w/b* of the pastes. An increase in *w/b* causes an increase in moisture content of CEM I pastes at all RH conditions. However, the increase in moisture content of the blended pastes mainly occurs at RH above 40 % as the *w/b* increases to be larger than 0.45 [44]. A similar phenomenon has been reported by Olsson

et al. [39] in desorption data of the well hydrated (water curing for 4 years) pastes blended with slag. Effects of SCMs introduce additional complexities to the prediction of moisture state and transport in concretes containing SCMs.

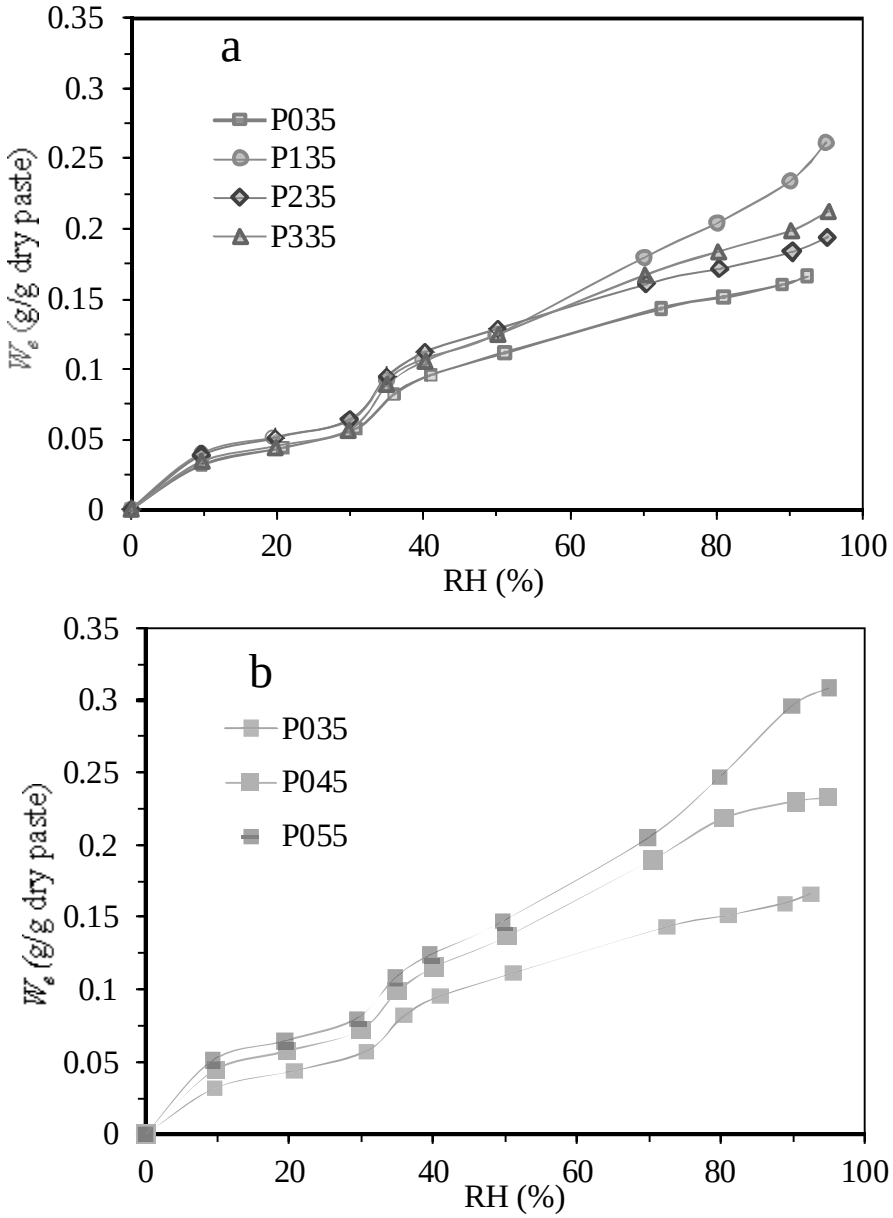


Figure 4.1. Water vapour desorption isotherms of pastes measured at 20 °C. Plots in a are comparisons between different binder systems with the same *w/b*, exampling with *w/b* of 0.35. Plots in b are comparison between different *w/b* for CEM I paste, refer to [44] for more detailed data.

### 4.1.2 Calculating the pore size distribution

The BJH method has been widely used to estimate the pore size distribution (PSD) in cementitious materials using data from water vapour desorption [96,98,99], which was initially proposed by Barrett, Joyner, and Halenda [100] for determining the pore size distribution in porous materials based on $N_2$ sorption isotherm. Although the pore geometry in hcps is more intricate than the assumed cylindrical shape in this approach, and cavitation occurs during the

desorption process [101,102], the computed results can provide valuable insights for comparative analysis, such as the present study. To calculate the pore size distribution, a physically adsorbed layer of molecules on pore surfaces needs to be considered. The radius of an open cylinder pore ($r_p$) is determined by adding the thickness $t_h$ to Kelvin diameter $r_k$ ($r_p = r_k + t_h$). The correlation between the statistical thickness of the water film and RH in hcp was initially discovered by Hagymassy et al. [103]. Badmann [104] developed this to describe the correlation using two parameters, $K_1$ and $K_2$. Parameters for pastes in this study were determined by a trial-error method to adjust the constants for different binder systems to ensure a good match between the measured and calculated total pore volume.

This method uses the Kelvin equation to establish a relationship between the radius of the condensed liquid in cylindrical pores and the relative humidity (represented by $RH_k$). However, ions in a solution can affect the equilibrium vapour pressure on the plane surface ($p_s$), which is different from the pressure on the pure water surface ($p_0$). Raoult's law [105,106] provides an empirical expression of the correlation between the ion concentration and the RH on the plane surface ($RH_s$), as shown in Eq. (4.1). The total moles of ions in the solution are represented by "$n_i$", and "$n_w$" refers to the moles of water in the solution. Consequently, the observed relative humidity value ($RH_o$) is a result of both curvature and ion effects, which can be described by Eq. (4.2).

$$RH_s = \frac{p_s}{p_0} = \frac{n_w}{n_w + n_i} \tag{4.1}$$

$$RH_o = RH_k RH_s \tag{4.2}$$

The influence of ions on the $RH_s$ of the pore solution has not been considered in previous studies [96,98,99], where the observed $RH_o$ was used as $RH_k$. Figure 4.2 presents a comparison of the calculated PSD with the $RH_s$ of the pore solution and pure water. Although the ions in the pore solution have a minor influence on the calculated width and volume of pores with a diameter less than 10 nm, neglecting the ion effects results in a significant underestimation of the size and volume of capillary pores (width greater than 12 nm). Therefore, it is crucial to include the influence of ions on the surface pressure of the pore solution when determining the PSD using the BJH method on water vapour desorption isotherm.

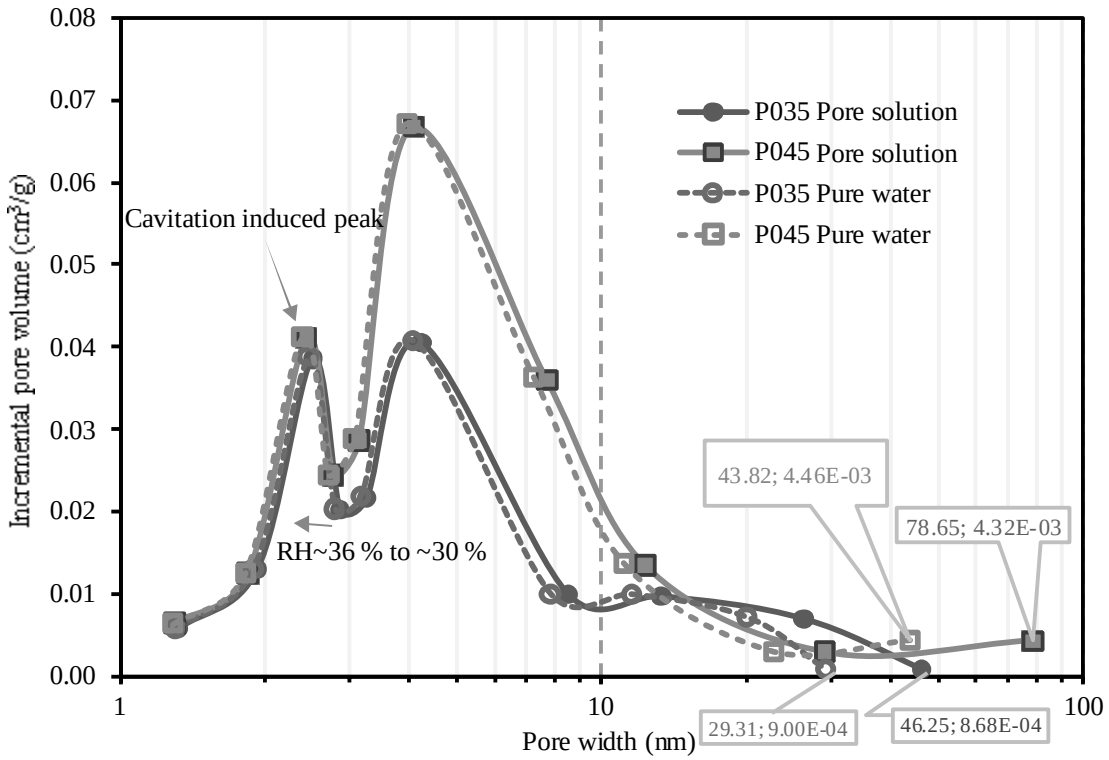


Figure 4.2. The effect of ions in pore solution on the calculated PSD of hcps, exemplifying with CEM I pastes, corresponding to *Figure 4* in paper III.

Figure 4.3 illustrates the pore size distribution obtained using the BJH method to analyze the water vapour isotherm data. The pore widths, calculated as the diameter of open cylinder pores, are between 1–90 nm. It means that water vapour desorption analysis can provide effective indication of mesoscale pore structure in hcp. It should be noted that a sudden decrease in the moisture content drying from 36 % to 30 % RH can be attributed to cavitation occurring in larger pores [101,102]. It is not useful to designate the calculated volume at this interval to pores of a specific size. However, it is noteworthy for comparative purposes in evaluating the volume of ink-bottle gel pores in various binder systems. Incorporation of SCMs leads to a minor reduction in the volume of interlayer space in hcp. The use of both slag and fly ash results in an increase in the value of cavitation-induced peaks, indicating a refinement of the large gel pores and the reduced pore connectivity. At higher *w/b*, the refinement effect of slag and fly ash is more pronounced, leading to a larger difference between binary and CEM I hcp. The blending of slag and fly ash significantly increases the volume of open large gel pores (3.3–12.3 nm), with the most significant effect observed for hcp with a *w/b* of 0.35.

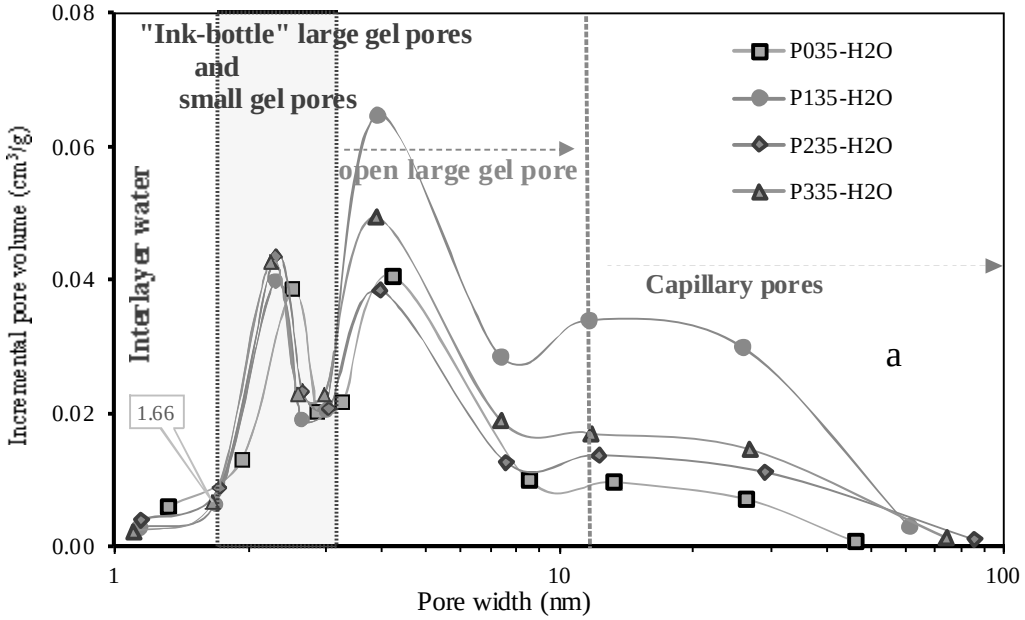


Figure 4.3. The PSD in hcp calculated by BJH method from water vapour desorption, exampling with pastes with *w/b* of 0.35, refer to [44] (paper III) for the detailed information of all pastes.

### 4.1.3 Evaluation of hydration degree

Moisture content at 20–25 % RH is associated with water in the interlayer space of C-S-H. Bonnaud et al. [107] conducted molecular dynamic simulations and discovered that interlayer water began to dry at approximately 20 % RH. The mesoporous structure of C-S-H gives it a specific surface area at least one order of magnitude greater than other hydration products. When the RH falls below the condensation point in the gel pores, most of the moisture in hcp is adsorbed in the interlayer space of C-S-H. Using the common atomic structure of $1.65CaO{\cdot}SiO_2{\cdot}1.75H_2O$ from [108] or $1.69CaO{\cdot}SiO_2{\cdot}1.80H_2O$ from [109], the evaporable water (dried at ~0 % RH) in the C-S-H structure is roughly $7.3 \times 10^{-3}$ mol/g (or 0.131 g/g) dried C-S-H, with approximately 0.55 mole of chemically bound water attached to Ca or Si atoms [110]. This value is close to the experimental result (0.1 g/g) in [111] and very similar to the value used in [96,99] for calculating the C-S-H content. Assuming SCMs have few effects on the evaporable water in the interlayer of C-S-H, Eq. (4.3) can be used to estimate the C-S-H content in all hcps in this study.

$$W_{CSH} = \frac{n_{e,20}}{\bar{n}_{w,CSH}} \tag{4.3}$$

where $n_{e,20}$ (mol/g) is the amount of water adsorbed in hcp at 20 % RH (partially shown in Figure. 4.1), $\bar{n}_{w,CSH}$ is the amount of evaporable water in C-S-H with respect to the weight dried at ~0 % RH ($7.3 \times 10^{-3}$ mol/g), and $W_{CSH}$ is the weight of C-S-H in the dried hcp. The

amount of C-S-H in pastes have been calculated and presented in paper III [44].

Thermodynamic modelling has been popularly employed to investigate the influence of SCMs on the hydration process and phase assemblage in cementitious materials. It was also used in this section to evaluate the effect of SCMs hydration degree on the phase assemblage in hcp. Figure 4.4 shows the hydration phases in the hcp with different hydration degree of fly ash. The hydration degree of CEM I is set to 92.2 %, which is calculated by dividing the measured content of portlandite in P055 (22.0 % by thermogravimetric analysis) with the portlandite content in the fully hydrated paste (23.87 % by GEMS). The focus centers on the quantities of the two main hydration products, namely C-S-H and portlandite. In the case of the fly ash binary hcp, portlandite will decrease due to consumption by the pozzolanic reaction of fly ash. Moreover, the amount of C-S-H will increase with the hydration degree, during the process before a complete consumption of fly ash. Theoretically, a hydration degree of 38 % will consume all portlandite in P145. Beyond this hydration degree, the content of C-S-H will decrease due to the formation of strätlingite.

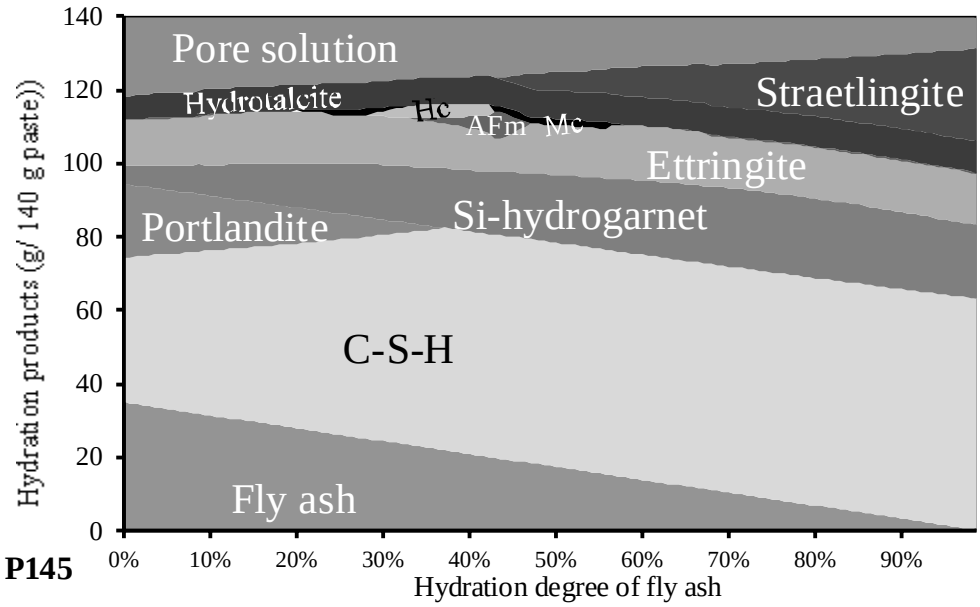


Figure 4.4. Phase assemblage of hydration products with the increase in hydration degree of fly ash, refer to paper III [44] for data of other binder systems.

To validate the method using water vapour sorption data to calculate the hydration degree of SCMs, the amount of portlandite was measured through thermogravimetric analysis. The hydration degree of SCMs is evaluated by its linear correlation to the amount of C-S-H and portlandite [44]. Figure 4.5 illustrates the hydration degree of fly ash and slag based on the measured portlandite content and the calculated C-S-H content. The good agreement between

the hydration degree estimated by these two methods confirms the reliability of water vapor desorption for assessing the C-S-H content and hydration degree. An increase in *w/b* will enhance the hydration of fly ash and slag. The calculated hydration degree of fly ash falls within the range of 20 %–30 %, which is consistent with previously reported data for hcps blended with 35 % fly ash under similar curing conditions [112,113]. The calculated hydration degree of slag in binary and ternary hcps ranges from 40 % to 52 % and 43 % to 59 %, respectively. These values are similar with the measured degree of hydration for slag blended hcps with a *w/b* of 0.42, as reported in previous studies [114].

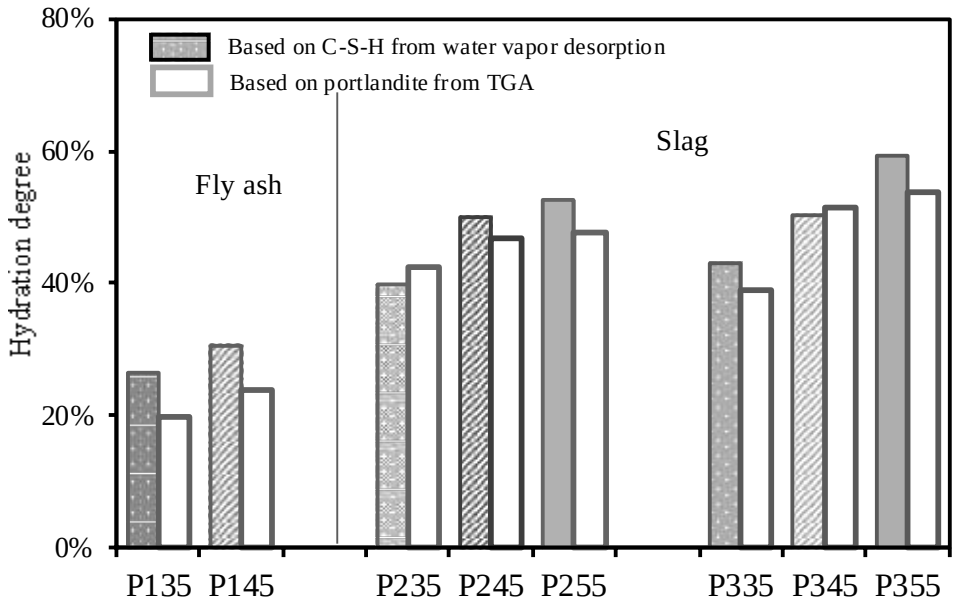


Figure 4.5. Hydration degree of fly ash and slag in the blended hcp after a 6-month water curing calculated by use of GEMS and water vapor isotherm data, corresponding to *Figure 10* in paper III.

## 4.2 Water behavior in hcp at low temperature

The nanosized confinement of water in hcp will change the thermodynamics of liquid-phase transformations during the freezing and melting experience. This kind of confinement will also change the dielectric response and dynamics of water. In this section low-temperature differential scanning calorimetry (LT-DSC) was employed to quantify the distribution of water confined in different pores during drying under various RH levels. It sheds light on the water distribution in gel and capillary pores with respect to freezable and unfrozen (supercooled) water. Broadband dielectric spectroscopy was used to investigate the dynamics of water confined in the hcp. Various relaxation processes were observed, corresponding to the local chemical environment of C-S-H microstructure, which contributes to a comprehensive understanding of the C-S-H structure.

### 4.2.1 Freezing and melting

Figure 4.6a presents a typical freezing and melting curve of hcp equilibrium under 97 % RH with CEM I paste as an example. The freezing-melting curve exhibits a significant hysteresis, with the average melting temperature being higher than the average freezing temperature. It is a common phenomenon observed in many porous media [115]. This can partially be attributed to the geometrical hindrance effect caused by the pore shape. Furthermore, the attractive potential from the pore wall induces a compression effect, resulting in a non-monotonic correlation between the freezing temperature and pore diameter due to the competition between hindrance and compression [116]. In cases of extreme confinement, water molecules are inhibited from forming an ice structure to avoid crystallization [50].

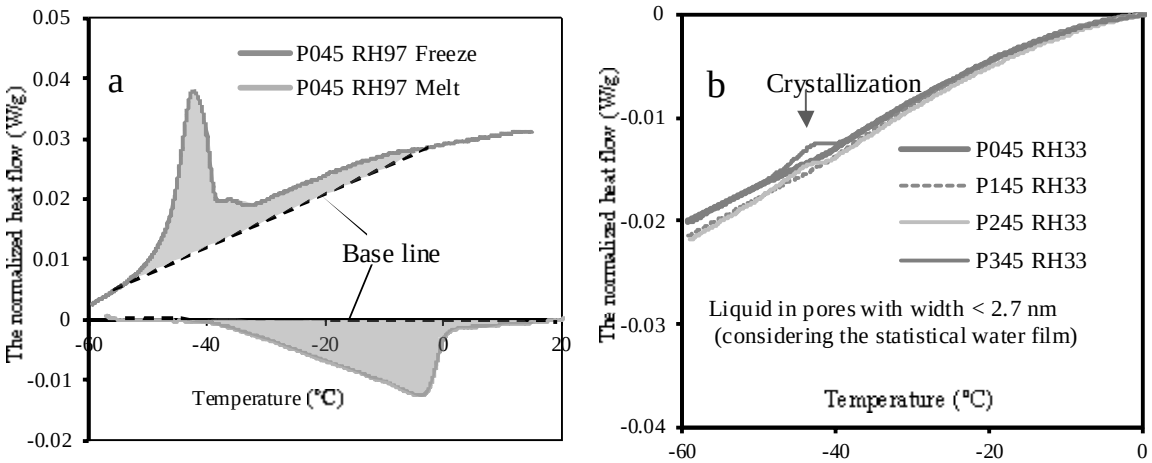


Figure 4.6. Example of low temperature DSC curve for hcp, with OPC paste conditioned under RH of 97 % (a) and pastes conditioned under RH of 33 % (b): corresponding to *Figure 1* in paper IV.

Sun and Scherer [117] suggested that water in pores with a width smaller than 4.5 nm did not undergo ice formation during the cooling process. In addition, Bager and Sellevold [118] observed no ice formation in hardened cement paste with equilibrium at 33 % and 11 % RH. White cement paste at 33 % RH also did not exhibit any exothermic peak indicative of ice formation [119]. However, as shown in Figure 4.6b, crystallization of ice was detected in slag blended pastes (P245 and P345) at 33 % RH, while no ice was found in P045 and P145. This intriguing observation may be attributed to the refined small neck of ink-bottle pores. During the drying process, it may be difficult to dry the inner part of these pores. The expulsion of water from interlayer or small gel pores to larger pores during the cooling process, similar to the freezing process of montmorillonite [120], may also result in this phenomenon.

### 4.2.2 Thermoporometry to determine moisture distribution

Based on the thermodynamic characteristics of water-ice phase transition in porous matrix, the correlation between phase change temperature and pore size can be expressed by the Gibbs-

Thomson equation [117,121].

$$r_p = \frac{A}{\Delta T_s} + \delta \quad \text{.....} (4.4)$$

In this equation, the radius of the cylinder pore is denoted as $r_p$ (nm), and the undercooling is represented by $\Delta T_s$ (°C), which is positive when the temperature is below the melting point of the bulk ice crystal. The constant $A$ is determined by the surface energy between water and the cement-based material, whilst the constant $\delta$ is related to the layer of unfrozen water and the shape of the pore. The shape of the pore is typically assumed to be cylindrical, and for the freezing process, the values of $A$ and $\delta$ are taken as 64.67 nm and 0.57 nm, respectively. For the melting process, the values are 32.33 nm and 0.69 nm, respectively [117].

Taking into account the baseline for LT-DSC and the variation in heat capacity of the different phases (liquid, ice crystal, and porous body), the quantity of ice formed at temperature $T$ can be computed using Equation (4.5) due to the narrow temperature intervals in the data collection [117].

$$m_c(T + n\Delta T) = m_c(T) + \sum_1^n \frac{\Delta T}{2}\left[\frac{Q(T+n\Delta T-\Delta T)-Q_0}{q h_f} + \frac{Q(T+n\Delta T)-Q_0}{q h_f}\right]\exp\left[\frac{\Delta T(C_{pC}-C_{pL})}{h_f}\right] \quad \text{.....} (4.5)$$

where $m_c(T)$ represents the ice mass at temperature $T$, and $\Delta T$ denotes the temperature interval that was set to 0.02 °C in this study. $h_f$ (J/g) denotes the heat of fusion for pore water, $Q(T)$ (W/g) represents the heat flow into the sample, $Q_0$ (W/g) is the baseline in heat flow, $q$ (°C/s) is the heating rate, $C_{pL}$ (J/g/°C) denotes the heat capacity of the pore liquid, and $C_{pC}$ (J/g/) represents the heat capacity of the ice crystal. The baseline of LT-DSC is estimated by fitting a linear line from the onset of freezing to approximately -55 °C.

Figure 4.7 presents the distribution of ice volume in cement paste under various RH levels. The curves for hcp equilibrium with 33 % RH are not included due to limited crystallization. As expected, the ice volume in hcp decreases as the RH decreases. The hysteresis phenomenon during freezing and melting processes is observed under all RH levels. When the temperature is converted to pore width using Eq. (4.4), the hysteresis effect becomes more noticeable, particularly in terms of the minimum pore width required for ice crystal formation. The freezing curves suggest that the critical pore width for ice formation is around 4 nm, implying that no ice will form in pores smaller than this value. However, previous studies have detected crystallization peaks in silica nanopores with diameters as small as 3 nm [122], and molecular dynamic modeling has indicated a critical nucleation radii of 1 nm [123]. The critical pore size for melting curves is approximately 2.4 nm, suggesting that the melting curves are more suitable for evaluating moisture distribution in hcp.

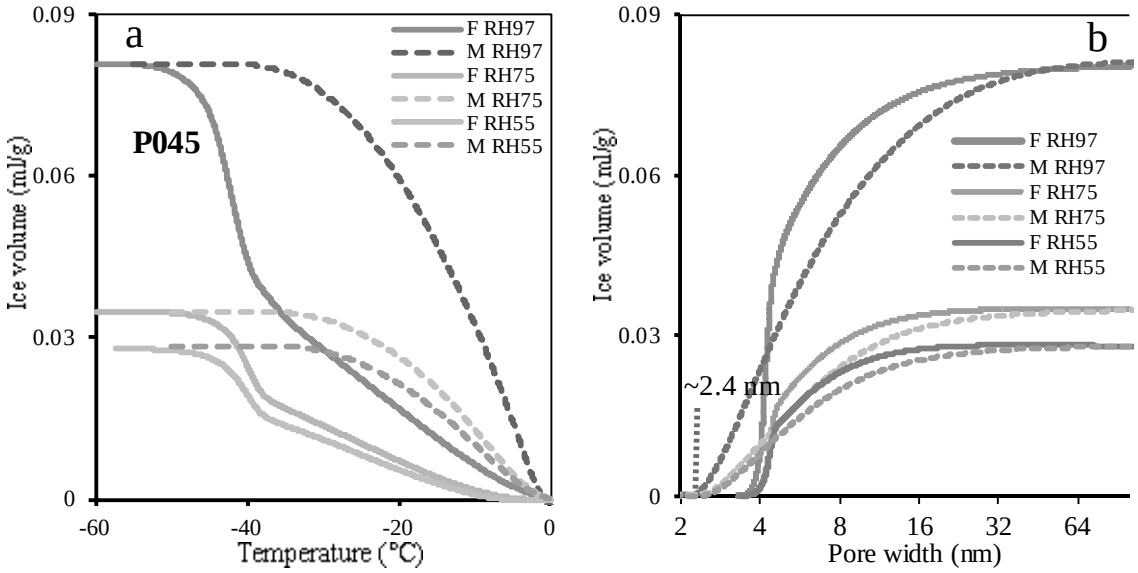


Figure 4.7. Ice volume distribution in P045 under different RH conditions. (a) Calculated ice volume under RH of 97 %, 75 %, and 55 % using Eq. (4.5), and (b) corresponding ice volume in nanopores based on Eq. (4.4) with respect to freezing (F) and melting (M) process: *Figure 2* in paper IV.

Figure 4.8 illustrates the detailed distribution of evaporable water in P045 and P145 during the drying process, categorized into four different intervals: < 2.7 nm, 2.7–10 nm, 10–20 nm, and > 20 nm. The change of water confined in the interlayer and gel pores is easily distinguishable from the data obtained from P045 and P145. The results indicate that water confined in the interlayer and small gel pores (< 2.7 nm) does not present any increase during the drying process. Under 75 % RH, water in capillary pores is almost fully evacuated, and there is a loss of more than half of the water in large gel pores [124] or interhydrate spaces (2.7–10 nm) [125,126]. The LT-DSC data reveals only a small loss of freezable water during a drying to 55 % RH compared to 75 % RH, and the major loss is detected in water confined in the interlayer and small gel pores. This can be ascribed to a coarsening of gel pores. A drying process at 33 % RH induces a minor increase in unfrozen water due to the movement of C-S-H sheets.

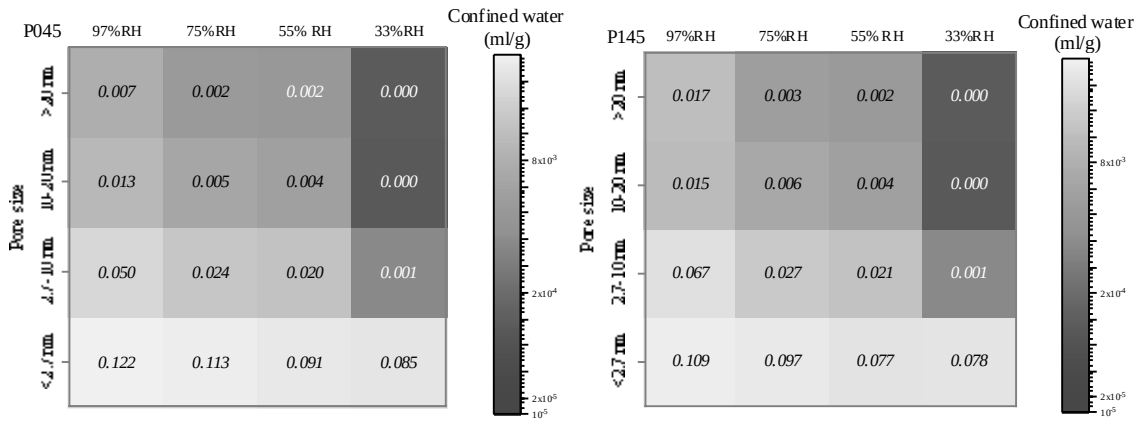


Figure 4.8. Moisture redistribution in P045 and P145 during the desorption equilibrium (*Figure 6* in paper IV).

### 4.2.3 Dynamics of water confined in hcp

Figure 4.9 shows that the comparison between the relaxation time of P145 with RH of 97 % and 33 %. Four relaxation processes were detected relating to the water behavior. The relaxation process 1 (R1) has the fastest relaxation dynamic and the lowest activation energy, which is attributed rotation/reorientation of hydroxyl in Si-OH environment [127] . Relaxation process 2 (R2) is the second fastest process, and it is more reasonable to be assigned as the dynamic of water molecular hydrating the silanol groups [128] or water confined in pores of smaller than 1 nm [129]. Relaxation process 3 (R3) is dynamics of the unfrozen water in pore with reduced hydrogen bonds and mixed with dynamics of hexagonal ice (ice $I_h$). Relaxation process 4 (R4) is a Maxwell–Wagner process, relating to interfacial polarization between liquid and solid face [130]. The saddle-like temperature dependence of relaxation time in between 1000/*T* of 3 and 4 is ascribed to the loss of evaporable water in matrix. This somehow can explain why R4 is missing in samples with RH of 33 %.

Relaxation of structural water (R1 and R2) is a β-process with Arrhenius dependence. The supercooled water in gel pores seems to have a Vogel–Fulcher–Tammann (VFT) dependence at high temperature range. This fragile-to-strong transition (from VFT to Arrhenius) occurs in supercooled water confined hydrophilic porous matrix [50,52]. However, the data in this study is insufficient for getting such a conclusion. R4 also has an Arrhenius dependence in temperatures below 250 K.

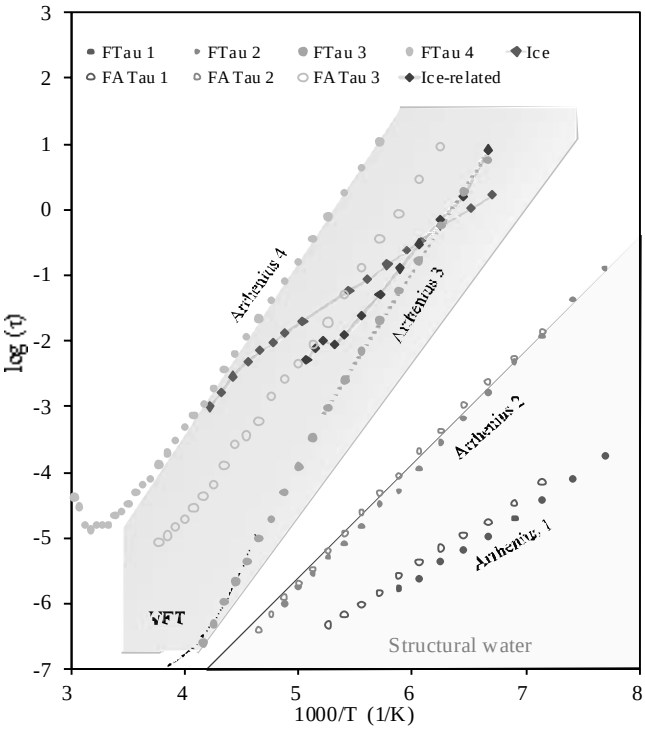


Figure 4.9. Comparison of relaxation times of P145 at RH of 97 % (FTau*) and 33 % (FATau*). Data of ice $I_h$ relaxation from [131] and ice-related relaxation in frozen tri-propylene glycol solution [132] are shown for comparison: Figure 9 in paper IV.

The comparison of fitting results with Arrhenius equation is presented in Table 4.1. The activation energy required for R1 lies in the range of 19.65 to 24.85 kJ/mol. These values are higher than the activation energy of Si-OH relaxation in xonotlite (17.28 kJ/mol or 0.18 ev) [127], but they are lower than that of the similar relaxation in Co-montmorillonite [133]. Fly ash and a further replacement of limestone seem to reduce the activation energy and increase the log($\tau_0$), but the effect is very limited. A drying of P145 at 33 % RH has almost no effects on both activation energy and the log($\tau_0$) of structural water compared with a conditioning at 97 % RH. Activation energy of R2 in binder systems has a value between 34.79 and 37.42 kJ/mol. The behavior of R2 is similar with that of process 2 observed in synthetic C-S-H [134] and tobermorite [127]. The activation energy of R3 is similar to the activation energy of diffusion of glassy bulk water (45 kJ/mol [135]) and lower than the activation energy of ice $I_h$ relaxation (~ 50 kJ/mol [131,136]). The addition of fly ash increases the activation energy of R3, which is likely due to the lower ion concentration in the pore solution. The effect of slag on this process is mainly observed in the non-Arrhenius temperature range; thus, P245 exhibits similar activation energy and log ($\tau_0$) as P045. When CEM I is partially replaced with limestone, the activation energy of R3 decreases. In comparison to CEM I paste, fly ash results in a lower activation energy of R4. Slag has little effect on the activation energy of R4, but it increases the value of log($\tau_0$).

Table 4.1. Regression of the temperature dependence of water related relaxation processes in hcps with RH of 97 % and P145 with RH of 33 %.

| Mix ID | Relaxation | Slope (k) | log($\tau_0$) | $R^2$ | $E_a$ (kJ/mol) |
|---|---|---|---|---|---|
| P045 | R1 | 1.237 | -13.25 | 0.998 | 23.67 |
| | R2 | 1.946 | -15.78 | 0.999 | 37.24 |
| | R3 | 2.607 | -17.02 | 0.996 | 49.90 |
| | R4 | 2.896 | -16.52 | 0.997 | 55.42 |
| P145 | R1 | 1.119 | -12.39 | 0.998 | 21.41 |
| | R2 | 1.818 | -14.89 | 0.999 | 34.79 |
| | R3 | 2.671 | -16.97 | 0.998 | 51.11 |
| | R4 | 2.500 | -13.29 | 0.999 | 47.84 |
| P245 | R1 | 1.297 | -13.63 | 0.997 | 24.82 |
| | R2 | 1.836 | -15.11 | 0.998 | 35.13 |
| | R3 | 2.582 | -16.91 | 0.996 | 49.41 |
| | R4 | 2.870 | -15.68 | 0.996 | 54.92 |
| P345 | R1 | 1.027 | -11.85 | 0.998 | 19.65 |
| | R2 | 1.944 | -15.73 | 1 | 37.20 |
| | R3 | 2.196 | -14.50 | 0.994 | 42.02 |
| | R4 | 2.831 | -15.68 | 0.999 | 54.17 |
| P145RH33 | R1 | 1.146 | -12.36 | 0.998 | 21.93 |
| | R2 | 1.832 | -14.85 | 0.999 | 35.06 |
| | R3 | 2.484 | -14.68 | 0.998 | 47.53 |

## 4.3 Chapter summary

Water vapour desorption isotherm provides effective information of the mesoscale pore structure in hcp. It is essential to consider the effect of ions on the equilibrium pressure of water vapour on a plane surface when calculating the pore size distribution using the BJH model. The novel approach based on water vapour sorption and thermodynamic modelling performs well in the evaluating the hydration degree of SCMs. It has been observed that the presence of SCMs markedly increases the moisture in hcp at RH above 50 %. This is attributed to their effect on increasing the volume of large gel pores and capillary pores. Cavitation occurs during the desorption of water vapour at RH between 36 % and 30 %, which can result in an overestimation of the volume of the small gel pores. Nonetheless, the increase in the cavitation-induced value reveals the refinement effect of SCMs. Furthermore, the dilution effect from SCMs provides essential extra water for achieving full hydration of the clinker.

During the drying process, moisture in hcp undergoes a redistribution due to the dynamic microstructural changes. Thermoporometry is an effective method for characterising the moisture distribution. The melting curve is preferable to the freezing curve for evaluating water confined in hcp, and it enables to perform measurement of the water confined in pores larger than ~2.4–2.7 nm. Regardless of the temperature to which the water is frozen, water in pores smaller than the critical value, including interlayer and partial gel pores, will not form a tetrahedral ice structure. The influence of SCMs on the distribution of moisture has been found to extend beyond the equilibrium state at 97 % RH to affect redistribution during the drying process down to 33 % RH. Although some discrepancies in the discussion of dynamic pore structure changes during the initial drying process have been observed between previous publications [137–139], this study affirms that, under equilibrium conditions, the drying process does not induce any increase in volume of pores smaller than 2.7 nm. A sever coarsening of small pores occurs during the drying process between RH values of 75 % and 55 %. SCMs have a limited effect on the dynamics of structural water, primarily influencing the dynamic of water in small gel pores and interfacial polarization.

# 5 Effect of SCMs on moisture and chloride transport

*Moisture transport properties play crucial roles in determining the performance of cement-based materials during construction process and the long-term service. The humidity levels in the concrete substrate before applying any covering material are directly linked to the risk of cracking and mould growth. Moisture also influence the transport of $CO_2$, $O_2$, and chloride ions in concrete, which ultimately determine the deterioration process of reinforced concrete structures [37,140]. Effect of SCMs on both water transport and chloride migration in cement-based material will be investigated to provide better understanding for the design of more durable cement-based materials. The impact of SCMs on pore structure in pastes will be analyzed by interpreting various parameters. Finally, the moisture and chloride transport characteristics of pastes blended with different SCMs will be comprehensively compared to the pore structure parameters. This chapter summarises the content of paper V and VI.*

## 5.1 Moisture transport

This section elaborates moisture transport properties of hcp measured by a novel method with the corresponding procedures, as described in [28,58]. This method enables the measurement of both water vapour diffusion coefficient ($D_v$) at steady state, total moisture transport coefficient ($D_w$) and water vapour diffusion coefficient by semi-infinite drying ($D_{v,s}$) for the same sample in a single procedure. The influence of *w/b* and SCMs on the moisture transport properties will be discussed in detail.

### 5.1.1 Water vapour diffusion at steady state

Figure 5.1 presents $D_v$ of hcp measured by the tube method within four different RH intervals. It is important to note that all "$D_v$" values in the figures represent the average diffusion coefficient within a specific RH interval. It has been observed that a higher RH interval leads to a higher deviation within three parallel tests. However, it is worth mentioning that the tube

method shows a lower level of deviation compared to the cup method, as reported in [38]. Therefore, the tube method, as described in detail in paper V, is a reliable and valid alternative to traditional cup methods for measuring vapour diffusivity under steady-state conditions.

For pastes with *w/b* of 0.35, the fly ash binary paste has the lowest $D_v$ within all RH intervals, with a value smaller than half of that in CEM I paste (P035). Effect of slag on the vapour diffusion at steady state depends on the RH intervals. It induces a reduction in coefficient measured in RH intervals above 75 % but enforces a minor increase in coefficient between RH of 75 and 50 %. The impact of SCMs on vapour diffusion reduction is more pronounced at the higher *w/b* and at RH intervals above 62.8 % (between 75.5 % and 50 %). For example, the $D_v$ of slag blended paste is only 0.52, 0.29, and 0.14 of CEM I paste for *w/b* ratios of 0.35, 0.45, and 0.55, respectively. A higher *w/b* causes an increase in the vapour diffusion coefficient for all pastes. An increase of the *w/b* from 0.35 to 0.55 induces an elevation in the coefficient of slag blended and CEM I paste, with a factor of approximately 2.5 and 10, respectively. The further replacement of CEM I with limestone generally leads to an increase in the vapour diffusion. However, this effect is negligible at the higher RH intervals.

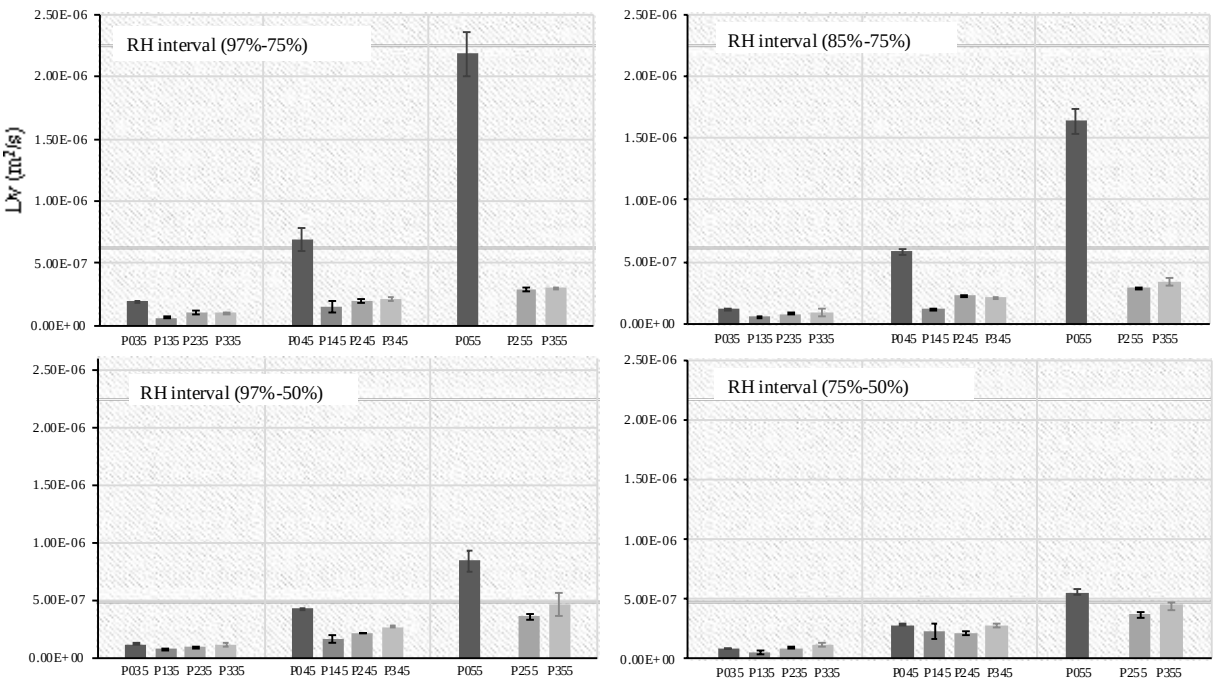


Figure 5.1. Water vapour diffusion coefficient of hcp measured by the tube method in four different RH intervals.

Apparently, the measured vapour diffusion coefficient depends on the RH intervals. There is a significant increase in the $D_v$ of CEM I pastes as RH increases. $D_v$ of pastes blended with SCMs seems to be independent on RHs. However, An increase in the $D_v$ can be observed as the RH level reaches a higher range (94.6 % to 97.6 %) in both the adsorption and desorption processes, as depicted in [38]. As shown in Figure 5.2, moisture transport in cement-based materials involves the transportation of both gas (vapor) and liquid phases under non-saturated

conditions, where the pore volume is only partially filled with the liquid phase. The dominance of either process depends on saturation state. Before the liquid phase achieves contiguous connection (percolation) at the critical RH condition, the moisture transport process is dominated by vapor diffusion. In contrast, a Darcian transport of the liquid phase is prominent after percolation, resulting in particularly high transport coefficients. Therefore, at high RH intervals, the results from the cup method will overestimate vapor diffusion due to liquid flow mixing. Baroghel-Bouny [37] provided a detailed explanation of this phenomenon. The RH dependence of measured $D_v$ is well described by equation (14) in paper V [28], and Figure 5.2 presents the representative results in the top left corner.

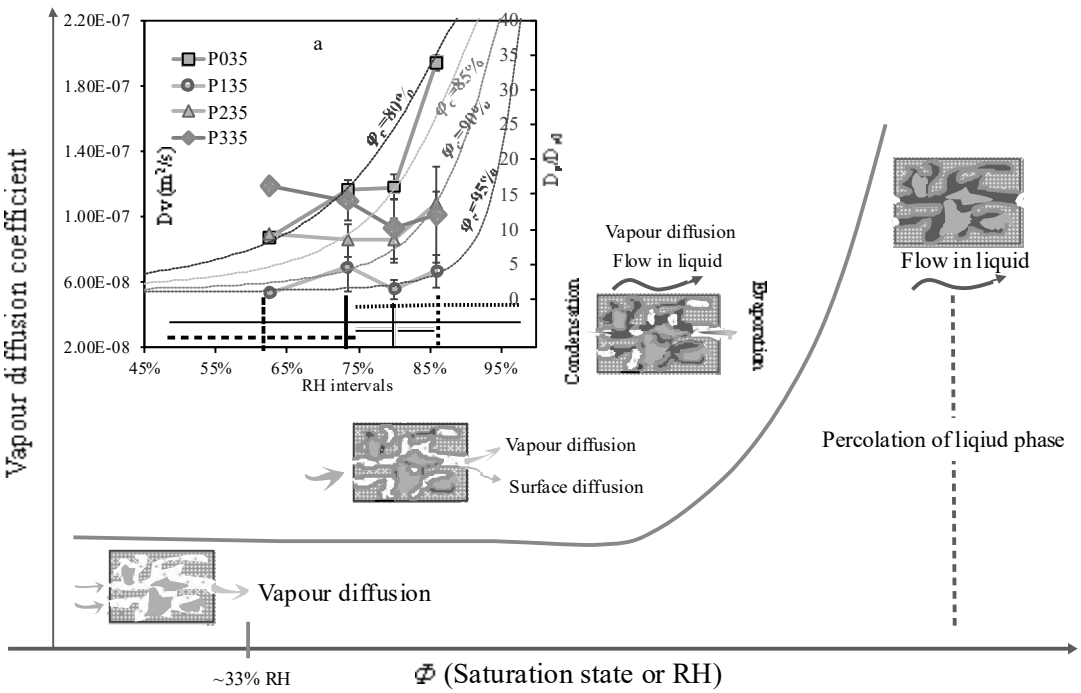


Figure 5.2. Illustration of dependence of water vapour diffusion coefficient, exampling with *w/b* of 0.35.

### 5.1.2 Moisture transport during the first drying

The total moisture transport coefficient ($D_w$) can be measured by the semi-infinite drying. Using $D_w$ and the moisture content at the drying RH enables to calculate the water vapour diffusion coefficient under the drying process ($D_{v,s}$). This has been demonstrated in paper V in detail.

Figure 5.3 shows the moisture transport coefficient for hcps dried at RH of 75 % and 50 %. Pastes dried at 75 % RH exhibit lower $D_w$ values compared to those dried at 50 % RH. $D_w$ is dependent on the moisture content of cement-based materials. As the degree of saturation increased from zero, $D_w$ decreased and reached its minimum value at a saturation degree of 0.5-0.8. Once the liquid percolation threshold was reached, $D_w$ increased with the saturation

degree [37]. Blending SCMs leads to a significant decrease in $D_w$ during drying at both 50 % and 75 % RH. While drying at RH of 50 %, the reduction in $D_w$ caused by SCMs is most noticeable in the hcp with fly ash and a *w/b* of 0.45. With a further replacement of limestone, the effect of slag in $D_w$ weakens, resulting in a $D_w$ of ternary paste almost twice as that of the binary paste containing slag.

The effect of drying RH on $D_{v,s}$ is comparable to its effect on $D_w$ . However, the variation in $D_{v,s}$ between different RH levels is less pronounced than that in $D_w$. This phenomenon is particularly noticeable in blended paste, which may be due to the greater moisture capacity of blended pastes compared to CEM I paste. Effect of SCMs on water vapor diffusion at drying will be amplified at a higher *w/b*, which is similar with the finding in water vapor diffusion at steady state.

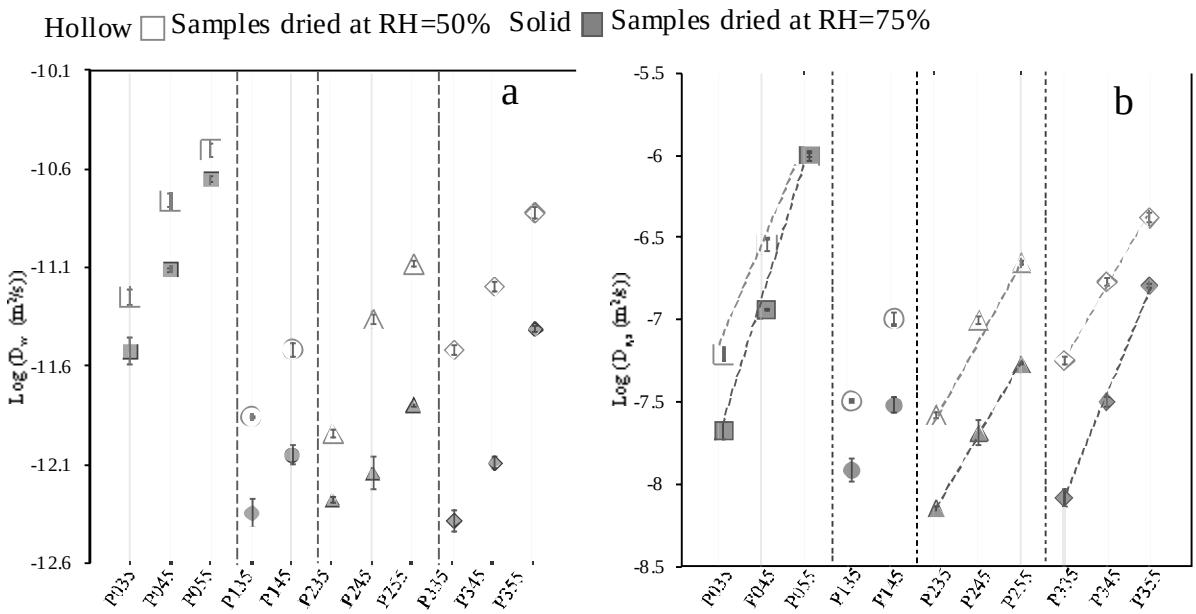


Figure 5.3. The total moisture transport coefficient $D_w$ and water vapor diffusion coefficient during semi-infinite drying $D_{v,s}$ at RH=50 % and 75 % (20 ℃), respectively: a- $D_w$ of all pastes; b- $D_{v,s}$ of all pastes: adopting from *Figure 2* in paper V.

## 5.2 Effect of SCMs on chloride migration

Chloride migration coefficient in cement-based material is crucial for predicting the service life of concrete structures exposed to marine and saline environment. This parameter is time-dependent and decreases over time due to the continuous hydration of binders, following an empirical power function [141,142]. Table 5.1 presents the chloride migration coefficient of various pastes at different curing times, tested by the rapid chloride migration (RCM) method. Generally, the chloride migration coefficient ($D_{RCM}$) decreases as curing time increases, except for P055, which shows an unexpected increase. Additionally, an increase in *w/b* causes an increase in $D_{RCM}$, although the influence of *w/b* on $D_{RCM}$ of slag binary paste at 180 d is

relatively weak. Blending of SCMs in reduces the chloride migration coefficient, particularly in pastes with a longer hydration time and higher *w/b* ratios. Fly ash has the strongest effect on the reduction of DRCM after 180 d. Interestingly, $D_{RCM}$ of P055 exhibits an increase with hydration time after 28 d, which has also been observed in some previous studies [141,142]. It was found that Portland cement-based concrete may have a higher chloride migration coefficient at a later age when the *w/b* ratio is relatively high (> 0.5).

Table 5.1. The $D_{RCM}$ of pastes cured to 28, 90 and 180 d.

| Time/days | Chloride migration coefficient ($\times 10^{-12}$ $m^2/s$) | | | | | | | | | | |
|---|---|---|---|---|---|---|---|---|---|---|---|
| | P035 | P045 | P055 | P135 | P145 | P235 | P245 | P255 | P335 | P345 | P355 |
| 28 | 8.02 | 15.56 | 21.08 | 8.90 | 11.35 | 5.12 | 5.82 | 7.29 | 5.79 | 5.39 | 6.40 |
| 90 | 5.84 | 11.67 | 26.28 | 2.27 | 3.67 | 3.17 | 3.85 | 4.52 | 2.70 | 3.64 | 3.81 |
| 180 | 3.52 | 10.46 | 26.15 | 0.84 | 1.51 | 2.50 | 2.60 | 2.91 | 1.76 | 1.94 | 3.71 |

In the practical application scenario, the exposure environment is much severer than the lab room. Figure 5.4 presents a comparison of the chloride profile in concretes after a 20-year exposure under a de-icing salt road environment in Sweden. It shows that substituting Swedish structural cement with 5 % silica fume has little impact on chloride penetration. However, the benefits of reducing chloride content become more apparent when the replacement ratio increases to 10 % silica fume. For the concrete made with Finnish rapid Portland cement containing 10–15 % limestone filler, blending of ground granulated blast-furnace slag seems to have very limited effect on the penetration front of the chloride at *w/b* of 0.4. It even caused an increase in the chloride content at depth lower than 20 mm. However, its inhibiting on the chloride ingress is much evident in concrete with *w/b* of 0.5, especially in the depth larger than 20 mm. It implies that the effect of slag on the chloride migration in practical environment still depends on the binder types and *w/b*.

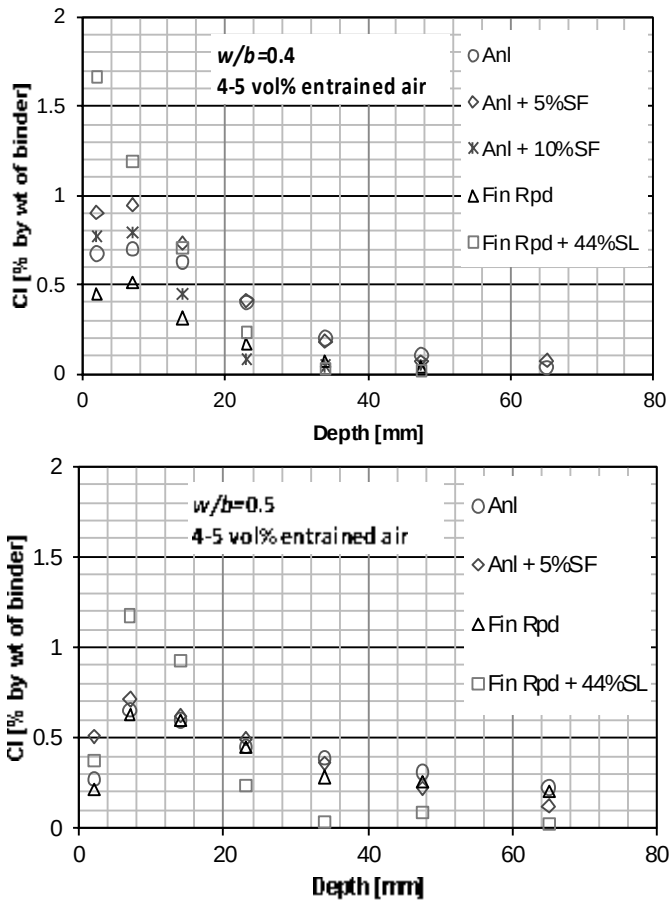


Figure 5.4. The chloride profile in concretes after an exposure of 20 years under a de-icing salt road environment adopted from *Figure 4* in paper VI [42]. Notes: Anl- Swedish structural cement, SF- Silica fume, SL- Finnish ground granulated blast-furnace, Fin Rpd- Finnish rapid Portland cement blended with 10–15 % limestone filler.

## 5.3 Refinement of pore structure

Mercury intrusion porosimetry measurement is a useful method for obtaining comparative indices of pore structure in cement-based materials by testing the threshold diameters of intrudable pore space. The pore size corresponding to the peak in the *dV/dlog(D)* curve is known as the critical entry pore size [143]. Figure 5.5 shows that under sealed curing conditions after 390 d, the incorporation of fly ash in pastes with *w/b* of 0.35 and 0.45 induces a decrease in the critical entry pore size. Conversely, the use of slag results in a minor increase in this critical size compared with CEM I paste. This means that in the change of critical entry pore size cannot explain the much lower moisture transport coefficients of the blended pastes (as shown in Figure 5.1 and 5.3), which was considered to be a significant factor controlling moisture transport in previous publications [39,144]. It has been observed that slag can reduce the critical entry pore size of pastes at a later age when cured in water [9]. This is because such a curing provides adequate amount of water in the large capillary pores, which enables the hydration products to precipitate and fill these pores during the later hydration of slag. However, the sealed curing may not induce this effect due to the limited availability of water.

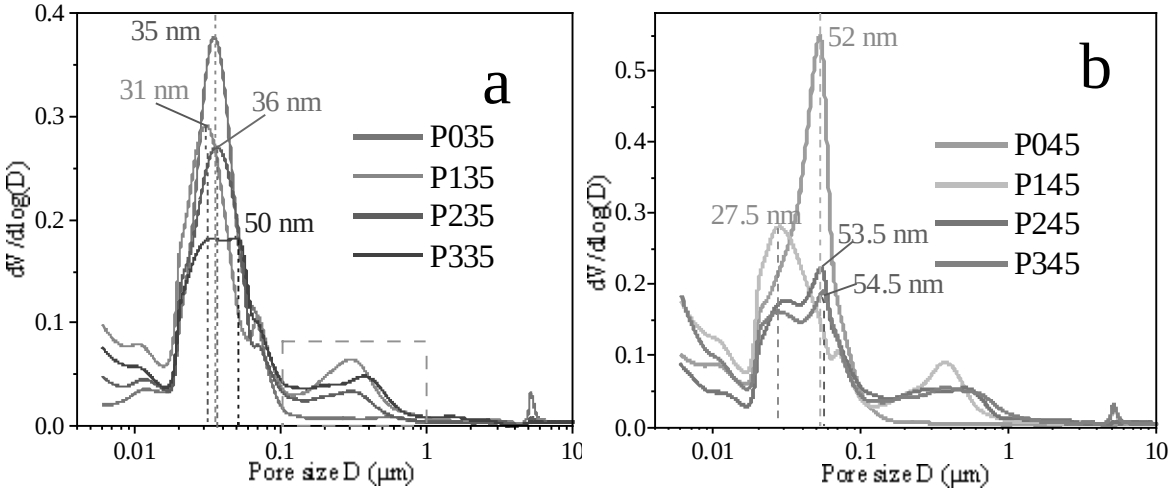


Figure 5.5. Pore size distribution of hcp after a sealed-curing for 390 d measured by mercury intrusion porosimeter, adopted from *Figure 6* in paper V [28].

Formation factor and pore connectivity are related to the transport properties of cement-based materials as described by equation (1) in paper V. To find out the real refinement effect of SCMs, these two parameters have been calculated and presented in Table 5.2. Blending of SCMs decreases not only the conductivity of pore solution but also the pore connectivity and inverse of $F$. The tendency of pore connectivity ($\beta$) with respect to variations in $w/b$ and binder types is similar to that of $1/F$. As the $w/b$ increases, both $1/F$ and $\beta$ present a significant increase. Fly ash causes a substantial reduction in $1/F$ compared with CEM I paste, with a reduction factor of approximately 1/8.5 and 1/20 in pastes with $w/b$ of 0.35 and 0.45, respectively. The $1/F$ the slag blended pastes is also much lower than that of CEM I paste with the same $w/b$, 0.45, and 0.55, respectively. The ternary pastes exhibit a similar $1/F$ or $\beta$ as the slag binary pastes. It is apparent that the real refinement effect of SCMs is to reduce the pore connectivity.

Table 5.2. Properties of pastes at approximately 1 year (390 d), including electrical conductivity, pore solution conductivity, inverse of $F$, porosity, and pore connectivity.

| Sample | Electrical conductivity (mS/cm) | | $1/F$ | $\Phi$ | $\beta$ |
|---|---|---|---|---|---|
| | Paste | Pore solution | | | |
| P035 | 0.251 | 165.9 | $1.52\times10^{-03}$ | 0.19 | $7.84\times10^{-05}$ |
| P045 | 0.701 | 131.3 | $5.34\times10^{-03}$ | 0.26 | $2.07\times10^{-02}$ |
| P055 | 1.249 | 102.9 | $1.21\times10^{-02}$ | 0.35 | $3.45\times10^{-02}$ |
| P135 | 0.019 | 104.4 | $1.78\times10^{-04}$ | 0.24 | $7.48\times10^{-04}$ |
| P145 | 0.026 | 96.0 | $2.71\times10^{-04}$ | 0.28 | $9.82\times10^{-04}$ |
| P235 | 0.075 | 149.6 | $4.98\times10^{-04}$ | 0.19 | $2.60\times10^{-03}$ |
| P245 | 0.128 | 114.5 | $1.12\times10^{-03}$ | 0.23 | $4.85\times10^{-03}$ |
| P255 | 0.167 | 111.6 | $1.50\times10^{-03}$ | 0.27 | $5.46\times10^{-03}$ |
| P335 | 0.070 | 133.3 | $5.26\times10^{-04}$ | 0.20 | $2.60\times10^{-03}$ |
| P345 | 0.085 | 86.9 | $9.75\times10^{-04}$ | 0.24 | $4.01\times10^{-03}$ |
| P355 | 0.111 | 78.0 | $1.42\times10^{-03}$ | 0.25 | $5.60\times10^{-03}$ |

## 5.4 Transport properties in relation to pore structure

### 5.4.1 Correlation between $D_v$, $F$ and porosity

As $D_v$ in hcp is moisture-dependent, Figures 5.6a–c show separate plots for correlations at different RH intervals. $D_v$ at RH97–75 presents a linear relation to the $1/F$ of hcp. This indicates that the pore connectivity, rather than porosity, determines $D_v$ at high RH intervals. The blended pastes exhibit much lower pore connectivity than CEM I pastes, which results in a much lower vapor diffusion coefficient at high RH intervals compared to CEM I pastes. As RH interval decreases to RH97–50, the connectivity of the pore solution declines significantly, causing a de-percolation of liquid phase. Therefore, the moisture transport process is primarily determined by porosity, as depicted in Figure 5.6d.

Even though both $1/F$ and $\beta$ of the blended pastes are substantially lower than that of CEM I (Table 5.2), the $D_v$ of blended pastes is similar to that of CEM I with the same $w/b$ in RH75–50. Furthermore, the slope of the regression line in the blended hcp increases with the decrease of RH levels. It implies that the major determinant of $D_v$ shifts from pore connectivity to porosity. It is noteworthy that the data of fly ash blended pastes with $w/b$ of 0.45 deviate from the fitting line of the blended pastes, owing to their much lower pore connectivity compared to the slag blended hcp.

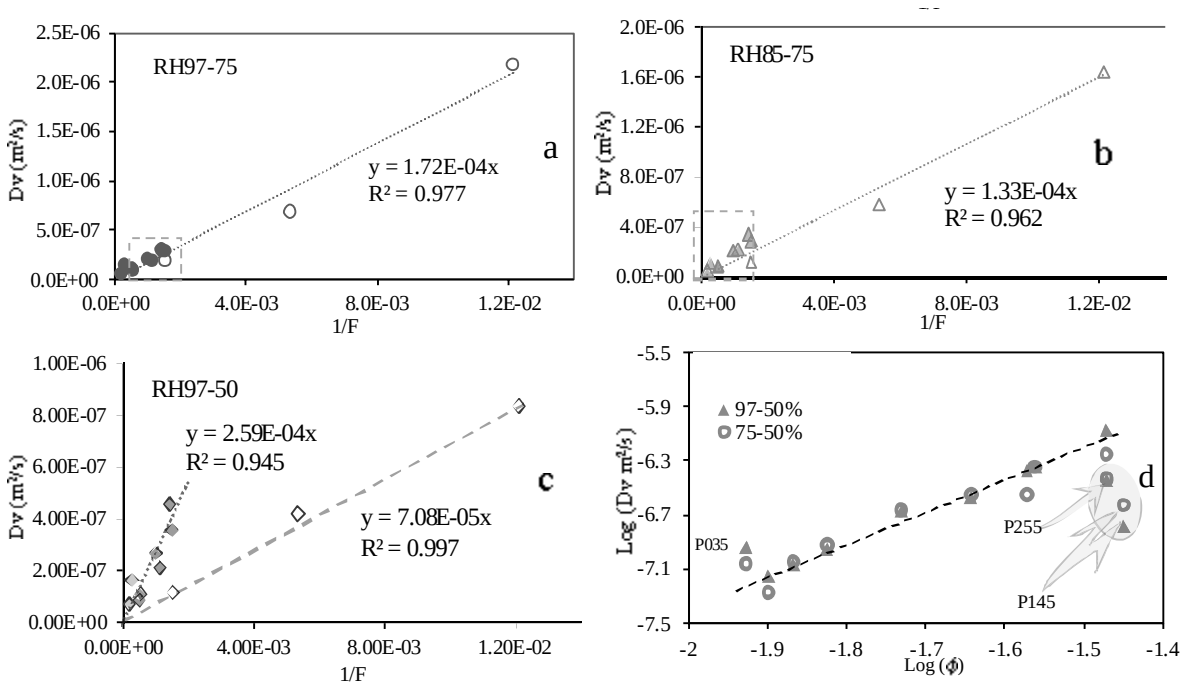


Figure 5.6. The water vapour diffusion coefficient in relation to $1/F$ and porosity. The hollow marks are the data of CEM I, the solid marks are the data of the blended pastes and the marks filled with green color are fly ash blended pastes.

### 5.4.2 Relationship between $D_{RCM}$ and $1/F$

The ion transport coefficient in the paste linearly correlates to the pore structure parameter $F$ and its transport coefficient in the pore solution [88,90]. If we assume that the binding capacity of the hydration products can be neglected, the non-steady-state migration of chloride under an applied electric field, $D_{RCM}$, can be estimated by the use of $F$. $D_{ps}$, the chloride migration coefficient in the bulk pore solution, is often assumed to be $2.03 \times 10^{-9}$ ($m^2/s$) [33], although The value could potentially be smaller as a result of interactions with other ions in pore solution.

$$D_{RCM} = \frac{D_{ps}}{F} \tag{5.1}$$

Figure 5.7 shows that in general the $D_{RCM}$ of all the pastes is located close to the modelled line (dash line in Figure 5.7). However, the data of pastes with *w/b* of 0.35 deviate from the general curve. Because pastes with a sealed curing were used to measure the conductivity, the pastes with *w/b* of 0.35 are far from the saturation state under this curing condition. However, the $D_{RCM}$ was tested under the nearly saturated condition which might result in a deeper chloride penetration depth thus a higher value of $D_{RCM}$. The data of Chidiac and Shafikhani [145] has been normalized to the volume of mortar to fit in the figure. It shows that $D_{RCM}$ of all the mortar generally locates close to the modelled line as well. Therefore, it can be concluded that the pore connectivity or $F$ of hcp should be a key controlling factor on the chloride migration in cement-based materials.

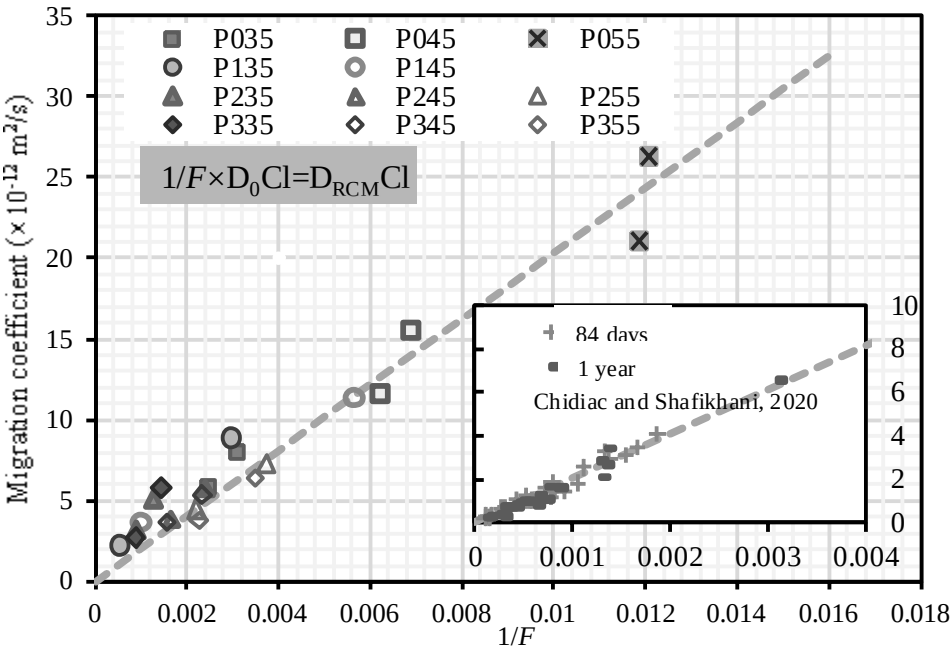


Figure 5.7. The correlation between chloride migration coefficient and $1/F$ with data in this study at curing time of 28 and 90 d and data adopted from [145].

## 5.5 Chapter summary

SCMs evidently reduce the moisture transport coefficient of hcp after curing for 390 d. Slag decreases the chloride transport rate in the hcp, and effect of fly ash on improvement of chloride resistance shows after 90 d curing. Both fly ash and slag have a great reducing effect on the pore connectivity in the pastes after a long-term curing. The ternary pastes with limestone have the similar $F$ with the binary slag blended pastes after 1 year. A higher *w/b* provides more water for the later hydration of fly ash and slag, which increases their refining effect on the pore structure. Thus, increasing the *w/b* amplifies the impact of SCMs on moisture transport and chloride migration coefficient in hcp. Moisture content in hcp plays a crucial role in the moisture transport due to water condensation in its porous structure. Blended pastes exhibit a more complex pore structure, resulting in that vapour diffusion coefficient ($D_v$) of the blende pastes shows a very weak RH dependence at measured RH intervals.

There are many parameters describing pore structure of hcp, such as porosity, pore connectivity, pore size distribution, the critical entry pore size, and formation factor. Critical entry pore size is not the main controlling factor for moisture transport. The improved resistance to moisture in the blended system is primarily attributed to the pore structure refinement. The refinement effect mainly reflects on the reduction in pore connectivity. The moisture transport properties in the hcp are determined by both the formation factor and the porosity of small pores, specifically volume of the middle capillary and mesoscale pores. However, at high RH the formation factor is the primary factor affecting moisture transport, whilst at low RH, the porosity of small pores is the main factor. Effect of SCMs on the chloride resistance of concrete depends on the *w/b*, and the effect of slag is pronounced after 20-years of exposure under a road environment for mixture with *w/b* of 0.5. A highly simplified model was developed to estimate the chloride migration coefficient with only one measured parameter $F$ of hcp. This model is valid to calculate the $D_{RCM}$ of both plain and blended pastes as well as mortars.

# 6 Monitoring the hardening process of the blended concrete

*Traditional methods for testing the hardening of concrete require the strict control of temperature and humidity, which is very different from the field conditions. The non-destructive test is useful for ensuring the application quality of SCMs in field construction. It is also essential for the digital fabrication. This chapter will present an upgraded system based on the previous version in paper II to replicate the setting and strength development of concrete containing SCMs. The content of this chapter is from paper VII.*

## 6.1 Electrical conductivity

### 6.1.1 Calibrating the dimension effect

The calculation of electrical conductivity using Wenner's method assumes a semi-infinite boundary condition. However, in practical applications, the size of the concrete specimen does not satisfy this boundary, particularly for the upper rows of sensors. To investigate the impact of dimension on the calculation of electrical conductivity, a numerical simulation was performed using COMSOL Multiphysics with a geometry similar with that of the container (see Figure 6.1). In this simulation, the AC/DC mode was employed with the electric current conservation equation, and the boundary conditions were set such that all surfaces of the geometry were insulative. The matrix was set to a constant electrical conductivity of 0.1 mS/cm, and a constant input current of 0.1 mA was applied from point A to point B.

The simulated potential difference between V2 and V1 was used to calculate the electrical conductivity by Wenner's method. The dimension factor ($\gamma$) was evaluated by dividing the given conductivity with the calculated one. Figure 6.1 shows that $\gamma$ is about 1.96 at the first row and decreases with depth. From these simulated results the relationship between $\gamma$ and the depth of sensors ($x$) can be established. The simulated values have been validated with the standard

solutions (KCl), and it is confirmed to be very close to the experimental value (see table in Figure 6.1).

***Dimension factor for calibration***

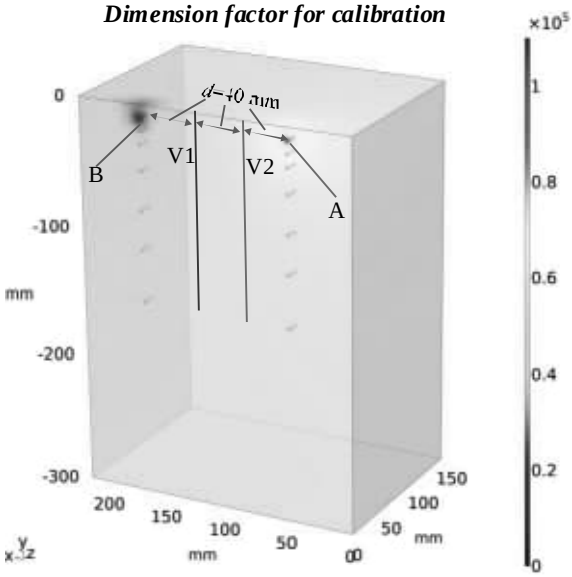


Given electrical conductivity [0.1 mS/cm]
Applied constant current [10 mA] from A to B

Run one simulation at Each depth to get the value in table below

| Depth [mm] | V1 [mV] | V2 [mV] | ΔV [mV] | Calculated conductivity based on semi-infinite assumption | Dimension factor | |
|---|---|---|---|---|---|---|
| | | | | | Simulated | Experiment |
| 10 | 51245 | 43459 | 7786 | 0.051 | 1.96 | 1.91 |
| 20 | 47015 | 40443 | 6572 | 0.061 | 1.65 | 1.54 |
| 30 | 45570 | 39833 | 5737 | 0.069 | 1.44 | 1.40 |
| 50 | 43865 | 39001 | 4864 | 0.082 | 1.22 | 1.22 |
| 80 | 43173 | 38728 | 4445 | 0.089 | 1.12 | 1.10 |
| 110 | 43121 | 38786 | 4335 | 0.092 | 1.09 | 1.09 |
| 150 | 43026 | 38730 | 4296 | 0.093 | 1.08 | 1.07 |

Wenner method for electrical conductivity at semi-infinite ground

$$\sigma = \frac{I}{2\pi\Delta V d}$$

**Dimension factor [γ]=Given value/Value with semi-infinite assumption**

Figure 6.1. Evaluation of dimension factor by the numerical simulation and experiments, corresponding to *Figure 2* in paper VII.

### 6.1.2 From paste to concrete

After including the temperature and dimension factor, the real-time electrical properties of hydrating concrete were calculated and shown in Figure 6.2. To calculate the formation factor ($F$) of concrete sample, the conductivity of pore solution is assumed to be the same as that in paste (as shown in Figure 3.7). This treatment is based on two assumptions: (1) the presence of aggregates has very limited influence on the hydration of binders; (2) the temperature change induced by the heat release shows minor effects on the ion concentration of pore solution. It should also be noted that the conductivity of pore solution in C338 is estimated by multiplying value of paste with *w/b* of 0.35 by a dilution factor of 1.09 (= 0.38/0.35).

$$F_c = \sigma_{ps}(t)/\sigma_c(t) \tag{6.1}$$

where $\sigma_c(t)$ is the monitored electrical conductivity of concretes.

The influence of aggregates on the electrical characteristics is assessed by comparing formation factor of concrete specimens ($F_c$) with that of pastes ($F_p$) with the same *w/b* ratio. This ratio is also equivalent to the ratio between conductivity of pastes and that of concrete.

Figure 6.2 presents the electrical conductivity, $F$ of concrete and the ratio of $F$ between concrete and paste. Compared to conductivity of pastes, a similar tendency of evolution was detected during the hydration of concrete. The upgraded system (in paper VII) is better than the old version (paper II) in monitoring electrical conductivity before final setting, since it can obtain more stable and smooth data due to a modification on eliminating polarization effects. During

the continuous decrease from 4 h to 20 h, a peak occurs in electrical conductivity of all samples. The time for this peak coincides with the second reaction period of aluminate with the presence of sulfates. The second aluminate peak causes a subsequent depletion of sulfate ions in the pore solution [146], so concentration of hydroxyl ions will increase in order to maintain electrical balance. As hydroxyl ions are more conductive than sulfate ions, the conductivity of the pore solution increases (see C255 in Figure 6.2a).

The initial formation factors are almost constant. The ternary concrete has the highest formation factor over hydration time up to 168 h. Although the formation factor of C255 is lower than C145 before 86 h due to a higher *w/b*, it grows higher than that of fly ash binary concrete afterwards. Figure 6.2c shows that aggregates will reduce the electrical conductivity of matrix by a factor of 2–7. Before setting, the factor is nearly equivalent to the ratio between the value of solid/water in concrete and that in pastes by volume. As the hardening process progresses from 6 h to 16 h, the factor increases to a peak and then decreases significantly to values similar with the ratio of volume fraction of mixing water in pastes and that in concretes.

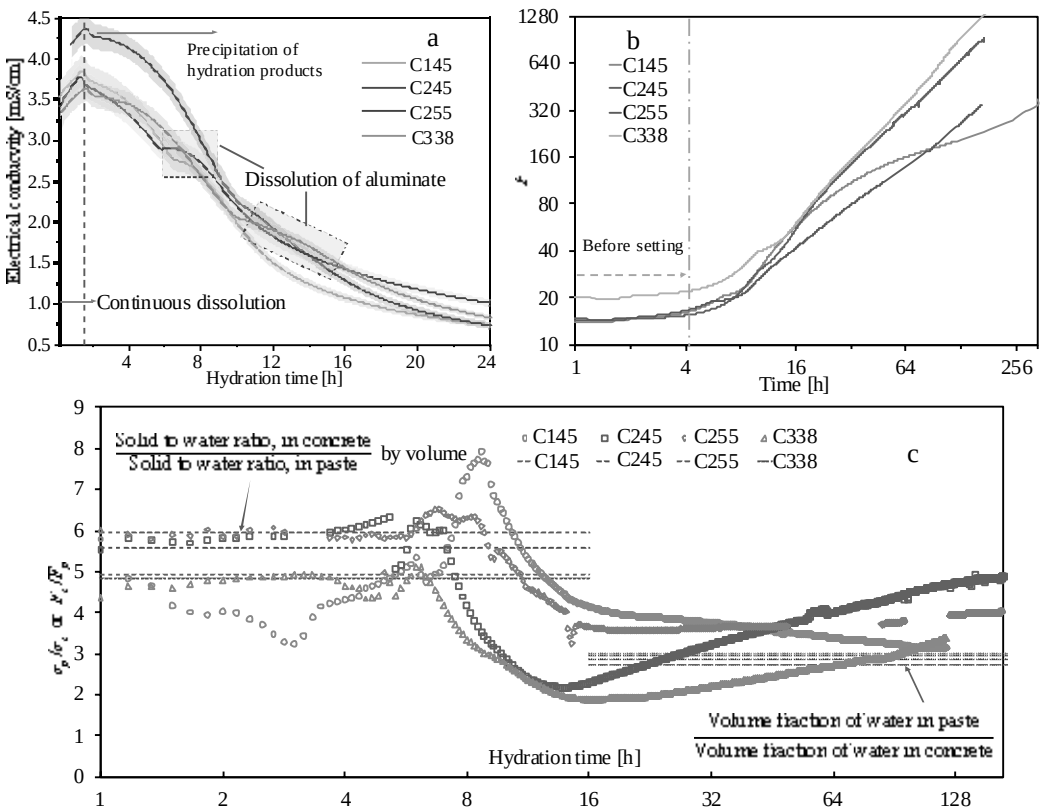


Figure 6.2. The monitored electrical properties of concretes: graph a – evolution of electrical conductivity; graph b – formation factor of concretes: graph c – the difference between electrical properties of paste and concrete, note that C338 was evaluated based on P335: corresponding to *Figure 3* in paper VII.

## 6.2 Ultrasonic pulse velocity

According to Figure 6.3, the ultrasonic pulse velocity (UPV) of concrete remains nearly constant before 2 h due to the limited consumption of free water. This period corresponds to the induction time of cement hydration, during which the UPV of the fresh concrete is primarily

governed by the volume fraction of solids. Some slight variations in the sequence may occur due to temperature effects. After the slow rate period, the precipitation of hydration products starts to build connections between particles, leading to an increase in UPV. The growth of particle connection is faster in C145 than in C255 owning to the lower *w/b*, which results in a higher UPV of C145 than that of C255 after 4 h.

The square of UPV ($v^2$) has a linear correlation with elasticity parameter of materials is, which can be described by the dynamic Young's modulus and dynamic Poisson's ratio [147]. Therefore, the change rate of elasticity can be inferred from the value of $dv^2/dt$, as shown in Figure 6.3b. C245 has the highest $dv^2/dt$ in the first 4 h. The increase in $dv^2/dt$ of C145 occurs later than C245, but the curve shape of these two concretes is similar. From 4 h to 8 h, C255 has the lowest $dv^2/dt$ due to its high *w/b*. This could also result from the low growth rate of solid connection caused by the dispersive distribution of the precipitated hydration products on particle surfaces [68,148]. From 12 h to 18 h, there is an increase in the growth rate of elasticity in C245 and C338 due to the aluminate reaction. The higher peak indicates that the dynamic modulus of C338 grows faster than C245, likely due to the accelerating effect of fine limestone powder on hydration after 4 h.

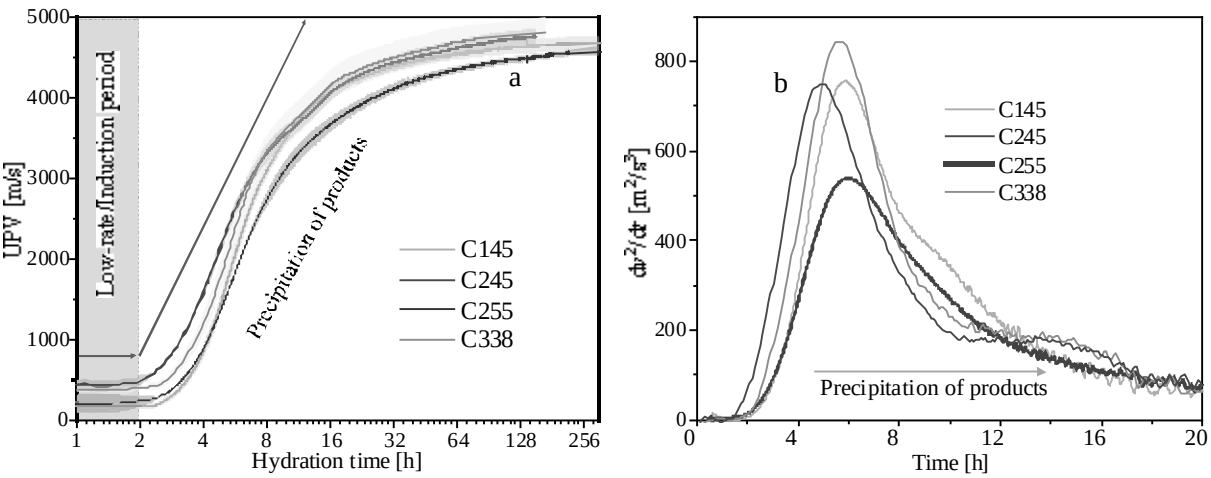


Figure 6.3. Monitored UPV in hydrating concrete (a) and $dv^2/dt$, corresponding to *Figure 5* in paper VII.

## 6.3 Comparison with traditional methods

### 6.3.1 Penetration resistance

The percolation theory of consolidation has been extensively employed to comprehend the mechanics of soil during its drying process [149]. Although Pellenq and Damme [150] emphasized that the setting of cement-based materials differs from soil hardening by "wetting" rather than "drying", the physics underlying concrete setting is similar to soil drying in that both processes involve the formation of solid networks to a percolation point for a transformation from a plastic to an elastic state. To establish a quantitative description of the

elastic modulus during hydration, percolation theory based on the hardcore/soft-shell model was employed [151]. The regression results by using the equations (6) and (7) in paper VII within a certain time interval indicate the initial setting of concrete. The transition from a semi-solid to a solid state can be indexed by the inflection point of the average growth rate of formation factor (*a-F*). The *a-F* is calculated by dividing the formation factor by hydration time [59]. The inflection time of average growth rate of UPV (*a-UPV*) was determined using the same protocol.

Table 6.1 summarises the critical time and setting time of all the concrete samples, and Figure 6.4 shows the correlation between critical time and setting time. The critical time of *a-F* is a good indicator of both the initial and final setting, with a strong linear correlation, regardless of the influence of temperature. The inflection time of UPV can also indicate the final setting time in a similar way but it has a weaker correlation to the initial setting time.

Table 6.1. Critical time of *a-F* and *a-UPV* in percolation ($t_0$), the inflection time and setting time.

| Sample | Critical time [h] | | | | Setting time [h] | |
|---|---|---|---|---|---|---|
| | $t_0$ of UPV | $t_0$ of *F* | Peak of *a-UPV* | Inflection time of *a-F* | Initial setting | Final setting |
| C145 | 2.80 | 2.68 | 7.00 | 8.48 | 3.81 | 6.82 |
| C245 | 1.80 | 4.08 | 5.67 | 7.33 | 4.83 | 6.56 |
| C255 | 2.40 | 2.41 | 7.25 | 8.58 | 3.73 | 6.97 |
| C338 | 2.34 | 3.56 | 6.64 | 7.72 | 4.41 | 6.31 |

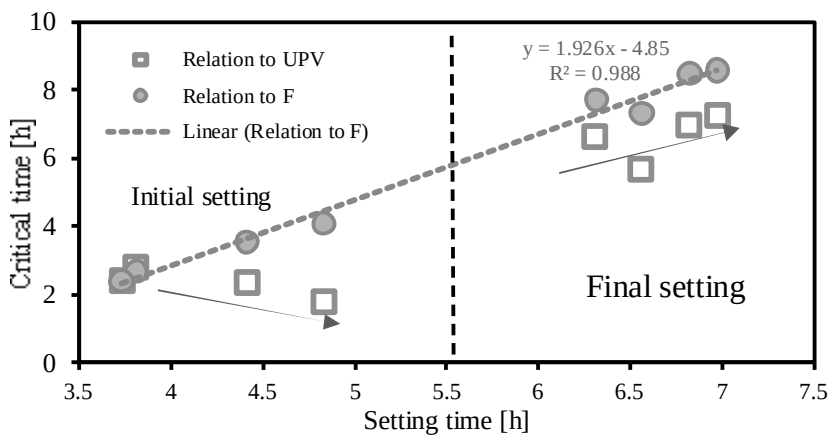


Figure 6.4. Correlation between critical time of monitored data and setting time of concrete: corresponding to *Figure 10* in paper VII.

### 6.3.2 Compressive strength

The mechanical properties of porous materials depend on the pore structures of the matrix. Several empirical functions have been proposed to describe the relationship between porosity and compressive strength of concrete [152,153]. Schiller [154] reported a logarithmic function as a typical expression. Formation factor relates to water accessible porosity according to Archie's law [87]. By combining Archie's law and Schiller's empirically function, Eq. (6.2) is obtained to describe the correlation between compressive strength and formation factor.

$$f_c = K\left(ln\Phi_0 - \frac{lna}{m}\right) + \frac{K}{m}lnF \quad (6.2)$$

where $f_c$ is the compressive strength, $K$ is the constant parameter, and $\Phi_0$ is porosity at which the strength practically vanishes. Parameters $a$ and $m$ share the same definition in Eq. (3.5). This equation describes the volume of pores filled with conductive liquid, so it may exclude the empty pores and air void in the non-saturated concrete matrix. However, the samples in this study cured under sealed condition so the matrix is a naturally saturated state with few empty air voids. In practical utilization, the saturation degree of the matrix should be taken into consideration.

Consequently, a logarithmic function was used as the base for regression between strength and $F$. Figure 6.5a depicts a linear relationship between the compressive strength of concretes containing SCMs and natural logarithm of the formation factor ln$F$, with a coefficient of determination ($R^2$) of 0.99. This finding is a remarkable quantitative description that can be used for in-situ monitoring of strength development of the blended concretes. Moreover, it is independent of both curing ages and binder types. On the other hand, Figure 6.5b displays the correlation between compressive strength and electrical conductivity of concretes. Although the $R^2$ value is high at 0.96, Figure 6.5d illustrates that the deviation in value predicted by electrical conductivity is significantly higher than that by $F$. This is mainly because ion concentration of pore solution affects the electrical conductivity of concretes.

For a theoretical description using physical principles, Luping [155] introduced a model based on Griffith's theory, which includes the average pore radii to describe the relationship between compressive strength and pore structure. Kumar and Bhattacharjee [156] furtherly simplified the correlation. This study used the simplified function and the Archie's law to build a correlation between compressive strength and formation factor as Eq. (6.3). $C_1$ and $C_2$ are constant parameters. The detailed derivation of this equation has been elaborated in paper VII.

$$f_c = \frac{C1 - C_2 F^{\frac{1}{m}}}{\sqrt{F^{-\frac{1}{m}}}} \quad (6.3)$$

Figure 6.5c shows the correlation between $F^{-1/m}$ ($m = 2$) and compressive strength is quite good with a regression result of $R^2$=0.99. Hence, the compressive strength can be well indicated by the formation factor in both the empirical and theoretical description.

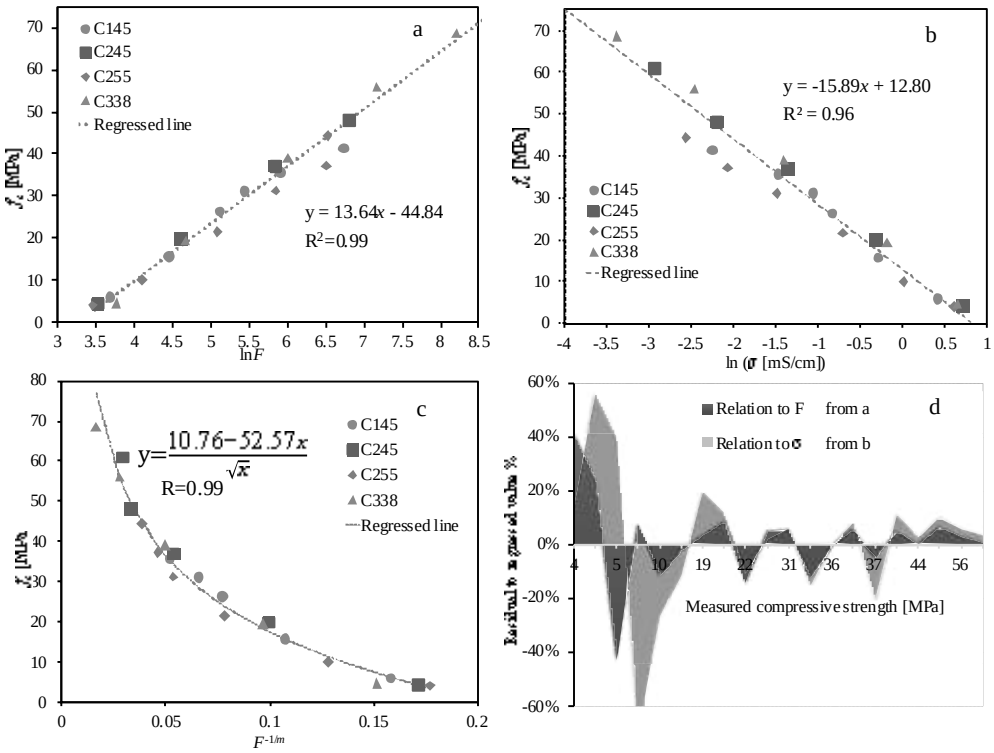


Figure 6.5. Quantitative correlations between compressive strength and electrical properties in different functions, corresponding to *Figure 13* in paper VII.

To highlight advantage of using formation factor, Figure 6.6 displays the regressions between compressive strength and ultrasonic pulse velocity (UPV). Numerous empirical relationships for correlating value of UPV ($v$) and compressive strength have been documented in a review paper [157]. The results in this study can be regressed with an exponential expression as Eq. (6.4).

$$f_c = A \cdot e^{B \cdot v} \tag{6.4}$$

where $A$ and $B$ are constant parameters related to the concrete mix. Despite with $R^2$ of 0.96, there is a significant deviation of data points from the regression line in the case of C145 and C255.

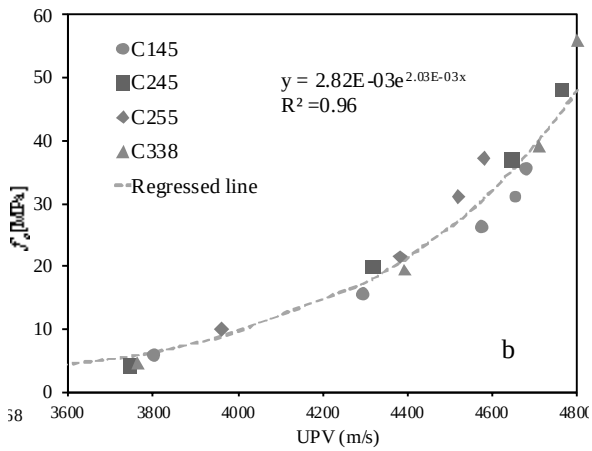


Figure 6.6. Quantitative correlations between compressive strength and UPV: *Figure 13* in paper VII.

## 6.4 Chapter summary

The upgraded device can properly measure the electrical conductivity of hydrating concretes with SCMs at various depths, meanwhile accounting for the dimension factor. Moreover, the temperature sensors integrated within the device provide test of the internal temperature with adequate accuracy at different depths, which is also useful for normalizing the electrical conductivity to a reference temperature.

Both the formation factor and UPV serve as good indicators for the hardening process of concrete up to final setting. The development of UPV and formation factor undergoes a sudden change during the hardening process, which can be explained by the percolation theory. The inflection time of formation factor shows a linear correlation with the initial and final setting time of concrete. Although all indices (including electrical conductivity, formation factor and UPV) can indicate the development of compressive strength in concretes, the formation factor is the most reliable indicator as it appears to be independent of binder types, mixing proportions, and curing ages. Quantitative descriptions have been established for the compressive strength in relation to all the indices, among which two correlations between compressive strength and formation factor exhibit the highest accuracy.

# 7 Conclusions and future research work

## 7.1 Conclusions

Supplementary cementitious materials (SCMs) are one of the promising options to reduce the emissions from production of cement and concrete. Most of them have a lower reactivity than cement clinker, so activators are commonly added to mitigate this issue. Both the SCMs and activators alter the hydration of the blended binders, change the microstructure of hardened cementitious materials, and thus impact the transport process related to the durability. Water plays a crucial role in the hydration reaction, in the microstructure of hydration products and in the deterioration process of cement-based materials. This study has revealed the limitations of dissolution theory and based on this, proposed a new hypothesis to explain the mechanism in early hydration of $C_3S$. A novel non-destructive method was developed to detect the microstructure change during the setting and hardening process. A new approach for assessing the hydration degree of SCMs has been proposed by use of thermodynamic simulations and water vapour isotherm. The proposed moisture transport testing method enables an effective detection of steady-state and transient moisture transport coefficients. The key structural parameters for moisture and ion transport in cementitious materials have been identified, and a simplified model has been proposed for an accurate prediction of chloride migration coefficient in the blended cementitious systems.

Hydration of $C_3S$ at early age is not solely controlled by the dissolution rate of minerals. The duration of the induction period is mainly determined by the nucleation rate of hydration products in localized areas on the surface. The new hypothesis proposed in this study is focused on the crystallization and precipitation process of the main hydration products, which provides a better explanation of early hydration mechanism. it suggests that C-S-H primarily nucleates within the near-surface region and its precipitation involves a nonclassical nucleation process. Additionally, the effect of potassium salts and pH levels on the dissolution of $C_3S$ and

precipitation of C-S-H can be well explained by the proposed hypothesis.

The process of water interacting with cement and SCMs is more complex than it with $C_3S$, so a non-destructive method was proposed to monitor early-age interactions based on electrical conductivity test. The evolution of electrical conductivity in hydrating pastes closely relates to chemical reaction and can be classified into four stages. The formation factor, calculated by dividing the pore solution conductivity by the paste conductivity, accurately reflects the evolution of pore structure during the hydration process. The differences in formation factors observed among various cementitious systems primarily derive from disparities in the pore solution connectivity. Blending SCMs refines the pore structure, better indexed by the decreased pore connectivity, which results in a much higher formation factor of hcp. Conductivity monitoring demonstrates the relationship between evaporable water volume and formation factor, facilitating in-situ monitoring of moisture content in cement-based materials.

SCMs not only impact the pore structure but also change the phase assemblage and the water structure in the local environment of C-S-H. Water vapour desorption isotherm is an effective test for detecting the mesoscale pore structure in pastes with SCMs. When calculating pore size distribution using the BJH model, it is important to consider the effect of ions on water vapour equilibrium pressure on a plane surface. The proposed novel approach performs well to evaluate the hydration degree of SCMs based on water vapour sorption and thermodynamic modelling. Cavitation during desorption results in an overestimation of small gel pore volume, but it somehow implies the refinement effect of SCMs on pore structure. Replacing CEM I with slag and fly ash increases both small and large gel pore volumes.

Interaction of water with hcp under low temperature can be effectively unraveled by Thermoporometry for characterising moisture distribution and broadband dielectric spectroscopy for detecting water dynamics. The melting curve performs better than the freezing curve for testing water confined in pores larger than 2.4–2.7 nm. Water in smaller pores, including interlayer and a part of gel pores, cannot form a tetrahedral ice structure during the cooling process. SCMs affect not only moisture distribution equilibrium at 97 % RH but also influence moisture redistribution during a drying down to 33 % RH. Despite controversies in previous publications on pore structure changes during the first drying, this study confirms that the drying process does not induce any increase in volume of unfrozen water (< ~2.4 nm) under equilibrium conditions. Gel pores coarsen severely during the drying between 75 % and 55 % RH. SCMs have limited effects on the dynamics of structural water, and they primarily influence dynamics of water in small gel pores and the interfacial polarization.

SCMs have a significant impact on the pore structure, thus altering moisture and chloride transport in cement-based materials. The reduction in moisture transport coefficient and

chloride migration coefficient caused by SCMs is more pronounced at a higher *w/b* and after a longer curing. Pore structure refinement, specifically the reduction in pore connectivity, is the primary reason for the decrease in moisture transport coefficient of blended systems. The moisture transport properties in hcp are determined by both the formation factor and the porosity of small pores, with the formation factor being the primary factor at high RH and the porosity of small pores being the primary factor at low RH. The effect of SCMs on chloride resistance also mainly derives from the refinement of pore structure, which depends on the *w/b* and curing ages. A simplified model based on the formation factor can be used to estimate the chloride migration coefficient of hcp and mortars.

A reliable non-destructive monitoring method is useful for promoting the use of SCMs in concrete. The upgraded device properly measures the electrical conductivity and internal temperature of hydrating concretes with SCMs. Both formation factor and UPV are good indicators for the hardening process of concrete. The formation factor is the most reliable indicator for compressive strength development and is independent of SCMs types, mixing proportions, and curing ages. Quantitative descriptions have been established for the compressive strength in relation to the monitored indices, and Correlations between compressive strength and formation factor exhibit the best prediction

## 7.2 Future research work

Hydration during the main peak controls the setting and hardening of cement-based materials. This study paid more attention to early hydration up to the end of induction period, but a concept model has been proposed for understanding the hydration of $C_3S$ after the induction period. It is of great interest to further develop an analytic model based on the conceptual model to provide a quantitative description for the precipitation of hydration products at the main peak.

The electrical conductivity test has been verified as a very effective method to monitor the moisture related interaction process in SCMs at relative early age. The main purpose of the project is to develop a method for assessing the moisture drying in the blended concrete. Therefore, a clear correlation between the moisture content and electrical conductivity in concrete is meaningful topic in further research. Chloride ingress, carbonation and the combined effects will also change both the moisture and ion concentration in concrete. Exploring the function of the device for monitoring these processes in low-carbon concretes is very interesting as well.

The refinement effect of SCMs on the pore structure and its impact on moisture and ion transport depend on the later age hydration. Thus, it is essential to conduct further research on the effect of curing conditions on the pore structure and spatial distribution of hydration products. This can be achieved by combining different advanced tests to reveal differences in phase assemblage and local pore distribution in hcp after different long-term curing regimes. Such studies not only enhance our understanding of the impact of SCMs on the durability of concrete but also contribute to a deeper comprehension of the mechanisms governing hydration at later stages.

Experimental results from this study provide abundant data for validation of models that predicts moisture transport based on pore size distribution or pore network in blended pastes. Another topic for future research is the development of a moisture transport and fixation model based on pore structure. Models that incorporate the effect of the interfacial transition zone are also necessary to predict moisture content and diffusion in concrete containing various kinds of SCMs.

# References


[1] P.A. Arias, N. Bellouin, E. Coppola, R.G. Jones, K. Zickfeld, IPCC AR6 WGI Technical Summary, Cambridge University Press, Cambridge, UK and New York, NY, USA, 2021.

[2] F. Preston, J. Lehne, Making Concrete Change Innovation in Low-carbon Cement and Concrete, CHATHAM HOUSE, 2018.

[3] IEA, Energy technology perspectives 2023, IEA—International Energy Agency Paris, France, 2023. https://www.iea.org/reports/energy-technology-perspectives-2023.

[4] IEA, Low-carbon Transition in the Cement Industry: Technology Roadmap, IEA—International Energy Agency Paris, France, 2019. https://webstore.iea.org/technology-roadmap-low-carbontransition-in-the-cement-industry. (accessed October 5, 2019).

[5] Davis, Steven J., Nathan S. Lewis, Matthew Shaner, Sonia Aggarwal, Doug Arent, Inês L. Azevedo, Sally M. Benson et al. Net-zero emissions energy systems, Science. 360 (2018) eaas9793. https://doi.org/10.1126/science.aas9793.

[6] R.M. Andrew, Global $CO_2$ emissions from cement production, Earth Syst Sci Data. 10 (2018) 195–217. https://doi.org/10.5194/essd-10-195-2018.

[7] IEA, World Energy Outlook 2022, IEA—International Energy Agency Paris, France, 2022. https://www.iea.org/reports/world-energy-outlook-2022.

[8] P.J.M. Monteiro, S.A. Miller, A. Horvath, Towards sustainable concrete, Nat. Mater. 16 (2017) 698–699. https://doi.org/10.1038/nmat4930.

[9] K.L. Scrivener, P. Juilland, P.J.M. Monteiro, Advances in understanding hydration of Portland cement, Cem. Concr. Res. 78 (2015) 38–56. https://doi.org/10.1016/j.cemconres.2015.05.025.

[10] K.L. Scrivener, A. Ouzia, P. Juilland, A. K. Mohamed, Advances in understanding cement hydration mechanisms, Cement and Concrete Research 124 (2019): 105823.

[11] J.I. Escalante-García, J.H. Sharp, Effect of temperature on the hydration of the main clinker phases in portland cements: part II, blended cements, Cem. Concr. Res. 28 (1998) 1259–1274. https://doi.org/10.1016/S0008-8846(98)00107-0.

[12] P. Juilland, L. Nicoleau, R.S. Arvidson, E. Gallucci, Advances in dissolution understanding and their implications for cement hydration, RILEM Tech. Lett. 2 (2017) 90–98. https://doi.org/10.21809/rilemtechlett.2017.47.

[13] C. Naber, F. Bellmann, T. Sowoidnich, F. Goetz-Neunhoeffer, J. Neubauer, Alite dissolution and C-S-H precipitation rates during hydration, Cem. Concr. Res. 115 (2019) 283–293. https://doi.org/10.1016/j.cemconres.2018.09.001.

[14] L. Nicoleau, E. Schreiner, A. Nonat, Ion-specific effects influencing the dissolution of tricalcium silicate, Cem. Concr. Res. 59 (2014) 118–138. https://doi.org/10.1016/j.cemconres.2014.02.006.

[15] F. Bellmann, T. Sowoidnich, H.-M. Ludwig, D. Damidot, Dissolution rates during the early hydration of tricalcium silicate, Cem. Concr. Res. 72 (2015) 108–116. https://doi.org/10.1016/j.cemconres.2015.02.002.

[16] L. Nicoleau, A. Nonat, D. Perrey, The di- and tricalcium silicate dissolutions, Cem. Concr. Res. 47 (2013) 14–30. https://doi.org/10.1016/j.cemconres.2013.01.017.

[17] A. Schöler, B. Lothenbach, F. Winnefeld, M.B. Haha, M. Zajac, H.-M. Ludwig, Early hydration of SCM-blended Portland cements: A pore solution and isothermal calorimetry study, Cem. Concr. Res. 93 (2017) 71–82. https://doi.org/10.1016/j.cemconres.2016.11.013.

[18] J. Skibsted, R. Snellings, Reactivity of supplementary cementitious materials (SCMs) in cement blends, Cem. Concr. Res. 124 (2019) 105799. https://doi.org/10.1016/j.cemconres.2019.105799.

[19] S. Joseph, R. Snellings, Ö. Cizer, Activation of Portland cement blended with high volume of fly ash using $Na_2SO_4$, Cem. Concr. Compos. 104 (2019) 103417.

[20] A.M. Rashad, Y. Bai, P.A.M. Basheer, N.B. Milestone, N.C. Collier, Hydration and properties of sodium sulfate activated slag, Cem. Concr. Compos. 37 (2013) 20–29.

https://doi.org/10.1016/j.cemconcomp.2012.12.010.

[21] L. Huang, W. Song, H. Li, H. Zhang, Z. Yang, Effects of aphthitalite on the formation of clinker minerals and hydration properties, Constr. Build. Mater. 183 (2018) 275–282.

[22] L. Huang, Z. Yang, Early hydration of tricalcium silicate with potassium hydroxide and sulfate from pore solution and solid view, Constr. Build. Mater. 230 (2020) 116988.

[23] I. Jawed, J. Skalny, Alkalies in cement: A review, Cem. Concr. Res. 8 (1978) 37–51. https://doi.org/10.1016/0008-8846(78)90056-X.

[24] S. Adu-Amankwah, M. Zajac, C. Stabler, B. Lothenbach, L. Black, Influence of limestone on the hydration of ternary slag cements, Cem. Concr. Res. 100 (2017) 96–109. https://doi.org/10.1016/j.cemconres.2017.05.013.

[25] B. Mota, T. Matschei, K. Scrivener, The influence of sodium salts and gypsum on alite hydration, Cem. Concr. Res. 75 (2015) 53–65.

[26] P.K. Mehta, P.J. Monteiro, Concrete: microstructure, properties, and materials, McGraw-Hill Education, 2014.

[27] V. Baroghel-Bouny, M. Thiéry, X. Wang, Modelling of isothermal coupled moisture–ion transport in cementitious materials, Cem. Concr. Res. 41 (2011) 828–841. https://doi.org/10.1016/j.cemconres.2011.04.001.

[28] L. Huang, L. Tang, I. Löfgren, N. Olsson, Z. Yang, Y. Li, Moisture and ion transport properties in blended pastes and their relation to the refined pore structure, Cem. Concr. Res. 161 (2022) 106949. https://doi.org/10.1016/j.cemconres.2022.106949.

[29] S. Ahmad, Reinforcement corrosion in concrete structures, its monitoring and service life prediction—a review, Cem. Concr. Compos. 25 (2003) 459–471.

[30] P.J. Prado, B.J. Balcom, S.D. Beyea, T.W. Bremner, R.L. Armstrong, P.E. Grattan-Bellew, Concrete Freeze/Thaw as Studied by Magnetic Resonance Imaging, Cem. Concr. Res. 28 (1998) 261–270. https://doi.org/10.1016/S0008-8846(97)00222-6.

[31] Z.P. Bazant, J.-C. Chern, A.M. Rosenberg, J.M. Gaidis, Mathematical Model for Freeze-Thaw Durability of Concrete, J. Am. Ceram. Soc. 71 (1988) 776–783. https://doi.org/10.1111/j.1151-2916.1988.tb06413.x.

[32] F. Rajabipour, E. Giannini, C. Dunant, J.H. Ideker, M.D.A. Thomas, Alkali–silica reaction: Current understanding of the reaction mechanisms and the knowledge gaps, Cem. Concr. Res. 76 (2015) 130–146. https://doi.org/10.1016/j.cemconres.2015.05.024.

[33] T. Luping, J. Gulikers, On the mathematics of time-dependent apparent chloride diffusion coefficient in concrete, Cem. Concr. Res. 37 (2007) 589–595. https://doi.org/10.1016/j.cemconres.2007.01.006.

[34] V. Elfmarkova, P. Spiesz, H.J.H. Brouwers, Determination of the chloride diffusion coefficient in blended cement mortars, Cem. Concr. Res. 78 (2015) 190–199. https://doi.org/10.1016/j.cemconres.2015.06.014.

[35] M. Shafikhani, S.E. Chidiac, A holistic model for cement paste and concrete chloride diffusion coefficient, Cem. Concr. Res. 133 (2020) 106049. https://doi.org/10.1016/j.cemconres.2020.106049.

[36] N. Olsson, F. Abdul Wahid, L.-O. Nilsson, C. Thiel, H.S. Wong, V. Baroghel-Bouny, Wick action in mature mortars with binary cements containing slag or silica fume – The relation between chloride and moisture transport properties under non-saturated conditions, Cem. Concr. Res. 111 (2018) 94–103. https://doi.org/10.1016/j.cemconres.2018.06.006.

[37] V. Baroghel-Bouny, Water vapour sorption experiments on hardened cementitious materials. Part II: Essential tool for assessment of transport properties and for durability prediction, Cem. Concr. Res. 37 (2007) 438–454. https://doi.org/10.1016/j.cemconres.2006.11.017.

[38] M. Saeidpour, L. Wadsö, Moisture diffusion coefficients of mortars in absorption and desorption, Cem. Concr. Res. 83 (2016) 179–187. https://doi.org/10.1016/j.cemconres.2016.02.003.

[39] N. Olsson, L.-O. Nilsson, M. Åhs, V. Baroghel-Bouny, Moisture transport and sorption in cement based materials containing slag or silica fume, Cem. Concr. Res. 106 (2018) 23–32. https://doi.org/10.1016/j.cemconres.2018.01.018.

[40] O. Linderoth, Hydration, pore structure, and related moisture properties of fly ash blended cement-based materials: Experimental methods and laboratory measurements, PhD thesis, Lund University, 2020.

[41] N. Olsson, B. Lothenbach, V. Baroghel-Bouny, L.-O. Nilsson, Unsaturated ion diffusion in cementitious materials – The effect of slag and silica fume, Cem. Concr. Res. 108 (2018) 31–37. https://doi.org/10.1016/j.cemconres.2018.03.007.

[42] L. Tang, D. Boubitsas, L. Huang, Long-term performance of reinforced concrete under a de-icing road environment, Cem. Concr. Res. 164 (2023) 107039. https://doi.org/10.1016/j.cemconres.2022.107039.

[43] J. Plank, E. Sakai, C.W. Miao, C. Yu, J.X. Hong, Chemical admixtures — Chemistry, applications and their impact on concrete microstructure and durability, Cem. Concr. Res. 78 (2015) 81–99. https://doi.org/10.1016/j.cemconres.2015.05.016.

[44] L. Huang, L. Tang, L. Wadsö, I. Löfgren, N. Olsson, Z. Yang, Using water vapour and N2 isotherms to unveil effects of SCMs on nanopores and evaluate hydration degree, Cem. Concr. Res. 164 (2023) 107042. https://doi.org/10.1016/j.cemconres.2022.107042.

[45] E. Berodier, K. Scrivener, Evolution of pore structure in blended systems, Cem. Concr. Res. 73 (2015) 25–35.

[46] P. Duan, Z. Shui, W. Chen, C. Shen, Effects of metakaolin, silica fume and slag on pore structure, interfacial transition zone and compressive strength of concrete, Constr. Build. Mater. 44 (2013) 1–6.

[47] V.Z. Zadeh, C.P. Bobko, Nanoscale mechanical properties of concrete containing blast furnace slag and fly ash before and after thermal damage, Cem. Concr. Compos. 37 (2013) 215–221.

[48] C. Hu, Z. Li, Property investigation of individual phases in cementitious composites containing silica fume and fly ash, Cem. Concr. Compos. 57 (2015) 17–26.

[49] W. Wilson, L. Sorelli, A. Tagnit-Hamou, Unveiling micro-chemo-mechanical properties of C–(A)–S–H and other phases in blended-cement pastes, Cem. Concr. Res. 107 (2018) 317–336.

[50] S. Cerveny, F. Mallamace, J. Swenson, M. Vogel, L. Xu, Confined Water as Model of Supercooled Water, Chem Rev. (2016) 18.

[51] R. Bergman, J. Swenson, Dynamics of supercooled water in confined geometry, Nature. 403 (2000) 283–286.

[52] J. Swenson, Possible relations between supercooled and glassy confined water and amorphous bulk ice, Phys. Chem. Chem. Phys. 20 (2018) 30095–30103. https://doi.org/10.1039/C8CP05688A.

[53] O. Coussy, P.J.M. Monteiro, Poroelastic model for concrete exposed to freezing temperatures, Cem. Concr. Res. 38 (2008) 40–48. https://doi.org/10.1016/j.cemconres.2007.06.006.

[54] L. Reiter, T. Wangler, A. Anton, R.J. Flatt, Setting on demand for digital concrete – Principles, measurements, chemistry, validation, Cem. Concr. Res. 132 (2020) 106047. https://doi.org/10.1016/j.cemconres.2020.106047.

[55] V. Mechtcherine, K. van Tittelboom, A. Kazemian, E. Kreiger, B. Nematollahi, V.N. Nerella, M. Santhanam, G. de Schutter, G. Van Zijl, D. Lowke, E. Ivaniuk, M. Taubert, F. Bos, A roadmap for quality control of hardening and hardened printed concrete, Cem. Concr. Res. 157 (2022) 106800. https://doi.org/10.1016/j.cemconres.2022.106800.

[56] H.W. Reinhardt, ed., Testing during concrete construction: proceedings of the international workshop held by RILEM and organized by the Institut für Massivbau, Chapman and Hall, Technical University of Darmstadt, Germany, Mainz, March 5–7, 1990.

[57] L. Huang, Z. Yang, Hydration kinetics of tricalcium silicate with the presence of portlandite and calcium silicate hydrate, Thermochim. Acta. 681 (2019) 178398. https://doi.org/10.1016/j.tca.2019.178398.

[58] L. Huang, Water and alkali salts in the hydrating and hardened green cement-based materials: Hydration process, moisture content and transport, Licentiate thesis, Chalmers Tekniska Hogskola (Sweden), 2022.

[59] L. Huang, L. Tang, I. Löfgren, N. Olsson, Z. Yang, Real-time monitoring the electrical properties of pastes to map the hydration induced microstructure change in cement-based materials, Cem. Concr. Compos. 132 (2022) 104639. https://doi.org/10.1016/j.cemconcomp.2022.104639.

[60] B. Sioulas, J.G. Sanjayan, The coloration phenomenon associated with slag blended cements, Cem. Concr. Res. 31 (2001) 313–320. https://doi.org/10.1016/S0008-8846(00)00371-9.

[61] J.D. Rhoades, P.A.C. Raats, R.J. Prather, Effects of liquid-phase electrical conductivity, water content, and surface conductivity on bulk soil electrical conductivity, Soil Sci. Soc. Am. J. 40 (1976) 651–655.

https://doi.org/10.2136/sssaj1976.03615995004000050017x.

[62] S.-T. Yi, E.-I. Yang, J.-C. Choi, Effect of specimen sizes, specimen shapes, and placement directions on compressive strength of concrete, Nucl. Eng. Des. 236 (2006) 115–127. https://doi.org/10.1016/j.nucengdes.2005.08.004.

[63] B. Lothenbach, D.A. Kulik, T. Matschei, M. Balonis, L. Baquerizo, B. Dilnesa, G.D. Miron, R.J. Myers, Cemdata18: A chemical thermodynamic database for hydrated Portland cements and alkali-activated materials, Cem. Concr. Res. 115 (2019) 472–506. https://doi.org/10.1016/j.cemconres.2018.04.018.

[64] T. Thoenen, W. Hummel, U. Berner, E. Curti, The PSI/Nagra Chemical Thermodynamic Database 12/07, (2014).

[65] J.I. Escalante-García, J.H. Sharp, Effect of temperature on the hydration of the main clinker phases in portland cements: part i, neat cements, Cem. Concr. Res. 28 (1998) 1245–1257. https://doi.org/10.1016/S0008-8846(98)00115-X.

[66] J. Bensted, Hydration of Portland Cement, in: Adv. Cem. Technol., Elsevier, 1983: pp. 307–347. https://doi.org/10.1016/B978-0-08-028670-9.50015-6.

[67] H.M. Jennings, P.L. Pratt, An experimental argument for the existence of a protective membrane surrounding portland cement during the induction period, Cem. Concr. Res. 9 (1979) 501–506. https://doi.org/10.1016/0008-8846(79)90048-6.

[68] L. Huang, L. Tang, H. Gu, Z. Li, Z. Yang, New insights into the reaction of tricalcium silicate ($C_3S$) with solutions to the end of the induction period, Cem. Concr. Res. 152 (2022) 106688. https://doi.org/10.1016/j.cemconres.2021.106688.

[69] P.W. Brown, E. Franz, G. Frohnsdorff, H.F.W. Taylor, Analyses of the aqueous phase during early $C_3S$ hydration, Cem. Concr. Res. 14 (1984) 257–262. https://doi.org/10.1016/0008-8846(84)90112-1.

[70] E.M. Gartner, F.J. Tang, S.J. Weiss, Saturation Factors for Calcium Hydroxide and Calcium Sulfates in Fresh Portland Cement Pastes, J. Am. Ceram. Soc. 68 (1985) 667–673. https://doi.org/10.1111/j.1151-2916.1985.tb10122.x.

[71] J. Nehring, D. Jansen, J. Neubauer, F. Goetz-Neunhoeffer, Hydration of $C_3S$ in presence of CA : Mineral-pore solution interaction, J. Am. Ceram. Soc. 102 (2019) 3152–3162. https://doi.org/10.1111/jace.16197.

[72] P. Suraneni, R.J. Flatt, Micro-reactors to Study Alite Hydration, J. Am. Ceram. Soc. 98 (2015) 1634–1641. https://doi.org/10.1111/jace.13472.

[73] P. Suraneni, R.J. Flatt, Use of micro-reactors to obtain new insights into the factors influencing tricalcium silicate dissolution, Cem. Concr. Res. 78 (2015) 208–215. https://doi.org/10.1016/j.cemconres.2015.07.011.

[74] E. Pustovgar, R.K. Mishra, M. Palacios, J.-B. d'Espinose de Lacaillerie, T. Matschei, A.S. Andreev, H. Heinz, R. Verel, R.J. Flatt, Influence of aluminates on the hydration kinetics of tricalcium silicate, Cem. Concr. Res. 100 (2017) 245–262. https://doi.org/10.1016/j.cemconres.2017.06.006.

[75] F. Bellmann, H.-M. Ludwig, Analysis of aluminum concentrations in the pore solution during hydration of tricalcium silicate, Cem. Concr. Res. 95 (2017) 84–94. https://doi.org/10.1016/j.cemconres.2017.02.020.

[76] A. Ouzia, K. Scrivener, The needle model: A new model for the main hydration peak of alite, Cem. Concr. Res. 115 (2019) 339–360. https://doi.org/10.1016/j.cemconres.2018.08.005.

[77] J.J. De Yoreo, P.U.P.A. Gilbert, N.A.J.M. Sommerdijk, R.L. Penn, S. Whitelam, D. Joester, H. Zhang, J.D. Rimer, A. Navrotsky, J.F. Banfield, A.F. Wallace, F.M. Michel, F.C. Meldrum, H. Colfen, P.M. Dove, Crystallization by particle attachment in synthetic, biogenic, and geologic environments, Science. 349 (2015) aaa6760–aaa6760. https://doi.org/10.1126/science.aaa6760.

[78] G. Mirabello, A. Ianiro, P.H.H. Bomans, T. Yoda, A. Arakaki, H. Friedrich, G. de With, N.A.J.M. Sommerdijk, Crystallization by particle attachment is a colloidal assembly process, Nat. Mater. 19 (2020) 391–396. https://doi.org/10.1038/s41563-019-0511-4.

[79] N. Krautwurst, L. Nicoleau, M. Dietzsch, I. Lieberwirth, C. Labbez, A. Fernandez-Martinez, A.E.S. Van Driessche, B. Barton, S. Leukel, W. Tremel, Two-step nucleation process of calcium silicate hydrate, the nanobrick of cement, Chem. Mater. 30 (2018) 2895–2904. https://doi.org/10.1021/acs.chemmater.7b04245.

[80] F. Bellmann, D. Damidot, B. Möser, J. Skibsted, Improved evidence for the existence of an intermediate phase during hydration of tricalcium silicate, Cem. Concr. Res. 40 (2010) 875–884. https://doi.org/10.1016/j.cemconres.2010.02.007.

[81] C. Nalet, A. Nonat, Retarding effectiveness of hexitols on the hydration of the silicate phases of cement: Interaction with the aluminate and sulfate phases, Cem. Concr. Res. 90 (2016) 137–143. https://doi.org/10.1016/j.cemconres.2016.09.018.

[82] M. Schönlein, J. Plank, A TEM study on the very early crystallization of C-S-H in the presence of polycarboxylate superplasticizers: Transformation from initial C-S-H globules to nanofoils, Cem. Concr. Res. 106 (2018) 33–39. https://doi.org/10.1016/j.cemconres.2018.01.017.

[83] F. Rajabipour, J. Weiss, Electrical conductivity of drying cement paste, Mater. Struct. 40 (2007) 1143–1160. https://doi.org/10.1617/s11527-006-9211-z.

[84] J. Bockris, Modern Electrochemistry: An Introduction to an Interdisciplinary Area Volume 1, Springer Science & Business Media, 2012.

[85] F. Deschner, F. Winnefeld, B. Lothenbach, S. Seufert, P. Schwesig, S. Dittrich, F. Goetz-Neunhoeffer, J. Neubauer, Hydration of Portland cement with high replacement by siliceous fly ash, Cem. Concr. Res. 42 (2012) 1389–1400. https://doi.org/10.1016/j.cemconres.2012.06.009.

[86] A. Vollpracht, B. Lothenbach, R. Snellings, J. Haufe, The pore solution of blended cements: a review, Mater. Struct. 49 (2016) 3341–3367. https://doi.org/10.1617/s11527-015-0724-1.

[87] G.E. Archie, The Electrical Resistivity Log as an Aid in Determining Some Reservoir Characteristics, Trans. AIME. 146 (1942) 54–62. https://doi.org/10.2118/942054-G.

[88] P.J. Tumidajski, A.S. Schumacher, S. Perron, P. Gu, J.J. Beaudoin, On the relationship between porosity and electrical resistivity in cementitious systems, Cem. Concr. Res. 26 (1996) 539–544. https://doi.org/10.1016/0008-8846(96)00017-8.

[89] M.K. Moradllo, Relating Formation Factor of Concrete to Water Absorption, ACI Mater. J. (2018) 13.

[90] E.J. Garboczi, Permeability, diffusivity, and microstructural parameters: A critical review, Cem. Concr. Res. 20 (1990) 591–601. https://doi.org/10.1016/0008-8846(90)90101-3.

[91] J. Zhang, E.A. Weissinger, S. Peethamparan, G.W. Scherer, Early hydration and setting of oil well cement, Cem. Concr. Res. 40 (2010) 1023–1033. https://doi.org/10.1016/j.cemconres.2010.03.014.

[92] J.P. Straley, Critical phenomena in resistor networks, J. Phys. C Solid State Phys. 9 (1976) 783–795. https://doi.org/10.1088/0022-3719/9/5/017.

[93] I. Webman, J. Jortner, M.H. Cohen, Numerical simulation of continuous percolation conductivity, Phys. Rev. B. 14 (1976) 4737–4740. https://doi.org/10.1103/PhysRevB.14.4737.

[94] E.R.A. Jr, G.H. Smith, The Significance of Particle Shape in Formation Resistivity Factor-Porosity Relationships, J. Pet. Technol. (n.d.) 7.

[95] V. Baroghel-Bouny, Water vapour sorption experiments on hardened cementitious materials. Part II: Essential tool for assessment of transport properties and for durability prediction, Cem. Concr. Res. 37 (2007) 438–454. https://doi.org/10.1016/j.cemconres.2006.11.017.

[96] V. Baroghel-Bouny, Water vapour sorption experiments on hardened cementitious materials part I: Essential tool for analysis of hygral behaviour and its relation to pore structure, Cem. Concr. Res. 37 (2007) 414–437. https://doi.org/10.1016/j.cemconres.2006.11.019.

[97] H.M. Jennings, A. Kumar, G. Sant, Quantitative discrimination of the nano-pore-structure of cement paste during drying: New insights from water sorption isotherms, Cem. Concr. Res. 76 (2015) 27–36. https://doi.org/10.1016/j.cemconres.2015.05.006.

[98] M. Babaee, A. Castel, Water vapor sorption isotherms, pore structure, and moisture transport characteristics of alkali-activated and Portland cement-based binders, Cem. Concr. Res. 113 (2018) 99–120. https://doi.org/10.1016/j.cemconres.2018.07.006.

[99] N. De Belie, J. Kratky, S. Van Vlierberghe, Influence of pozzolans and slag on the microstructure of partially carbonated cement paste by means of water vapour and nitrogen sorption experiments and BET calculations, Cem. Concr. Res. 40 (2010) 1723–1733. https://doi.org/10.1016/j.cemconres.2010.08.014.

[100] E.P. Barrett, L.G. Joyner, P.P. Halenda, The determination of pore volume and area distributions in porous

substances. I. Computations from nitrogen isotherms, J. Am. Chem. Soc. 73 (1951) 373–380.

[101] I. Maruyama, J. Rymeš, M. Vandamme, B. Coasne, Cavitation of water in hardened cement paste under short-term desorption measurements, Mater. Struct. 51 (2018) 159. https://doi.org/10.1617/s11527-018-1285-x.

[102] M. Rastogi, A. Müller, M.B. Haha, K.L. Scrivener, The role of cavitation in drying cementitious materials, Cem. Concr. Res. 154 (2022) 106710. https://doi.org/10.1016/j.cemconres.2022.106710.

[103] J. Hagymassy Jr, S. Brunauer, R.S. Mikhail, Pore structure analysis by water vapor adsorption: I. t-curves for water vapor, J. Colloid Interface Sci. 29 (1969) 485–491.

[104] R. Badmann, N. Stockhausen, M.J. Setzer, The statistical thickness and the chemical potential of adsorbed water films, J. Colloid Interface Sci. 82 (1981) 534–542. https://doi.org/10.1016/0021-9797(81)90395-7.

[105] E.A. Guggenheim, The theoretical basis of Raoult's law, Trans. Faraday Soc. 33 (1937) 151. https://doi.org/10.1039/tf9373300151.

[106] H. Chen, M. Wyrzykowski, K. Scrivener, P. Lura, Prediction of self-desiccation in low water-to-cement ratio pastes based on pore structure evolution, Cem. Concr. Res. 49 (2013) 38–47. https://doi.org/10.1016/j.cemconres.2013.03.013.

[107] P.A. Bonnaud, Q. Ji, B. Coasne, R.J.-M. Pellenq, K.J. Van Vliet, Thermodynamics of Water Confined in Porous Calcium-Silicate-Hydrates, Langmuir. 28 (2012) 11422–11432. https://doi.org/10.1021/la301738p.

[108] R.J.-M. Pellenq, A. Kushima, R. Shahsavari, K.J. Van Vliet, M.J. Buehler, S. Yip, F.-J. Ulm, A realistic molecular model of cement hydrates, Proc. Natl. Acad. Sci. 106 (2009) 16102–16107. https://doi.org/10.1073/pnas.0902180106.

[109] G. Kovačević, B. Persson, L. Nicoleau, A. Nonat, V. Veryazov, Atomistic modeling of crystal structure of Ca 1.67 SiH x, Cem. Concr. Res. 67 (2015) 197–203. https://doi.org/10.1016/j.cemconres.2014.09.003.

[110] I.G. Richardson, Tobermorite/jennite- and tobermorite/calcium hydroxide-based models for the structure of C-S-H: applicability to hardened pastes of tricalcium silicate, β-dicalcium silicate, Portland cement, and blends of Portland cement with blast-furnace slag, metakaolin, or silica fume, Cem. Concr. Res. 34 (2004) 1733–1777. https://doi.org/10.1016/j.cemconres.2004.05.034.

[111] R.A. Olson, H.M. Jennings, Estimation of CSH content in a blended cement paste using water adsorption, Cem. Concr. Res. 31 (2001) 351–356.

[112] K.L. Scrivener, B. Lothenbach, N. De Belie, E. Gruyaert, J. Skibsted, R. Snellings, A. Vollpracht, TC 238-SCM: hydration and microstructure of concrete with SCMs, Mater. Struct. 48 (2015) 835–862.

[113] M.B. Haha, K. De Weerdt, B. Lothenbach, Quantification of the degree of reaction of fly ash, Cem. Concr. Res. 40 (2010) 1620–1629.

[114] V. Kocaba, E. Gallucci, K.L. Scrivener, Methods for determination of degree of reaction of slag in blended cement pastes, Cem. Concr. Res. 42 (2012) 511–525. https://doi.org/10.1016/j.cemconres.2011.11.010.

[115] C. Alba-Simionesco, B. Coasne, G. Dosseh, G. Dudziak, K.E. Gubbins, R. Radhakrishnan, M. Sliwinska-Bartkowiak, Effects of confinement on freezing and melting, J. Phys. Condens. Matter. 18 (2006) R15–R68. https://doi.org/10.1088/0953-8984/18/6/R01.

[116] H. Kanda, M. Miyahara, K. Higashitani, Solidification of Lennard-Jones Fluid in Cylindrical Nanopores and Its Geometrical Hindrance Effect: A Monte Carlo Study, Langmuir. 16 (2000) 8529–8535. https://doi.org/10.1021/la991659p.

[117] Z. Sun, G.W. Scherer, Pore size and shape in mortar by thermoporometry, Cem. Concr. Res. 40 (2010) 740–751. https://doi.org/10.1016/j.cemconres.2009.11.011.

[118] D.H. Bager, E.J. Sellevold, Ice formation in hardened cement paste, Part I — room temperature cured pastes with variable moisture contents, Cem. Concr. Res. 16 (1986) 709–720. https://doi.org/10.1016/0008-8846(86)90045-1.

[119] K. Kurumisawa, O.M. Jensen, Thermoporometry and Proton NMR Measurement on Cement Paste Equilibrated at Different Relative Humidities, J. Adv. Concr. Technol. 18 (2020) 456–462. https://doi.org/10.3151/jact.18.456.

[120] P.D. Svensson, S. Hansen, Freezing and thawing of montmorillonite — A time-resolved synchrotron X-ray diffraction study, Appl. Clay Sci. 49 (2010) 127–134. https://doi.org/10.1016/j.clay.2010.04.015.

[121] M. Brun, A. Lallemand, J.-F. Quinson, C. Eyraud, A new method for the simultaneous determination of the size and shape of pores: the thermoporometry, Thermochim. Acta. 21 (1977) 59–88.

[122] S. Jähnert, F. Vaca Chávez, G.E. Schaumann, A. Schreiber, M. Schönhoff, G.H. Findenegg, Melting and freezing of water in cylindrical silica nanopores, Phys. Chem. Chem. Phys. 10 (2008) 6039. https://doi.org/10.1039/b809438c.

[123] E.B. Moore, E. de la Llave, K. Welke, D.A. Scherlis, V. Molinero, Freezing, melting and structure of ice in a hydrophilic nanopore, Phys. Chem. Chem. Phys. 12 (2010) 4124. https://doi.org/10.1039/b919724a.

[124] H.M. Jennings, Refinements to colloid model of C-S-H in cement: CM-II, Cem. Concr. Res. 38 (2008) 275–289. https://doi.org/10.1016/j.cemconres.2007.10.006.

[125] A.C.A. Muller, K.L. Scrivener, A.M. Gajewicz, P.J. McDonald, Use of bench-top NMR to measure the density, composition and desorption isotherm of C–S–H in cement paste, Microporous Mesoporous Mater. 178 (2013) 99–103. https://doi.org/10.1016/j.micromeso.2013.01.032.

[126] A.C.A. Muller, K.L. Scrivener, A.M. Gajewicz, P.J. McDonald, Densification of C–S–H Measured by $^{1}$H NMR Relaxometry, J. Phys. Chem. C. 117 (2013) 403–412. https://doi.org/10.1021/jp3102964.

[127] V. Musumeci, G. Goracci, P. Sanz Camacho, J.S. Dolado, C. Aymonier, Correlation between the Dynamics of Nanoconfined Water and the Local Chemical Environment in Calcium Silicate Hydrate Nanominerals, Chem. – Eur. J. 27 (2021) 11309–11318. https://doi.org/10.1002/chem.202100098.

[128] S. Cerveny, G.A. Schwartz, J. Otegui, J. Colmenero, J. Loichen, S. Westermann, Dielectric Study of Hydration Water in Silica Nanoparticles, J. Phys. Chem. C. 116 (2012) 24340–24349. https://doi.org/10.1021/jp307826s.

[129] S. Cerveny, S. Arrese-Igor, J.S. Dolado, J.J. Gaitero, A. Alegría, J. Colmenero, Effect of hydration on the dielectric properties of C-S-H gel, J. Chem. Phys. 134 (2011) 034509. https://doi.org/10.1063/1.3521481.

[130] J. Sjöström, J. Swenson, R. Bergman, S. Kittaka, Investigating hydration dependence of dynamics of confined water: Monolayer, hydration water and Maxwell–Wagner processes, J. Chem. Phys. 128 (2008) 154503. https://doi.org/10.1063/1.2902283.

[131] S. Kawada, Dielectric anisotropy in ice Ih, J. Phys. Soc. Jpn. 44 (1978) 1881–1886.

[132] J.H. Melillo, J. Swenson, S. Cerveny, Influence of ice formation on the dynamic and thermodynamic properties of aqueous solutions, J. Mol. Liq. 356 (2022) 119039. https://doi.org/10.1016/j.molliq.2022.119039.

[133] M.A. Vasilyeva, Y.A. Gusev, V.G. Shtyrlin, A. Greenbaum (Gutina), A. Puzenko, P.B. Ishai, Y. Feldman, Dielectric Relaxation of Water in Clay Minerals, Clays Clay Miner. 62 (2014) 62–73. https://doi.org/10.1346/CCMN.2014.0620106.

[134] I. Garcia-Lodeiro, G. Goracci, J.S. Dolado, M.T. Blanco-Varela, Mineralogical and microstructural alterations in a portland cement paste after an accelerated decalcification process, Cem. Concr. Res. 140 (2021) 106312. https://doi.org/10.1016/j.cemconres.2020.106312.

[135] J. Swenson, J. Teixeira, The glass transition and relaxation behavior of bulk water and a possible relation to confined water, J. Chem. Phys. 132 (2010) 014508. https://doi.org/10.1063/1.3285286.

[136] G.P. Johari, S.J. Jones, Dielectric properties of polycrystalline D2O ice Ih (hexagonal), Proc. R. Soc. Lond. Math. Phys. Sci. 349 (1976) 467–495.

[137] C. Zhou, X. Zhang, Z. Wang, A discussion of the paper "Dynamic microstructural evolution of hardened cement paste during first drying monitored by 1H NMR relaxometry" by I. Maruyama, T. Ohkubo, T. Haji et al., Cem. Concr. Res. 128 (2020) 105928. https://doi.org/10.1016/j.cemconres.2019.105928.

[138] I. Maruyama, T. Ohkubo, T. Haji, R. Kurihara, Reply to Zhou et al.'s "A discussion of the paper 'Dynamic microstructural evaluation of hardened cement paste during first drying monitored by 1H NMR relaxometry,'" Cem. Concr. Res. 137 (2020) 106219. https://doi.org/10.1016/j.cemconres.2020.106219.

[139] I. Maruyama, T. Ohkubo, T. Haji, R. Kurihara, Dynamic microstructural evolution of hardened cement paste during first drying monitored by 1H NMR relaxometry, Cem. Concr. Res. 122 (2019) 107–117. https://doi.org/10.1016/j.cemconres.2019.04.017.

[140] K. Li, C. Li, Modeling Hydroionic Transport in Cement-Based Porous Materials Under Drying-Wetting Actions, J. Appl. Mech. 80 (2013) 020904. https://doi.org/10.1115/1.4007907.

[141] K. Stanish, M. Thomas, The use of bulk diffusion tests to establish time-dependent concrete chloride diffusion coefficients, Cem. Concr. Res. 33 (2003) 55–62. https://doi.org/10.1016/S0008-8846(02)00925-0.

[142] M.D.A. Thomas, P.B. Bamforth, Modelling chloride diffusion in concrete Effect of fly ash and slag, Cem. Concr. Res. (1999) 9.

[143] Q. Zeng, K. Li, T. Fen-chong, P. Dangla, Pore structure characterization of cement pastes blended with high-volume fly-ash, Cem. Concr. Res. 42 (2012) 194–204. https://doi.org/10.1016/j.cemconres.2011.09.012.

[144] O. Linderoth, P. Johansson, L. Wadsö, Development of pore structure, moisture sorption and transport properties in fly ash blended cement-based materials, Constr. Build. Mater. 261 (2020) 120007. https://doi.org/10.1016/j.conbuildmat.2020.120007.

[145] S.E. Chidiac, M. Shafikhani, Electrical resistivity model for quantifying concrete chloride diffusion coefficient, Cem. Concr. Compos. 113 (2020) 103707. https://doi.org/10.1016/j.cemconcomp.2020.103707.

[146] D. Jansen, F. Goetz-Neunhoeffer, C. Stabler, J. Neubauer, A remastered external standard method applied to the quantification of early OPC hydration, Cem. Concr. Res. 41 (2011) 602–608. https://doi.org/10.1016/j.cemconres.2011.03.004.

[147] M.S. Mohamed, J. Carette, B. Delsaute, S. Staquet, Applicability of Ultrasonic Measurement on the Monitoring of the Setting of Cement Pastes: Effect of Water Content and Mineral Additions, Adv. Civ. Eng. Mater. 6 (2017) 20160062. https://doi.org/10.1520/ACEM20160062.

[148] Y. Dhandapani, M. Santhanam, G. Kaladharan, S. Ramanathan, Towards ternary binders involving limestone additions — A review, Cem. Concr. Res. 143 (2021) 106396. https://doi.org/10.1016/j.cemconres.2021.106396.

[149] S.S. Vialov, Rheological fundamentals of soil mechanics, Elsevier ; Distributors for the United States and Canada, Elsevier Science Pub. Co, Amsterdam ; New York : New York, N.Y, 1986.

[150] R.J.-M. Pellenq, H. Van Damme, Why does concrete set?: the nature of cohesion forces in hardened cement-based materials, MRS Bull. 29 (2004) 319–323. https://doi.org/10.1557/mrs2004.97.

[151] G.W. Scherer, J. Zhang, J.A. Quintanilla, S. Torquato, Hydration and percolation at the setting point, Cem. Concr. Res. 42 (2012) 665–672. https://doi.org/10.1016/j.cemconres.2012.02.003.

[152] A.M. Brandt, Cement-based composites: materials, mechanical properties and performance, CRC Press, 2005.

[153] C. Lian, Y. Zhuge, S. Beecham, The relationship between porosity and strength for porous concrete, Constr. Build. Mater. 25 (2011) 4294–4298. https://doi.org/10.1016/j.conbuildmat.2011.05.005.

[154] K.K. Schiller, Strength of porous materials, Cem. Concr. Res. 1 (1971) 419–422. https://doi.org/10.1016/0008-8846(71)90035-4.

[155] T. Luping, A study of the quantitative relationship between strength and pore-size distribution of porous materials, Cem. Concr. Res. 16 (1986) 87–96. https://doi.org/10.1016/0008-8846(86)90072-4.

[156] R. Kumar, B. Bhattacharjee, Porosity, pore size distribution and in situ strength of concrete, Cem. Concr. Res. 33 (2003) 155–164. https://doi.org/10.1016/S0008-8846(02)00942-0.

[157] D. Breysse, Nondestructive evaluation of concrete strength: An historical review and a new perspective by combining NDT methods, Constr. Build. Mater. 33 (2012) 139–163. https://doi.org/10.1016/j.conbuildmat.2011.12.103.